Nano Research Energy

ISSN 2791-0091 (print); 2790-8119 (online)
https://doi.org/10.26599/NRE.2026.9120220

Review Article

Recent progress in flexible thermoelectric materials and devices

Linlong Xing[1,2], Shaowei Han[1,2], Yanqi Gu[1], Xingang Pan[3], Zhiwei Fu[3], Weidong Chen[1], Yongxin Qin[1] (✉), and Caofeng Pan[1,2] (✉)

[1] *Institute of Atomic Manufacturing, Beihang University, Beijing 100191, China*
[2] *School of Physics, Beihang University, Beijing 100191, China*
[3] *Xuzhou B & C Chemical Co. Ltd, Xuzhou 221300, China*

Received: 29 November 2025 / **Revised:** 17 January 2026 / **Accepted:** 24 January 2026 / **Published date:** 11 March 2026

ABSTRACT

Thermoelectric technology enables all-solid-state direct and clean conversion between thermal energy and electrical energy, and is regarded as an effective strategy to address the issue of energy shortage. Especially in recent years, with the popularity of wearable devices, flexible thermoelectric devices, as an excellent self-powered technology, have experienced rapid development. Therefore, this review systematically summarizes recent advancements in this field. It begins with the fundamental thermoelectric principles and key performance evaluation parameters for flexible devices. Then we emphasize the design strategies to improve devices performance. It is followed by a critical discussion on several material systems. Later, we demonstrate different strategies for fabricating flexible devices based on thin films, fibers and fabrics. Furthermore, practical applications in energy harvesting, cooling, and sensing are also summarized. Finally, the review concludes the challenges and perspectives on future innovations in flexible thermoelectric devices.

KEYWORDS

flexible, thermoelectric materials, device design, film, fiber and textiles

1 Introduction

The rapid development of human society has intensified the demand for energy, while the depletion of traditional fossil fuels has simultaneously led to severe environmental pollution [1, 2]. Consequently, there is an urgent need for green, efficient, and recyclable clean energy sources. In this context, thermoelectric (TE) conversion technology is recognized as a promising green energy solution due to its capability to directly convert thermal energy into electrical energy [3–5]. Beyond generating electricity from ubiquitous waste heat, this technology exhibits significant potential in thermal management with its precise temperature control capabilities. Notably, flexible TE materials and devices can be attached to various curved surfaces or integrated into wearable devices, thereby expanding their application scope. With advantages such as high reliability, the absence of moving parts, and noiseless operation, TE technology, especially in its flexible form, is facilitating the diversification of the energy structure and promoting efficient utilization [6–9].

The TE effect is a physical phenomenon in which electrons or holes in conductive or semiconductor materials migrate from regions of higher temperature to the lower along a temperature gradient when heated. This movement results in an electric current generation or charge accumulation. As shown in Fig. 1(a), TE effect primarily encompasses three fundamental forms: the Seebeck effect, the Peltier effect and the Thomson effect [10, 11]. Discovered by the German physicist Thomas Johann Seebeck in 1821, the Seebeck effect reveals that when two dissimilar materials are connected in a circuit and a temperature difference is maintained at their junctions, an electromotive force and consequently an electric current are generated within the circuit. This phenomenon fundamentally arises from the diffusion and accumulation of charge carriers under a temperature gradient. It is quantified by the Seebeck coefficient (S) and serves as the theoretical basis for TE power generation technology. As its inverse, the Peltier effect was discovered by the French physicist Jean Charles Athanase Peltier in 1834. When an electric current passes through a circuit formed by two different materials, reversible heat absorption or release occurs at the junction. This results from charge carriers absorbing or releasing energy as they cross the material interface to accommodate energy level differences. This effect forms the core operating principle of semiconductor-based refrigerators. Predicted and subsequently observed by the British physicist William Thomson (Lord Kelvin) in 1854, the Thomson effect describes the reversible, heat absorption or release that occurs when an electric current passes through a single conductor possessing a temperature gradient. Although relatively weak, this effect holds significance in precise TE systems. These three effects provide theoretical basis for TE power generation, solid-state refrigeration and precise temperature control.

Since the 1960s, TE power supplies based on radioactive

Address correspondence to Yongxin Qin, qinyongxin@buaa.edu.cn; Caofeng Pan, pancaofeng@buaa.edu.cn

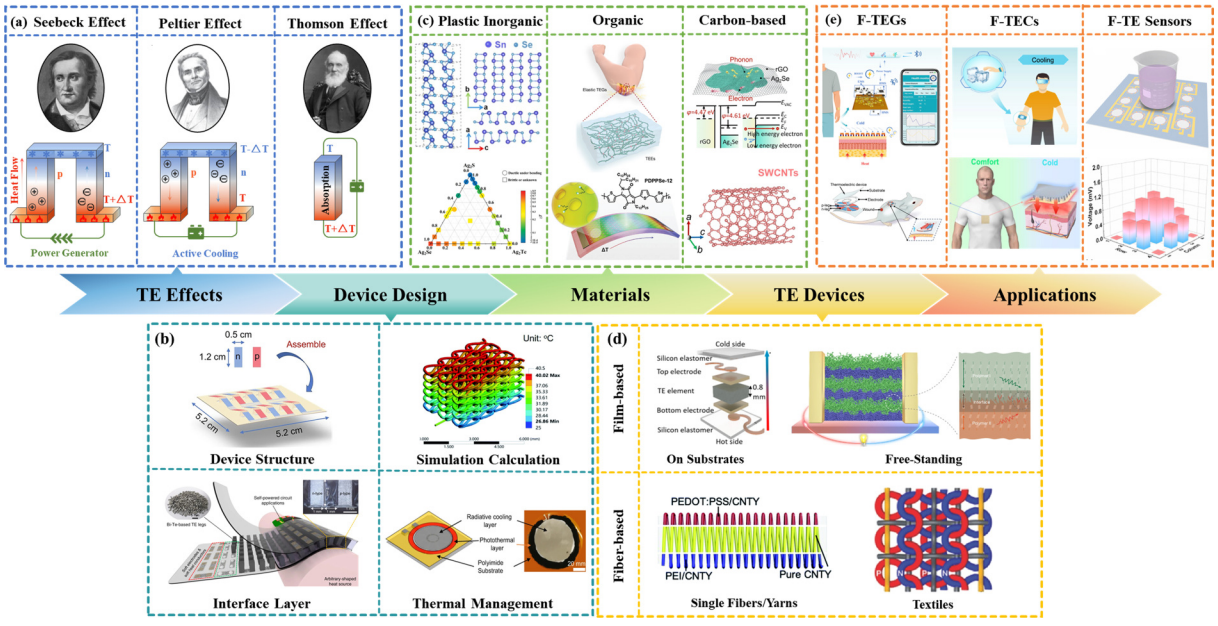

Figure 1 Summary of the review. (a) TE effects and their discoverers. (b) TE device design. Reproduced with permission from Ref. [36], © Chen, W. Y. et al. 2025. Reproduced with permission from Ref. [37], © The Royal Society of Chemistry 2020. Reproduced with permission from Ref. [38], © Lee, B. et al. 2020. Reproduced with permission from Ref. [39], © Liu, Y. et al. 2024. (c) Common TE materials. Reproduced with permission from Ref. [40], © WILEY-VCH, 2022. Reproduced with permission from Ref. [41], © American Chemical Society 2025. Reproduced with permission from Ref. [42], © Liu, K. et al. under exclusive licence to Springer Nature Limited 2025. Reproduced with permission from Ref. [43], © Wiley-VCH GmbH 2024. Reproduced with permission from Ref. [44], © Zhang, L. et al. 2025. Reproduced with permission from Ref. [45], © Elsevier Inc. 2025. (d) Film-based and fiber-based TE Devices. Reproduced with permission from Ref. [46], © American Chemical Society 2020. Reproduced with permission from Ref. [47], © Wang, D. Y. et al. under exclusive licence to Springer Nature Limited 2024. Reproduced with permission from Ref. [37], © The Royal Society of Chemistry, 2020. Reproduced with permission from Ref. [48], © WILEY-VCH Verlag GmbH & Co. KGaA, Weinheim 2016. (e) Applications. Reproduced with permission from Ref. [49], © Liang, L. L. et al. Published by Elsevier Inc. 2025. Reproduced with permission from Ref. [50], © Wiley-VCH GmbH 2024. Reproduced with permission from Ref. [51], © Elsevier Ltd. 2023. Reproduced with permission from Ref. [52], © American Chemical Society 2025. Reproduced with permission from Ref. [53], © Published by Elsevier Ltd. 2024.

isotopes have been successfully utilized in deep space exploration, while Bi_2Te_3 materials have achieved significant commercialization at room temperature (RT) [12, 13]. However, due to the low reserves of Te elements, high costs, and inadequate mechanical strength, researchers continue to seek high-performance TE materials without Te. To date, various inorganic TE material systems, including SnSe [14–16], PbSe [17, 18], Mg_3Bi_2 [19, 20], and half-Heusler alloys [21, 22], have made remarkable advancements, demonstrating extremely high TE figures of merit (*ZT*). Concurrently, theoretical research into the thermal and electrical transport properties of these materials has progressed, with strategies proposed for optimizing electronic transport properties via carrier concentration (n) regulation and band structure engineering [23–25], as well as for reducing thermal conductivity (κ) through nanostructures and defect engineering [21, 26, 27]. Nonetheless, these inorganic materials often contain toxic elements or exhibit insufficient stability at high temperatures [28–30]. Furthermore, their application in flexible devices has been limited due to their inherent rigidity [31, 32]. Therefore, the development of high-performance TE materials with flexible will undoubtedly broaden their application scope. It is necessary to clarify that ionic TE materials also represent promising candidates for fabricating flexible TE devices (F-TEDs) [33]. The fundamental difference between the electronic and ionic TE materials lies in that ionic TE materials operate based on the thermal diffusion effect (Soret effect), where ions selectively migrate under the applied temperature difference to form a concentration gradient, thereby generating a TE voltage. In terms of application, due to higher ion enthalpy, ionic TE materials can generate higher S_i of several millivolts per kelvin [34]. However, due to the limitations of ion saturation concentration and diffusion rate, they often face challenges such as slow response, low energy density, and unstable output [35]. This review mainly focuses on electronic F-TE materials.

Several previous works have reviewed topics related to F-TE materials and devices, particularly focusing on ductile inorganic TEs [54, 55], polymer-based TEs [56, 57], hybrid organic-inorganic TEs [58–60] and carbon-based TEs [4, 61]. In contrast to these prior systematic reviews, this review aims to provide a comprehensive perspective, enabling a more detailed and thorough understanding of the latest advancements in F-TE materials and devices. The second section briefly introduces fundamental principles in the field of thermoelectricity. The third section discusses the design of F-TEDs. The fourth section systematically presents common TE materials, including novel plastic inorganic TE materials, organic TE materials and carbon-based TE materials. The fifth and sixth sections summarize classic and recent F-TEDs from two distinct perspectives: film-based and fiber-based. The seventh section presents common applications. Finally, the eighth section outlines the challenges and prospects in realizing high-performance F-TE materials and devices with stable mechanical strength.

2 Fundamental TE principle

Typically, the energy conversion efficiency of a TE material is represented by the dimensionless figure-of-merit *ZT* [62]:

$$ZT = \frac{S^2\sigma}{\kappa} \cdot T \quad (1)$$

where S is the Seebeck coefficient, representing the voltage

generated per unit temperature difference across the material, σ represents the electrical conductivity, and κ denotes the total thermal conductivity of the TE material, which is the sum of the electronic contribution (κ_{ele}) and the lattice vibration contribution (κ_{lat}). The numerator, $S^2\sigma$, is referred to as the power factor (*PF*), reflecting the material's electrical performance for power generation or cooling [43]. It should be underlined that *PF* is frequently employed to assess the TE properties due to the inherently low κ of polymer materials and the absence of reliable and standard testing techniques [63]. Obviously, a high *ZT* value relies on a high σ to reduce Joule heating, a high *S* for conversion of thermal energy into electrical energy, and a low κ for maximum temperature gradient. The parameters *S*, σ and κ_{ele}, can be expressed as [64]:

$$S = \frac{8\pi^2 k_B^2}{3e\hbar^2} m^* \left(\frac{\pi}{3n}\right)^{2/3} \tag{2}$$

$$\sigma = ne\mu \tag{3}$$

$$\kappa_{ele} = L\sigma T \tag{4}$$

where k_B is the Boltzmann constant, e is the electron charge, $\hbar$ is the Planck constant, m^* is the carrier effective mass, n is the carrier concentration, μ is the carrier mobility, and L is the Lorenz constant. Evidently, the performance enhancement of TE materials is fundamentally constrained by the complex coupling relationship between *S* and σ. And both parameters are strong opposite dependence on n. Therefore, it is important to develop appropriate strategies for synergistic optimization of *S* and σ [26, 65–67].

In terms of a device, the maximum energy conversion efficiency (η_{max}) of a flexible TE generator (F-TEG) can be defined as [68]:

$$\eta_{max} = \frac{T_H - T_C}{T_H} \cdot \frac{\sqrt{1+ZT_{avg}} - 1}{\sqrt{1+ZT_{avg}} + \frac{T_C}{T_H}} \tag{5}$$

$$ZT_{avg} = \frac{\int_{T_c}^{T_H} ZT dT}{T_H - T_c} \tag{6}$$

where T_H and T_C are the hot-side and cold-side temperatures, respectively, ZT_{avg} represents the average *ZT* between T_H and T_C. The above equation highlights that the performance of a F-TEG depends not only on the material itself (ZT_{avg}) but also on the temperature difference (ΔT).

In addition, the open-circuit voltage (V_{OC}) and power output (P_{out}) for F-TEGs are defined as follows [69]:

$$V_{OC} = N \cdot (S_p - S_n) \cdot (T_H - T_C) \tag{7}$$

$$P_{out} = \frac{V_{OC}^2}{(R_{in} + R_{Load})^2} \cdot R_{Load} \tag{8}$$

where N is the number of p/n couples, S_p and S_n are the Seebeck coefficients of p-type and n-type materials, respectively. R_{in} is the internal resistance of the device, and R_{Load} is the load resistance in the circuit. Especially, when R_{in}=R_{Load}, P_{out} reaches its maximum value [70]:

$$P_{max} = \frac{V_{OC}^2}{4R_{Load}} \tag{9}$$

In practical applications, the maximum power density (ω_{max}) holds greater reference value than η_{max}, especially in cases of harvesting low-grade heat to generate sufficient power that can drive electronic components. It can be expressed as [69]:

$$\omega_{max} = \frac{P_{max}}{A_D} = \frac{(T_H - T_C)^2}{4H} \cdot \frac{(S_p - S_n)^2 \cdot F}{\rho} \tag{10}$$

where A_D is the cross-sectional area of the TEG, F is the fill factor (the ratio of the TE legs area to A_D), H denotes the height of the legs, and ρ represents the electrical resistivity of the legs.

The cooling capacity of a TE cooler (TEC) is assessed by the coefficient of performance (COP) [17]:

$$COP = \frac{T_C}{T_H - T_C} \cdot \frac{\sqrt{1+ZT_{avg}} - \frac{T_H}{T_C}}{\sqrt{1+ZT_{avg}} + 1} \tag{11}$$

Compared to traditional refrigeration systems, TECs usually exhibit a lower COP. To obtain comparable cooling performance, a ZT_{avg} greater than 4 is necessary, which remains a challenge for current technologies. Therefore, TECs are commonly used for precise temperature management on a small scale.

3 TE device design

Currently, most research on F-TEDs are the search of appropriate materials and improvement of their TE properties alongside flexibility and stability. And it is most important to translate the inherent material advantages into device high-performance outputs in practical applications through multiscale device engineering. This involves the selection of suitable device architectures, optimization of TE legs' geometry, distribution and fill factor, identification of compatible interfacial materials, and improvement of the thermal management.

3.1 Device structure

The energy conversion efficiency and potential application scenarios of TEDs are significantly influenced by their structural design. Figure 2 illustrates architectural types of TEDs in vertical, horizontal, Y-type, circular and monopole structures [69, 71, 72].

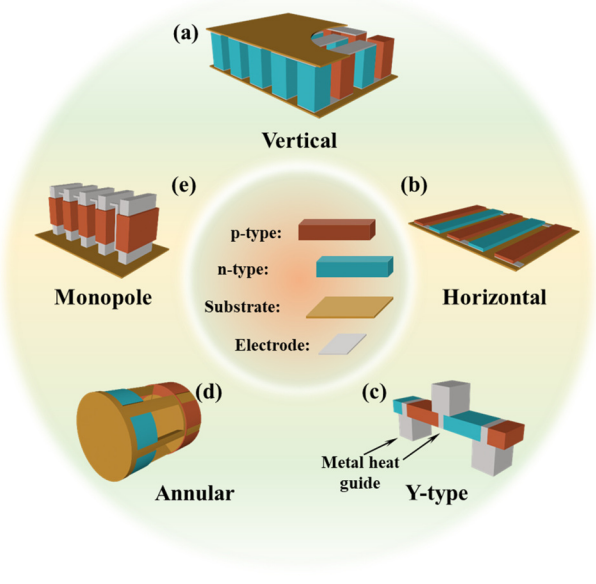

Figure 2 Basic structures of F-TEDs: (a) vertical, (b) horizontal, (c) Y-type, (d) annular and (e) monopole structures.

Each configuration possesses distinct characteristics. Choosing the appropriate device structure is a critical step that depends on the specific application.

The vertical structure represents one of the most classic device architectures (Fig. 2(a)). In this arrangement, TE elements are oriented perpendicular to the substrate. Using its compact spatial structure and efficient heat transfer path from hot to cold side, it reaches extremely high heat flux density and conversion efficiency. This makes it particularly well-suited for small-scale devices with limited spatial extents that also require higher output power [73, 74]. However, the overall device typically possesses a relatively high rigidity. In contrast, the TE elements with a horizontal structure are arranged parallel to the substrate (Fig. 2(b)). This configuration enables the easy integration of devices with planar systems, making it an ideal choice for flexible and wearable electronics [36, 75]. Thus, its advantage lies in the ability to utilize large surface area for heat management. Nevertheless, it is a considerable challenge to establish a large temperature gradient in the plane. A novel Y-type structure has been designed to solve the inconsistency between the planar temperature gradient and out-of-plane heat dissipation (Fig. 2(c)). This architecture employs a branched geometry and is typically combined with metal conductors to accurately guide the heat flow path and promote the establishment of a larger temperature difference [76, 77].

It offers high flexibility and adaptability to complex and irregular surfaces, demonstrating great potential in the field of medical devices that require targeted heat delivery and precise temperature control. In annular structure (Fig. 2(d)), the components are organized in a cylindrical or annular manner [78, 79]. This configuration is particularly well-suited for wrapping around tubular surfaces for waste heat recovery or thermal management. The monopolar structure consists of a vertical stack of TE units, all the same type, either n-type or p-type. Although such a device does not exhibit high performance, it serves as a simple and fundamental research evaluation tool for assessing the potential of any new material under device conditions and for studying the interfacial characteristics between electrodes and the TE materials [80, 81]. However, due to its high thermal resistance and low efficiency, this structure is not suitable for practical cooling applications. In summary, the choice of device structure requires a balance among efficiency, power, flexibility, thermal management, and integration methods [71, 82]. Based on actual needs, the selection of suitable device structure will facilitate full utilization of material properties.

3.2 Simulation calculation

The continuous refinement of various physical theories has established calculational simulation as an indispensable tool in the research of TE materials. First-principles calculations based on density functional theory (DFT) can reveal the electronic band structure and phonon spectra of materials at the microscopic level, enabling accurate predictions of intrinsic electrical properties such as S and m^* [83–85]. Furthermore, the combination of DFT and Boltzmann transport theory allows to simulate the variation of transport coefficients with doping concentration, which can provide clear experimental optimization guidelines [86, 87]. Simultaneously, phonon spectrum calculations and molecular dynamics (MD) expand the understanding of decreasing lattice thermal conductivity mechanism [88–90]. These methods analyze phenomena such as point defect scattering and phonon scattering by nano-precipitates and grain boundaries, thereby guiding the design of "phonon glass-electron crystal" materials [91, 92]. In the realm of materials development, the integration of high-throughput computing and machine learning has significantly accelerated the screening and prediction of novel high-performance TE materials by rapidly screening material databases and establishing structure-property mapping relationships [93–95]. Moreover, simulations have been extended to investigate the atomic-level mechanisms of doping behavior, for instance, calculations of doping formation energy and defect energy levels help elucidate the influence of dopants on electrical and thermal transport properties [96, 97].

At the macroscopic device level, multi-physics coupling simulations based on the finite element analysis (FEA) method can model the temperature field distribution, thermal stress, and output power of TEDs, thereby optimizing thermal management design and device architecture [98–100]. For instance, Fan et al. utilized FEA method to investigate the influence of leg geometry, fill factor, and leg height on the TE performance and mechanical reliability of wearable TEGs (Fig. 3(a)) [98]. Among these factors, cuboid-shaped legs exhibited the lowest stress levels while maintaining an output power only marginally lower (by 1.22%) than that of triangular prism-shaped legs, indicating superior mechanical reliability. Increasing the fill factor enhances output power but also increases the minimum safe bending radius, thereby reducing flexibility. However, increasing the number of thermocouples to 64 pairs simultaneously boosted the output power and reduced the maximum stress within the legs, achieving synergistic optimization of performance and reliability. This research provides crucial guidance for the structural design of wearable TEGs, emphasizing that optimizing geometric parameters, specifically adopting cuboid-shaped legs and increasing the number of thermocouples, can ensure high TE output while significantly enhancing mechanical robustness. Liu et al. employed FEA method to solve their model under different temperature gradients and load conditions, incorporating all essential components and realistic natural convection boundary conditions for a wearable TEG [99]. The simulation results showed excellent agreement with experimental data. By analyzing the resulting temperature and voltage distributions within the TED, they elucidated the impacts of side heat loss and internal heat conduction of the encapsulation. Furthermore, they explored the influence of the κ of the encapsulation and the geometric dimensions of the TE legs on the output performance. As exhibited in Fig. 3(b), Zheng et al. systematically studied the temperature differences and output voltages of three different textile structures using FEA method, providing valuable references for subsequent experiments [37]. The effects of these three distinct textile architectures, specifically weft-knitted, warp-knitted spacer and woven fabrics, on the TE performance of F-TE textiles were systematically investigated. The results demonstrated that the knitted fabric structure could establish the largest temperature difference. In contrast, the woven fabric, due to its regular yarn arrangement in the thickness direction, formed fewer static air pockets capable of suppressing heat convection. By weaving spacer fabrics, a ω_{max} of 51.5 mW·m^{-2} was achieved under a temperature difference of 47.5 K. In summary, simulation technology provides insights into the intrinsic physical mechanism of TE materials, while also reducing experimental trial-and-error costs.

3.3 Interface layer

Interface issue is another critical factor that affects the performance and reliability of F-TEDs. These problems may arise from interdiffusion between TE materials and electrode materials

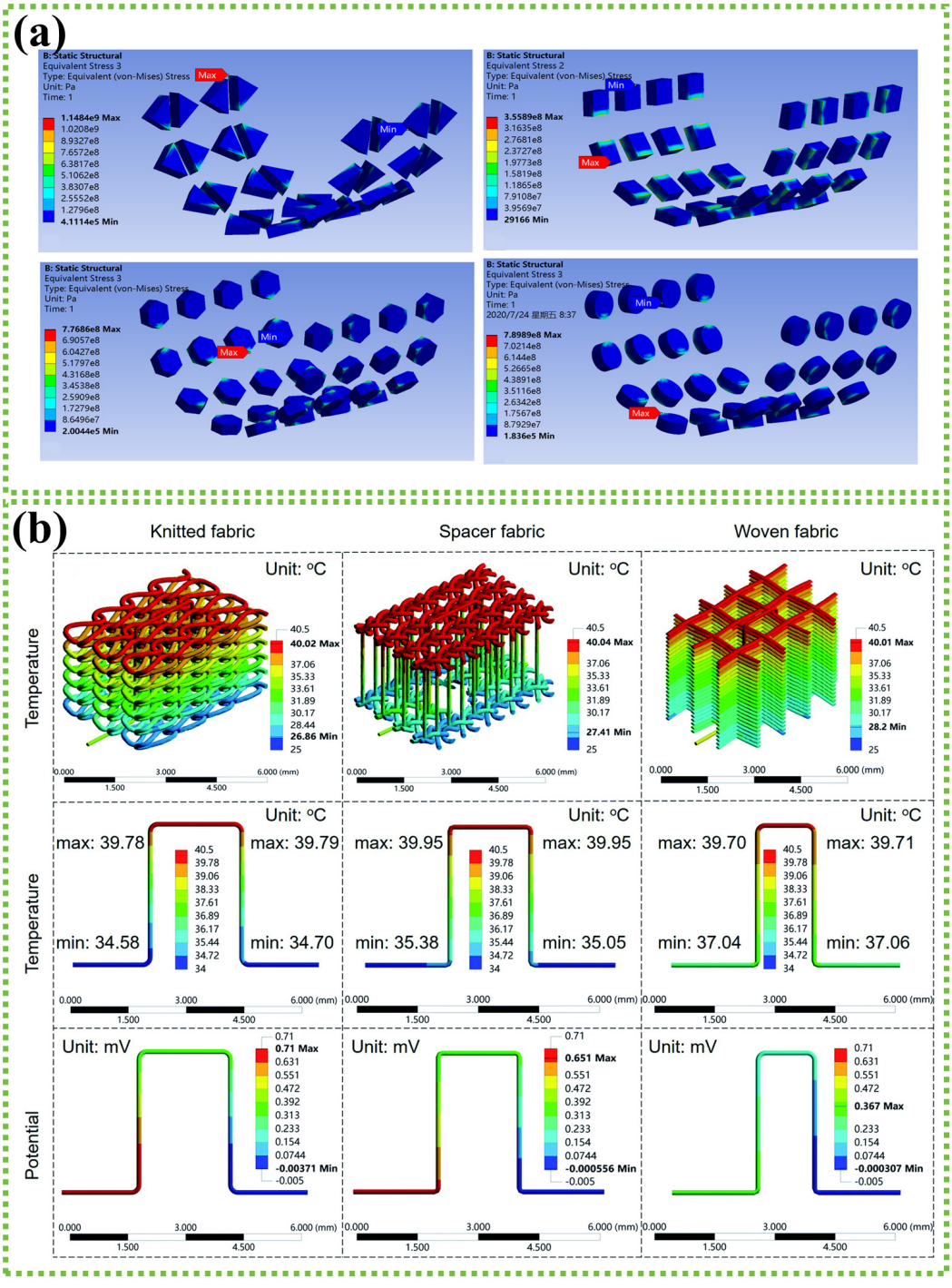

Figure 3 Computer simulation calculation for flexible TEDs. (a) Von Mises stress profiles in four different geometrical shape TE legs. Reproduced with permission from Ref. [98], © Elsevier Ltd. 2021. (b) Finite element simulations of three typical fabric structure including weft-knitted, warp-knitted spacer and woven fabrics. Reproduced with permission from Ref. [37], © The Royal Society of Chemistry 2020.

during long-term operation under thermal cycling, high contact resistance at the interface. And the reliable adhesion is necessary for flexible applications, particularly avoiding cracking induced by stress concentration [101–104]. These challenges degrade the device's overall performance and mechanical stability.

Many innovative strategies have been proposed to solve these problems. For example, Zuo et al. offered an atomic-level interface reinforcement strategy to successfully achieve efficient and stable all-Mg-based TEDs through precisely controlling interfacial chemical bonding and diffusion behaviors (Fig. 4(a)) [95]. A high-throughput screening method was developed to greatly improved efficiency in the identification of suitable barrier layers. This method utilized a multi-interface synchronous construction technology. The formation of multi-heterogeneous interfaces and parallel resistance testing were possible in one sintering process, which significantly boosted experimental efficiency. Co metal was found to be an exceptional candidate for barrier layer material, showing ultra-low and stable contact resistance of less than 2.5 μΩ·cm^2, high bonding strength of 60.6 MPa, and negligible elemental interdiffusion after prolonged service. The advantages of

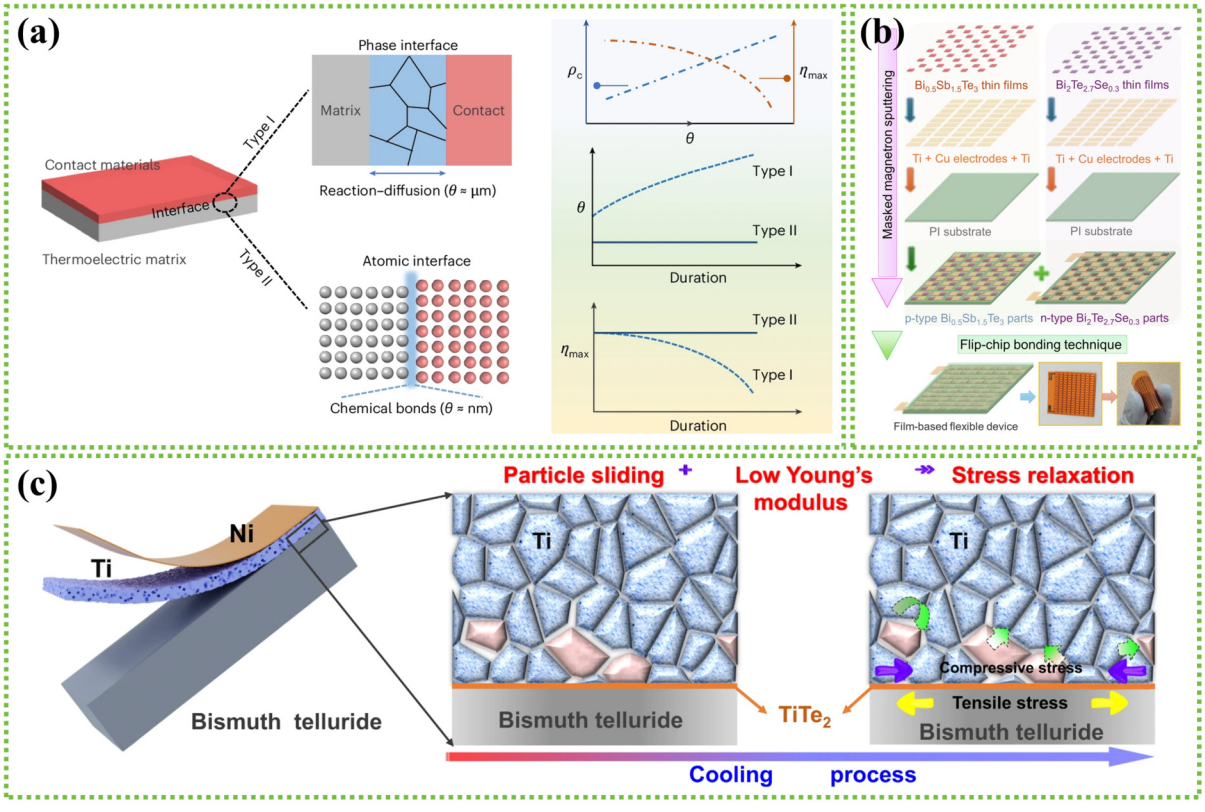

Figure 4 Various strategy for optimizing the interface layers of F-TEDs. (a) Atomic bonding interface. Reproduced with permission from Ref. [95], © Zuo, W. S. et al. under exclusive licence to Springer Nature Limited 2025. (b) Multi-layer interface design. Reproduced with permission from Ref. [105], © Tan, M. et al. 2025. (c) Release interfacial stress via a lowered Young's modulus and particle sliding. Reproduced with permission from Ref. [106], © Sun, Y. X. et al. 2023.

this atomic-level interface were further confirmed with molecular dynamics simulations. Experimental results demonstrated that devices using this atomic interface design retained stable conversion efficiency even after 600 full thermal cycles in a high temperature range of 373 to 573 K, much better than devices with conventional interfaces. In addition, Fig. 4(b) described an innovative interface by adding an approximately 10 nm thick Ti contact layer between the Cu electrode and the polyimide (PI) substrate. And a barrier layer with the same thickness was introduced between the Cu electrode and the TE thin film [105]. The devices' flexibility as well as output performance was enhanced significantly because of improved interfacial adhesion and lower contact resistance. A device comprising 162 pairs of p/n thin-films showed a small resistance change rate of only about 3% after more than 100 bending cycles at 10 mm radius. It displayed a high normalized power density (ω_n) of greater than 4 μW·cm^{-2}·K^{-2} at a small temperature difference of 5 K. Furthermore, when attached on an irregular heat source at 50 °C, three devices in series generated a V_{OC} of 1.85 V, successfully powering a light-emitting diode (LED) without extra heat sink or booster circuit. Similarly, as shown in Fig. 4(c), Sun et al. put forward a loose Ti barrier layer that took advantage of its low Young's modulus and particle sliding mechanism to relieve interface stress [106]. A $TiTe_2$ nano-reaction layer formed in situ at the Bi_2Te_3 interface to achieve metallurgical bonding and ohmic contact. This design enabled the device to operate for 360 hours at a hot-side temperature of 523 K without appreciable performance degradation. These works indicate that atomic-level interface bonding design has been a resultful method to overcome the challenge of interface failure [107].

3.4 Thermal management

The thermal management of TEDs is a systems engineering issue that is crucial for ensuring their conversion efficiency and reliability. Essentially, it aims to establish and keep the maximum effective temperature difference (ΔT) between hot and cold sides, since the output power and conversion efficiency of TEDs are proportional to the square of ΔT [108–111]. Thermal resistance at either side directly reduces the utilizable temperature gradient and so significantly impairs performance. Therefore, for TEGs, the hot side must closely contact the heat source for efficient heat absorption. On the other hand, the cold side requires high-performance heat dissipation components to rapidly release waste heat into surrounding environment. For TECs, it is important that the waste heat generated at the hot side must be dissipated quickly to avoid negatively impacting their cooling effect or even the failure of such devices. In addition, effective thermal management minimizes localized thermal stress and protects the long-term device reliability. It inhibits mechanical failures, including interfacial cracking and solder joint detachment caused by mismatch in coefficients of thermal expansion among different materials. It also suppresses performance degradation arisen from adverse interfacial diffusion and chemical reaction at high temperature [112–114]. As seen in Fig. 5(a), Lee et al. designed a soft thermal conductor by magnetically self-assembling Ag-coated Ni particles within an elastomeric substrate, significantly enhancing heat transfer to the TE legs [38]. Utilizing a highly automated manufacturing process, they assembled a F-TED comprising 220 p-n thermocouples pairs. The elastomeric substrate allows the device to conform perfectly on curved surfaces without any air gaps, which helps to reduce interfacial heat loss.

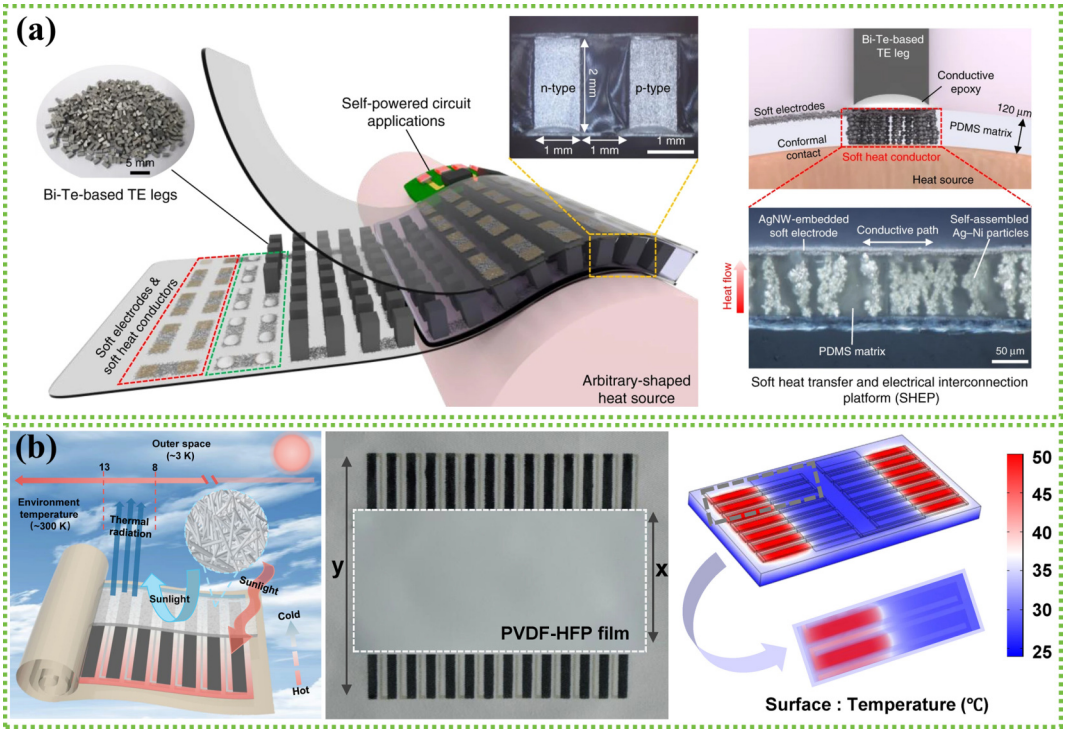

Figure 5 Methods for optimizing heat transfer and enhancing heat dissipation. (a) Soft electrodes and soft heat conductors for self-powered circuit. Reproduced with permission from Ref. [38], © Lee, B. et al. 2020. (b) Passive radiation cooling technology for assisting heat dissipation. Reproduced with permission from Ref. [115], © Liu, J. Z. et al. 2025.

Thereby, a bigger temperature difference was set up. The TED produced a P_{out} of 7.02 mW and a V_{OC} of 2.12 V, under $\Delta T = 40$ K.

To achieve efficient heat dissipation, various heat dissipation structures or components have been extensively developed and applied. The fin-type heat sink is a classic and widely used structure that achieves effective heat dissipation by increasing the surface area, thereby enlarging and maintaining the temperature difference across the device [116, 117]. For example, Khan et al. achieved a ω of 11.46 μW·cm^{-2} and a V_{OC} of 24 mV during nighttime by attaching a fin-shaped heat sink to the cold side [118]. Generally, these fin-like heat sinks are fabricated from metallic materials with high κ. However, their drawbacks including high rigidity, substantial weight, and space consumption limit their application in flexible devices [119, 120]. To overcome these limitations, lighter-weight alternatives such as Cu foams and Cu fabrics which offer certain flexibility and high κ, have been integrated into TEGs as heat dissipation components [114, 121, 122]. In recent years, radiative cooling materials have garnered significant attention [123–125]. These materials can radiate heat directly into the cold universe (approximately 3 K) to achieve sub-ambient cooling through the atmospheric window (8–13 μm band) without additional energy consumption [119, 126, 127]. As demonstrated in Fig. 5(b), Liu et al. integrated an electrospun poly(vinylidene fluoride-hexafluoropropylene) (PVDF-HFP) radiative cooling film onto a screen-printed carbon nanotube-based TE textile [115]. The 0.2 m^2 TE textile produced a temperature gradient of 37 K under a solar irradiance of ~800 W·m^{-2} and a ω_{max} of 0.20 mW·m^{-2}. Besides applying radiative cooling technology to lower the cold-side temperature, other functional materials can be incorporated to optimize the thermal management of TEDs for higher performance. For instance, photothermal conversion materials can be deposited on the hot side to convert ambient light energy into heat, which helps in raising the hot-side temperature to increase ΔT [128–130]. Phase change materials (PCMs) can also be incorporated to mitigate intermittent heat sources and stabilize the hot-side temperature [112, 131]. These materials act as thermal buffers by absorbing or releasing latent heat during phase transition processes.

4 Materials

4.1 Plastic inorganic materials

Traditional inorganic TE materials, such as Bi_2Te_3, tend to be inherently brittle at RT. The reason for their brittleness is their atomic bonding, which primarily consists of strong highly directional ionic or covalent bonds [132, 133]. These bonds create a rigid crystal lattice. That means these materials cannot dissipate energy through plastic deformation mechanisms such as dislocation glide or grain boundary sliding when subjected to external stress. Consequently, stress tends to concentrate at defects, which leads to directly cleavage fracture. This characteristic severely limits their application in flexible devices [54, 134]. However, recent studies have discovered metal-like plasticity in materials such as Ag_2S [133, 135], InSe [136, 137], SnSe [16, 138] and $SnSe_2$ [139, 140] at RT. This unusual characteristic is often attributed to their unique layered structures, weak van der Waals (vdW) interactions between layers, or specific atomic bonding configurations [54, 90]. These findings provide a promising new direction for overcoming the intrinsic rigidity of inorganic TE materials.

4.1.1 *Silver chalcogenide*

In the past, the research on inorganic TE materials mainly focused on rigid systems. A significant breakthrough occurred in 2018, when Shi et al. discovered that α-Ag_2S ingots could sustain compressive strains of up to 50% without fracture [133]. It was

also a surprise that this material could also withstand bending strain of 20% without cracking, which was extremely rare in previous studies. This finding had opened up new avenues for the development of F-TE materials. However, the TE performance of Ag_2S at room temperature is not satisfactory due to its very low n (10^{14}–10^{15} cm^{-3}) [141]. Further investigations are needed to ascertain the viability of these newly discovered plastic inorganic semiconductor materials as TE candidates. Based on the optimization strategies such as doping and alloying employed in previous studies for TE materials, researchers have synthesized a variety of silver chalcogenides Ag_2Q (Q = S, Te, Se) [40, 142–144]. For instance, Liu et al. demonstrated that I doping in Ag_2S not only optimized n but also suppressed κ_{lat}. Consequently, the ZT value increased threefold compared to pristine Ag_2S [145]. Similarly, Chang et al. achieved an optimal n in the $Ag_{5.98}SSe_{0.6}Te_{1.4}$ material by reducing the electronegativity of the anion sublattice and introducing Ag vacancies at the cation sites, which led to a high PF of 6.0 $\mu W \cdot cm^{-1} \cdot K^{-2}$ and a low κ of 0.27 $W \cdot m^{-1} \cdot K^{-1}$ at RT. Under a bending radius of 7 mm, the electrical resistance value remained basically unchanged over 500 cycles [146].

Unlike Ag_2S, the materials Ag_2Se and Ag_2Te possess better TE properties, but lack mechanical flexibility [147–149]. In order to effectively use the respective advantages of Ag_2S and Ag_2Se, Wu et al. ingeniously designed a novel sandwich-structured $Ag_2(S, Se)$-Ag_2Se TE film [25]. The $Ag_2(S, Se)$ core layer contributed to plasticity while maintaining low κ in this architecture. Thanks to the epitaxial growth method, the Ag_2Se layers were highly oriented and exhibited strong bonding between layers, which ensured efficient carrier transport and structural integrity during bending. As a result, a high ZT value of 0.91 was achieved for this unique structure within the near-room temperature region. During the bending cycle test, the Ag_2Se shell layer did not show obvious cracks until 400 cycles, which was associated with the increased resistance observed during the test. Although adjusting the alloy elements content can enhance TE performance, it might also deteriorate the material's intrinsic plasticity [150]. Therefore, there is an optimal compositional range to obtain excellent TE properties and plasticity. For $Ag_2S_{1-x}Se_x$, this range is about x = 0.4 to 0.6. And that is about x = 0.3 to 0.9 in $Ag_2S_{1-x}Te_x$ [55]. To balance TE properties and plasticity, it is necessary to clarify the relationships among composition, structure and properties. For the $Ag_2S_{1-x}Se_x$ system, the material began to transforms from monoclinic to orthorhombic crystal structure when x > 0.7. And the mechanical property tests suggested that the monoclinic $Ag_2S_{1-x}Se_x$ retained ductile and flexible, while the orthorhombic samples were brittle [151, 152]. In contrast, the crystal structure of the $Ag_2S_{1-x}Te_x$ system is more complex. A small amount of Te (x = ~ 0.16) can induce a phase transition from monoclinic to cubic, which significantly enhances TE performance while maintaining plasticity [144]. With further Te introduction, an amorphous phase appears. The results showed that the precipitation of the monoclinic phase Ag_2Te will seriously deteriorate the plasticity, while the cubic-crystalline/amorphous composite material exhibited plasticity. Through appropriate heat treatment processes, the phase structure can be regulated, thereby optimizing the comprehensive performance of the material [153, 154].

The common TE devices operate through alternately connected n-type and p-type legs. Furthermore, if these legs consist of materials with similar physical properties, the internal stress caused by differing coefficients of thermal expansion can be minimized, which is crucial for high-efficiency devices [155–157]. Due to the low defect formation energy of Ag interstitials in Ag_2Q compounds, nearly all Ag_2(S, Se, Te) pseudobinary solid solutions exhibit n-type semiconducting behavior [158]. Consequently, developing p-type TE materials based on silver chalcogenides has attracted significant research attention [64, 159]. Hrickova et al. attempted to achieve a p-type transition in α-Ag_2S by doping with Ge [135]. Although Ge doping resulted in a marked increase of σ and a shift of S towards positive values, the overall attempt was ultimately unsuccessful. Further studies indicated that Ge did not integrate into the Ag_2S lattice but instead precipitated as another phase within the matrix, indicating the low solubility of this foreign dopant. The selection of suitable dopants that possess high solubility and shallow defect levels is still a challenging task. In a breakthrough, Gao et al. successfully achieved an n- to p-type transition by alloying with Cu at the Ag sites and precisely controlling the Cu/Ag ratio to manipulate lattice defects, specifically Ag interstitials and Cu vacancies [159]. $(Ag_{1-x}Cu_x)_2S_{0.7}Se_{0.3}$ samples exhibited p-type conduction characteristics within the composition range of x = 0.7 to 0.8 while retaining good plasticity. As a result, $(Ag_{0.2}Cu_{0.8})_2S_{0.7}Se_{0.3}$ achieved a ZT of 0.42 at 800 K. Furthermore, by introducing a slight Cu deficiency to increase the hole concentration, the ZT value of $(Ag_{0.2}Cu_{0.785})_2S_{0.7}Se_{0.3}$ was enhanced to 0.95 at 800 K. However, their TE performance within the room temperature range remained still poor. Therefore, Yang et al. developed a series of high-performance p-type plastic TE materials based on the composition-property phase diagram of AgCu(Se, S, Te) pseudoternary solid solutions. These materials achieved notable ZT values of 0.45 at 300 K and 0.68 at 340 K [31]. Furthermore, Shen et al. employed a similar approach to increase the ZT value of the p-type $Ag_{0.995}CuSe_{0.22}S_{0.08}Te_{0.7}$ material to 0.81 at 340 K. And an in-plane TED assembled based on this material showed an extremely good mechanical stability after 500 bending tests under a bending radius of 10 mm, with the resistance change being only about 1% [160].

4.1.2 *Tin chalcogenides*

The exceptional ductility of Ag_2S, stemming from metallic Ag-Ag bonds that enable the sliding of Ag-S octahedral units without disrupting the Ag-S framework, has inspired researchers to shift their focus to 2D vdW semiconductor materials [54, 55]. In typical 2D vdW bulk inorganic semiconductors, intralayer bonding is usually covalent or ionic-covalent, resulting in in-plane rigidity [161, 162]. The presence of vdW gaps makes these materials prone to cleavage, thereby hindering their ability to retain structural integrity through plastic deformation [163]. In 2020, Wei et al. discovered that bulk single-crystal InSe can be compressed by several orders of magnitude at RT and deformed into Möbius strips or simple origami shapes [164]. This unusual plasticity in a 2D vdW inorganic semiconductor was attributed to interlayer sliding and dislocation glide, which was governed by long-range In-Se Coulomb interactions across the vdW gap and soft in-plane In-Se bonds. More significantly, they proposed a deformation factor as a criterion for pre-screening bendable and deformable candidate inorganic semiconductors. Building on this, Gao et al. further developed a nearly automated and efficient high-throughput screening method, identifying dozens of potentially deformable 2D chalcogenides, such as MoS_2, GaSe, and $SnSe_2$ [94]. Among these materials, $SnSe_2$ achieves the optimal compromise between plasticity and TE performance. Compared to InSe, which exhibits excellent plasticity but suffers from extremely low intrinsic n that hinders the optimization of its TE properties, $SnSe_2$ stands

out with higher room-temperature *ZT* values among similar plastic materials through strategies such as doping and phase structure engineering. Meanwhile, unlike other plastic materials like Ag_2S, which often require extensive alloying to enhance TE performance, typically at the expense of plasticity, $SnSe_2$ demonstrates superior and effectively tunable electrical transport properties via doping, while maintains significant macroscopic plasticity and inherent slip characteristics of its layered structure.

Deng et al. reported in 2022 that bulk single-crystal $SnSe_2$ exhibited significant plasticity at room temperature [139]. Furthermore, upon doping with a small amount of halogen elements, $SnSe_{1.95}Br_{0.05}$ demonstrated a high *PF* of 10.8 $\mu W \cdot cm^{-1} \cdot K^{-2}$ and a *ZT* of 0.09 along the in-plane direction at 375 K. Like other discovered plastic inorganic TE materials, $SnSe_2$ has a band gap of ~1.16 eV. Although this relatively large band gap contributes to a higher *S*, it also results in a low *n* (1.6×10^{18} cm^{-3}), leading to a low ZT value. Based on halogen doping, they employed a dual-doping strategy, introducing Cl/Br at Se sites while intercalating Cu into the vdW gaps, to change the stacking sequence of $SnSe_2$ [165]. Successfully inducing a phase transition from the 18R to the 4H. In 4H-$Cu_{0.005}SnSe_{1.95}Br_{0.05}$, the *n* increased to 4.2×10^{19} cm^{-3}. Therefore, the *PF* and *ZT* value were 18.0 $\mu W \cdot cm^{-1} \cdot K^{-2}$ and 0.14, respectively at 375 K. A planar flexible TED fabricated from this material achieved a ω of 0.18 $W \cdot m^{-1}$ under ΔT = 30 K. Furthermore, Liu et al. introduced Na atoms into the vdW gaps [166]. The Na intercalation acted as an n-type dopant, providing additional electrons and increasing the *n* to 3.3×10^{18} cm^{-3}. Unlike Cu intercalation, Na intercalation did not alter the crystal structure, but instead reduced the lattice vibration energy and weakened phonon scattering. As a result, the carrier mobility also increased with higher Na content. This led to an σ of 2500 $S \cdot m^{-1}$ in $Na_{0.1}SnSe_2$, which was an order of magnitude higher than that of pristine $SnSe_2$, although its efficiency remained significantly lower than that achieved with Br/Cl doping. $Na_{0.02}SnSe_2$ achieved the highest *PF* of ~5.6 $\mu W \cdot cm^{-1} \cdot K^{-2}$ at 300 K. When $x \leq 0.05$, Na_xSnSe_2 exhibited plasticity comparable to $SnSe_2$, sustaining a bending strain of up to 15%. Nonetheless, when $x \geq 0.07$, the plasticity decreased significantly due to the weakening of interlayer Se-Se bonds. Recent research had shown that the addition of Br could effectively improve *n* and σ, hence significantly improving PF [167]. Additionally, Pb doping induced a strong phonon softening effect, which reduced the phonon group velocity and κ. As a result, the $SnSe_2$-2% $PbBr_2$ sample achieved a peak *ZT* of approximately 0.76 at 773 K and an average *ZT* of about 0.51, which is more than 530% improved than the undoped sample. This work provides a feasible strategy for enhancing the TE performance of $SnSe_2$-based single crystals over a wide temperature range.

In contrast to $SnSe_2$, SnSe, composed of the same elements but distinct highly distorted orthorhombic crystal structure, achieves an extremely low lattice thermal conductivity and high *ZT* due to its strong phonon anharmonicity and pronounced anisotropy [168–170]. However, its distorted layered structure impedes effective interlayer sliding, rendering it challenging to directly apply in flexible devices [171, 172]. Numerous attempts have been made to expand the application of SnSe into the field of flexibility. For example, Nicolas Augustus Rongione et al. reported flexible SnSe films for lower grade waste heat recovery near room temperature by surfactant-free hydrothermal synthesis method [173]. The stacked SnSe nanosheets introduced strong interface phonon scattering, leading to an extremely low κ of 0.09 $W \cdot m^{-1} \cdot K^{-1}$. The maximum fluctuation of *S*, resistance value and κ of the SnSe film deposited on the polyethylene terephthalate (PET) substrate after 1000 bending cycles were respectively 7%, 6% and 5%, showing a superior flexibility and stability. In addition, Natalia V. Morozova et al. significantly enhanced the PF of layered p-type SnSe single crystals up to approximately 180 $\mu W \cdot cm^{-1} \cdot K^{-2}$ at room temperature via manipulating an external stress [174]. This giant enhancement can be attributed to band-gap narrowing leading to optimize the *n*, Lifshitz transition resulting in introducing multi-valley conduction while maintaining a high *S*, and strong crystal transformation bring about inducing severe intralayer plastic deformation while preserving the layered stacking.

4.1.3 Mg_3Bi_2-based

In previous studies, Mg-based TE materials have achieved significant development due to their abundant raw materials, good processability, and excellent TE properties, showing potential for room-temperature applications [175–177]. In 2020, Li et al. discovered that Nd doping in Mg_3Sb_2-based compounds increased the *n* to ~8×10^{19} cm^{-3} because of the substitution of Nd for Mg [178]. As a result, $Mg_{3.2}Nd_{0.03}Sb_{1.5}Bi_{0.5}$ achieved a high *PF* of 20.6 $\mu W \cdot cm^{-1} \cdot K^{-2}$ at 725 K and a maximum *ZT* value of 1.8. Remarkably, alongside its excellent TE performance, the material also exhibited superior processability. The sample could be easily machined into a dog-bone shape with external threads at both ends. Its measured hardness, Young's modulus, and fracture toughness were 1.1 GPa, 49.8 GPa, and 1.4 $MPa \cdot m^{1/2}$, respectively. Building on the discovery of this plasticity and to weaken the strong scattering effect of carriers by Mg-deficient phases at grain boundaries, Zhang et al. employed a cold deformation technique instead of a high-temperature solid solution process [179]. Under high pressure, the grain size increased perpendicular to the pressure direction, significantly reducing grain boundary scattering. Consequently, the $Mg_{3.1}Bi_{1.5}Sb_{0.49}Te_{0.01}$ sample achieved a carrier mobility of ~86.6 $cm^2 \cdot V^{-1} \cdot s^{-1}$ while maintaining *n* unchanged. And the *PF* at room temperature reached 16.2 $\mu W \cdot cm^{-1} \cdot K^{-2}$, comparable to samples prepared by high-temperature sintering. However, its relatively low room-temperature ZT still limited its application potential. To enhance room-temperature TE performance, Li et al. revealed the origin of the intrinsic high plasticity in Mg_3Sb_2 and Mg_3Bi_2 [180]. By optimizing the Bi content in $Mg_3Sb_{2-x}Bi_x$ to regulate both TE properties and plasticity, they achieved a large compressive strain of 43% and a high *ZT* of 0.72 at room temperature in the polycrystalline sample $Mg_3Sb_{0.5}Bi_{1.498}Te_{0.002}$. The abundance of dislocations facilitates the sliding of atomic layers during deformation, while the continuously connected Mg-Sb/Bi bonds within the sliding layers ensure structural integrity, which is a key reason for the material's high plasticity. Furthermore, the high plasticity and toughness of this compound allow it to be easily processed into particles smaller than 100 μm ×100 μm, which can be assembled into both in-plane and out-of-plane flexible TE modules. Otherwise, Hu et al. used magnetron sputtering and *ex-situ* annealing techniques to fabricate high-performance (*PF* = 1.59 $\mu W \cdot cm^{-1} \cdot K^{-2}$, 60 °C) n-type flexible Mg_3Bi_2 TE films, while ensuring high adhesion to various substrates. After 500 bending cycle tests with a radius of 5 mm, the resistance increase was less than 10% [20]. The high internal resistance at the material-electrode interface is identified as a primary factor limiting device performance, highlighting the necessity of optimizing the contact interface to fully utilize the material's high TE potential.

The plasticity of Mg_3Bi_2 is not limited to polycrystalline materials. Zhao et al. discovered that single-crystal Mg_3Bi_2 can

withstand compressive strains exceeding 75% and tensile strains up to 100% along the ab-plane at room temperature [19]. This is an order of magnitude higher than those of traditional TE materials and even surpassing some metals with similar crystal structures (e.g., Ti, Mg, Zr, Co, Hf). This exceptional deformability allows single-crystal Mg_3Bi_2 to be easily bent, twisted, and undergo other plastic deformations at RT. In addition, the optimized $Mg_3Bi_{1.998}Te_{0.002}$ single crystal also exhibits a high *PF* of 55 $\mu W \cdot cm^{-1} \cdot K^{-2}$ and *ZT* of approximately 0.65 within the *ab*-plane at room-temperature, comparable to commercial n-type Bi_2Te_3-based materials. Based on this work, Hu et al. further investigated the underlying mechanism of the superior plasticity in single-crystal Mg_3Bi_2 using the integrated differential phase contrast technique [181]. They revealed the atomic distribution of heavy Bi and light Mg atoms. The results showed that the strain-induced helical dislocations drive interlayer slip on the (0001) plane was the microscopic mechanism of plastic deformation. The small size of Mg atoms led to weak interlayer bonding, allowing the low-modulus $Mg_2Bi_2^{2-}$ network to slide easily along the ab-plane. During sliding, the weak interlayer Mg-Bi bonds also maintain the overall structural integrity. Furthermore, the high TE performance along the *c*-axis (*PF* = 26.2 $\mu W \cdot cm^{-1} \cdot K^{-2}$) contributed to the high output performance of the out-of-plane F-TEG. The fabricated F-TEG exhibited a high ω_n of 8.1 $\mu W \cdot cm^{-1} \cdot K^{-2}$ under a temperature difference of 7.3 K. These studies demonstrate that high-performance, low-cost plastic inorganic Mg_2Bi_2-based materials are promising for advancing the development of flexible electronics.

4.2 Organic thermoelectric materials

The fast development of organic conductive polymers has shown the potential of conjugated polymers for flexible devices [182]. These polymers possess advantages like intrinsic flexibility, tunable molecular structures, solvent processability, and low κ [183]. However, their applications in TE field still face some challenges, such as strong coupling between σ and *S*, poor air stability of n-type doping, and relatively low carrier mobility [184]. To address these issues, molecular engineering strategies, including backbone modification, side-chain engineering, and donor-acceptor (D-A) structure design, have been developed. Combined with efficient chemical doping, these strategies have significantly enhanced the TE performance [185–187].

4.2.1 *Polyaniline (PANI)*

As a widely studied p-type conductive polymer, PANI has the characteristics of easy synthesis, low cost, adjustable doping level, and environmental stability [188]. However, the rigid parts in its molecular structure and the strong hydrogen bonds between molecules make it difficult to dissolve, which limits its application in the TE field [189]. Nevertheless, due to its reasonable σ, it is often composited with other high-performance TE materials through *in-situ* polymerization to introduce heterogeneous interfaces and create energy filtering effects [190]. For example, when composited with single-walled carbon nanotubes (SWCNTs), it improved the dispersion of SWCNTs in aqueous PEDOT:PSS and formed a large number of highly uniform dual-interfaces with more efficient energy filtering effect, thereby improving the TE properties [191]. Additionally, incorporating metal oxides or metal-doped oxide nanoparticles into the PANI matrix to enhance *S* represents an effective strategy for improving the TE performance of PANI [192–194]. Currently, the potential of PANI in TE field lies in its role as an important component with composite materials, which can synergistically optimize overall performance.

4.2.2 *Polypyrrole (PPy)*

Similar to PANI, the application of PPy in TE field benefits from its relatively high σ and stability. Particularly, its good biocompatibility gives it unique potential in self-powered wearable or implantable sensors for biomedical applications [195, 196]. However, its insoluble and infusible properties make it difficult to prepare high-quality films through solution processing. Therefore, its preparation primarily relies on *in-situ* polymerization, but this process is difficult to precisely control the thickness of the growth layer [197]. Qi et al. utilized a simple *in-situ* freezing interfacial polymerization technique to fabricate self-supporting PPy films with high σ [198]. Nevertheless, the TE properties of the pure PPy films remains not satisfactory, and they are more often used to enhance the conductivity of composites [199, 200]. However, its unique conjugated molecular structure enables strong absorption of solar radiation ranging from ultraviolet to near-infrared regions and efficient conversion into thermal energy. This property can be strategically utilized to establish larger temperature gradients in TE systems [201, 202].

4.2.3 *Poly(3-4 ethylenedioxythiophene) (PEDOT)*

PEDOT is currently the most promising material in the field of organic TE. Its core advantage lies in its ability to achieve extremely high σ, low κ, metallic and semi-metallic characteristic, good environmental stability and intrinsic flexibility, making it ideally suited for flexible devices [203, 204]. However, the inherent rigidity of PEDOT's conjugated backbone, strong interchain interactions and lack of soluble functional groups render it insoluble in water and most common organic solvents, severely limiting its processability and application. To address this problem, a template polymerization strategy employing water-soluble poly(sodium 4-styrenesulfonate) (PSS) has been adopted. During the polymerization of PEDOT, its positively charged backbone in the oxidized state forms a stable complex with negatively charged PSS anions via electrostatic interactions. The hydrophilic PSS chains encapsulate the hydrophobic PEDOT chain clusters, resulting in the formation of stable colloidal particles with a PEDOT-rich core and a PSS-rich shell. The sulfonate groups on the PSS shell undergo strong hydration with water molecules, enabling the entire PEDOT:PSS complex to disperse stably in aqueous solution, thereby resolving its processability issue. Unfortunately, the presence of an excess amount of the electrical insulative PSS greatly reduces the σ of PEDOT. And its further advancement is constrained by the inherent trade-off relationship between σ and *S*. Unlocking its full potential could rely on doping, secondary doping and dedoping, precise manipulation microstructure, constructing 3D conductive networks by compounding with inorganic nanomaterials [197, 205]. The process of secondary doping involves the addition of secondary dopants to the PEDOT:PSS suspension, which facilitates the removal of PSS chains and alters the conformation of the PEDOT chains from benzoid to quinone structure. This transformation enhances the π-π stacking of PEDOT chains and improves crystallinity, which leads to a reduction in the barrier for carrier transport [206, 207]. Dedoping aids in balancing the electrical parameters and optimizing the overall *PF* by reducing *n* [208, 209]. To eliminate the use of toxic organic solvents, biocompatible and non-toxic deep eutectic solvents have also been utilized to enhance the TE properties of PEDOT:PSS [210].

Furthermore, a sequential treatment utilizing both secondary doping and dedoping has been shown to simultaneously raise σ and S [211, 212].

4.2.4 poly(3-hexylthiophene) (P3HT)

P3HT, as a typical p-type conjugated polymer, has garnered significant attention in the field of TE due to its suitable band gap, solution processability, and environmental stability. Its thiophene backbone and the hexyl side chains on the thiophene rings provide a broad scope for tuning its charge transport properties. Mardi et al. investigated the influence of polymer molecular weight on dopant distribution [213]. The lower molecular weight tended to promote dopant aggregation, whereas longer polymer chains provided more spatial freedom, facilitating a more uniform distribution of additives. A large amount of works has shown that chemical doping demonstrates great potential in regulating the TE properties of P3HT, but the contradiction with the polymer orientation also limits the high σ of the material. Thermal annealing can be employed to modify the crystallinity and orientation of the material, thereby constructing more efficient charge carrier pathways [214]. To break through the limitation of low σ, Byeong et al. focused on establishing conductive pathways within the amorphous region [215]. They reduced the side chain density of P3HT and introduced small-sized π-π aggregates into the disordered matrix to promote the delocalization of carriers in the amorphous region, which led to a σ of 528.3 $S \cdot cm^{-1}$ and a PF of 126.9 $\mu W \cdot m^{-1} \cdot K^{-2}$.

4.2.5 Donor-Acceptor (D-A) polymers

The design of donor-acceptor (D-A) polymers aims to exploits the push-pull effect between donor and acceptor units through reasonable molecular structure [216, 217]. The push-pull effect refers to the phenomenon where the electron-rich donor units can push electrons and the acceptor units can pull electrons because of their strong electron attracting ability. The alternating D-A structure helps to create a flat energy band structure that facilitates electron transport along the polymer backbone. This strategy guarantees intrinsically high σ with minimal doping requirements, and breaks the trade-off between σ and S in traditional conductive polymers [218]. More importantly, this material system is expected to fill the gap in high-performance n-type organic materials, laying the foundation for the construction of all-organic TEDs [219, 220]. Thanks to the ingenious molecular design of organic chemistry, D-A polymers have a much broader design space. By selecting different structural polymer units, the band gap can be precisely controlled. Although there are still challenges in terms of synthesis complexity, doping kinetics, and long-term operational stability, the excellent molecular tunability and inherent solution processability of these polymers provide vast potential for their future TE applications [221].

4.3 Carbon-based materials

4.3.1 Carbon nanotubes

Carbon nanotubes (CNTs) have garnered significant attention in F-TE field due to their unique one-dimensional nanostructure, demonstrating exceptional electrical properties [4, 222]. Their extremely high carrier mobility enables the prepared macroscopic films to have extremely high σ values. More importantly, their superior mechanical flexibility and strength make them an ideal choice for the flexible substrates. However, their TE applications are limited by the high κ and low S. Many effective strategies have been developed to address these issues, such as chemical doping and hybridization. Chemical doping is the most effective method to achieve charge transfer between CNTs and electron donors or acceptors. Thus, it can precisely regulate the n and type. However, there is a critical challenge in n-type doping, since the injected high-energy electrons are easily captured by the surrounding oxygen. Hybridization strategy is the key to achieving performance breakthroughs. The energy filtering effect arises from the combination of CNTs with other functional materials like organic polymers or inorganic nanomaterials, which will enhance S. The advantages of each component can be synergistically combined to realize the improvement of ZT values by this method [222–224]. During the manufacturing process, CNTs tend to aggregate into bundles due to vdW forces, resulting in inhomogeneous dispersion in solution [225]. To solve this problem, surface modification strategies can improve dispersion and optimize interface characteristics through covalent grafting or surfactant encapsulation [226]. It should be noted that the solvent polarity significantly influences the structure of surfactants or polymers assembled on CNTs, which will affect the doping efficiency and control the transformation between p-type and n-type characteristics [227].

4.3.2 MXene

MXene, as a new type of 2D transition metal carbides/nitrides material, demonstrates great potential in the field of TE energy conversion due to its high σ, tunable surface chemistry, flexible layered structure, and rich elemental composition. Its inherent high metallic σ helps reduce energy conversion losses; while the modification of surface functional groups can regulate the electronic structures. And the customizable characteristics of MXenes provide possibilities for energy collection in various scenarios by designing different elemental compositions and functional groups [228]. For instance, the natural defects generated during chemical etching can be precisely controlled in content through electrochemical methods [229]. During electrochemical reduction, some -OH functional groups break, forming more oxygen vacancies and reducing interlayer spacing. These oxygen vacancies acted as donor defects and enhanced interlayer electron transmission, which led to an increase in n and carrier mobility simultaneously, while the S remained stable, ultimately boosting the PF by fourfold. On the other hand, the surface functional groups introduced during etching are prone to oxidation and degradation in an aqueous and oxygen-containing environment, resulting in severe attenuation of σ and TE performance. Vacuum annealing can remove these surface functional groups and change the work function of MXene. Furthermore, for 2D materials, interlayer structure engineering also serves as an effective strategy for optimizing their TE performance [230]. Wang et al. constructed MXene/organic superlattices through an exfoliation-self-assembly method [231]. The electron injection effect of the inserted organic molecules increased n. And subsequent annealing treatment removed interlayer water molecules, some surface groups, and edge TiO_2, enhancing interlayer coupling and carrier mobility. As a result, the σ of prepared film increased to 2.7×10^5 $S \cdot m^{-1}$, approximately five times higher than that of pristine MXene film, and the PF reached ~33 $\mu W \cdot m^{-1} \cdot K^{-2}$, representing an improvement of over eightfold.

4.3.3 Graphene

As another 2D material, graphene exhibits extremely high carrier mobility, conductivity, and outstanding mechanical strength and

flexibility [232, 233]. However, its relatively low S and high κ lead to a low ZT value. To improve the TE performance, some methods like the assembly of nanoribbons and the introduction of dopants or defects have been employed [234–236]. Significant advancements have been made by introducing graphene as a nanofiller into other TE material systems rather than only enhancing the intrinsic performance. This approach can give play to synergistic effects to overcome the performance limitations of single-component materials [237–239].

5 Film-based F-TEDs

In order to meet the requirements of complex curved surface heat sources, replacing the rigid ceramic substrate used in inorganic TEDs with flexible materials to closely adhere to the heat source surface is a feasible and straightforward method for fabricating F-TEDs. In particular, some advanced fabrication techniques, such as 3D printing, screen printing, vapor deposition, and magnetron sputtering, have been applied to the preparation of F-TEDs [39, 73, 240, 241]. These manufacturing technologies have provided significant assistance in improving F-TEDs' performance, flexibility, stability and production efficiency. As previously mentioned, certain ductile inorganic TE materials can be processed into thin-film forms and applied in F-TEDs due to their unique plasticity. Additionally, many organic polymer materials, including PEDOT, PANI, PPy, P3HT, PBTTT, etc., inherently exhibit promising TE properties and are considered as another effective pathway for realizing F-TEDs. Therefore, according to the composition of the thin-film F-TEDs, they are classified into two categories of F-TEDs based on flexible substrates and free-standing F-TEDs.

5.1 F-TEDs based on flexible substrates

5.1.1 *Integrate bulk TE materials on flexible films*

Currently, F-TEDs comprising of inorganic bulk TE materials are predominantly fabricated using the strategy of integrating them onto flexible substrates. The main advantage of this approach lies in the ability to directly apply many mature process technologies from traditional device fabrication to the manufacturing of flexible devices. Particularly, PI has gained significant favor among researchers due to its excellent flexibility, stability, and outstanding heat resistance [244, 245]. Additionally, polydimethylsiloxane (PDMS) and ultra-soft Ecoflex silicone rubber are also frequently chosen as flexible basements [43, 73, 246]. For instance, as shown in Fig. 6(a), a F-TEG was previously fabricated by connecting commercial Bi_2Te_3 and Sb_2Te_3 TE legs using liquid metal on a thermosetting PI substrate featuring dynamic covalent bonds [242]. While the PI with dynamic covalent bonds and the liquid metal material endowed the device with new characteristics such as recyclability, self-healing capability and stretchability, the significant difference in mechanical stiffness between the flexible polymers and the rigid TE legs made the junctions highly prone to fracture, which limited the tensile resistance of the device. To address this challenge, many design concepts from stretchable flexible circuits have been adapted for F-TEDs. Yang et al. utilized wavy serpentine interconnects on a flexible Ecoflex substrate to link arrays of nanolayered p-type Sb_2Te_3 and n-type Bi_2Te_3 TE legs prepared via hot pressing (Fig. 6(b)) [46]. The entire device exhibited an extensibility exceeding 50% and could conform to various curved surfaces. Simultaneously, the prepared 10×10 array had a low internal resistance of only 22 ohms, delivering a P_{out} of approximately 0.15 mW·cm^{-2} under a temperature difference of

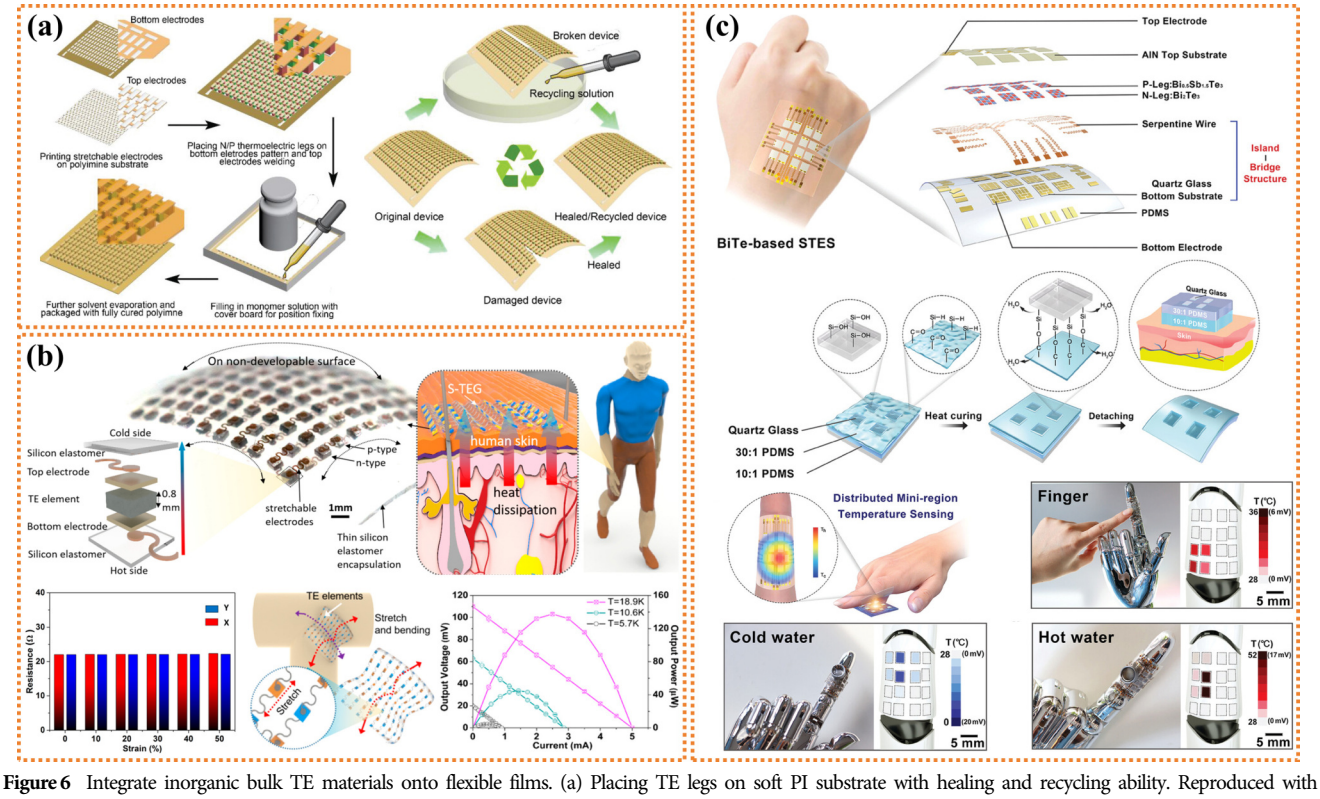

Figure 6 Integrate inorganic bulk TE materials onto flexible films. (a) Placing TE legs on soft PI substrate with healing and recycling ability. Reproduced with permission from Ref. [242], © WILEY-VCH, 2021. (b) Wavy serpentine interconnects for stretchable TEGs. Reproduced with permission from Ref. [46], © American Chemical Society, 2020. (c) Interfacial chemical bonds located between TE elements and the flexible substrate for solving interfacial failure. Reproduced with permission from Ref. [243], © WILEY-VCH, 2023.

19 K. Similarly, Kang et al. mitigated interfacial failure caused by modulus mismatch between rigid islands and the flexible substrate (PDMS) by designing the interfacial chemical bonds [243]. As demonstrated in Fig. 6(c), they fabricated a 4×4 vertical temperature sensing array with good extensibility and distributed sensing characteristics. This sensing unit could withstand up to 30% tensile strain, which is the maximum strain of human skin, and demonstrated fast response time (0.157 s), high sensitivity (729 μV·K^{-1}), and high spatial resolution (2.75 mm ×2.75 mm), showing great potential of self-powered temperature sensing.

5.1.2 *Deposit on flexible films*

However, in the fabrication process of the aforementioned devices, each individual TE leg was prepared by separate cutting. Due to limitations in machining precision and material brittleness, it is difficult to achieve large-scale integration and inevitable for performance loss during device assembly. With the emergence of various micro/nano fabrication technologies, the number of TE couples in a single device can be significantly increased, which markedly enhances P_{out} of the device and also shows great application potential in the field of electronic device cooling. Vacuum thermal evaporation method, centered on physical vapor deposition, enables the preparation of micron-scale or even atomic-scale thin films by precisely controlling parameters such as vacuum level, temperature, and evaporation rate. Building on this, improved multi-source co-evaporation techniques allow for the preparation of alloy or multilayer films [247–249]. As exhibited in Fig. 7(a), Yang et al. utilized vacuum thermal co-evaporation method to prepare Te-doped Ag_2Se films on flexible PI substrates [245]. The Te doping reduced the formation energy of the (00*l*) planes, enhancing both the film uniformity and the (00*l*) preferential orientation, which led to higher carrier mobility. Furthermore, Te doping widened the band gap, increasing the *S* and *PF*. Concurrently, the introduction of Te_{Se} point defects caused phonon scattering, reducing the film's κ to 0.71 W·m^{-1}·K^{-1}. As a result, the Ag_2Se film with 3.2 at.% Te doping achieved a high *ZT* value of 1.27 at 363 K. Following, an organic polymer protective layer was spun coated on its surface to enhance the film's flexibility. After 1000 bending cycles with a radius of 6.3 mm, the resistance change rate was only 2.5%. Finally, a F-TED assembled from a pair of p-type Sb_2Te_3 and n-type Ag_2Se films achieved a ω of 1.5 mW·cm^{-2} at ΔT = 20 K [245]. Similarly, magnetron sputtering also falls under the category of physical vapor deposition, which is an advanced technique conducted electric and magnetic fields to control Ar ions for bombarding the target substrate in a vacuum environment. This technology could achieve target atoms sputtering and depositing onto a substrate to form a thin film. By covering the patterned mask template on the substrate, it is possible to achieve the one-step fabrication of multiple TE materials, avoiding subsequent assembly steps and improving overall device consistency [20, 86, 250]. Figure 7(b) displayed a meaningful attempt by utilizing magnetron sputtering technology to fabricate an ultra-thin TED with 572 TE modules [251]. As shown in Fig. 7(c), Zhang et al. developed a F-TED with a vertical π-type structure using a pulse electroplating process [252]. The main fabrication process was as follows: First, a 100 nm thick Au electrode was deposited on a PI substrate. Next, the bottom electrode and connecting lines were patterned through photolithography and wet etching. Then, photolithography was performed again to etch holes with a diameter of 200 μm in SU-8 mold above each electrode. Subsequently, Bi_2Te_3 and Sb_xTe_y TE pillars were alternately deposited into each hole using pulse electroplating. Finally, the top electrodes were prepared, and the photoresist was removed. Precise control over the number and duration of the electroplating cycles resulted in deposited TE pillars with good uniformity and nearly identical heights. More importantly, the electrical contact between the TE pillars and the electrodes was improved by adjusting the electroplating conditions and applying a deposition-dissolution treatment. After optimizing the height and quantity of the TE pillars, the device achieved a ω of 14.3 mW·cm^{-2} [252].

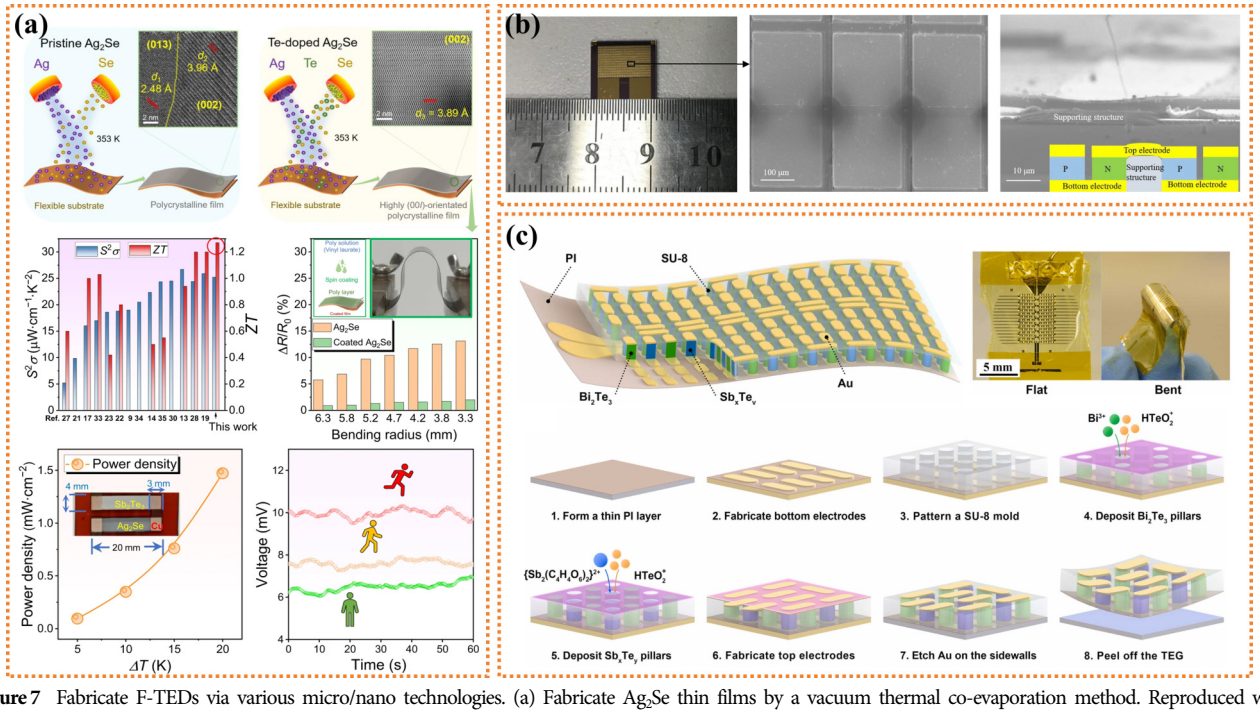

Figure 7 Fabricate F-TEDs via various micro/nano technologies. (a) Fabricate Ag_2Se thin films by a vacuum thermal co-evaporation method. Reproduced with permission from Ref. [245], © Yang, D. et al. 2024. (b) Prepare TE device through alternate magnetron sputtering. Reproduced with permission from Ref. [251], © Liu, Y. et al. 2020. (c) Develop flexible micro-TEG through pulse electroplating. Reproduced with permission from Ref. [252], © Elsevier Ltd. 2023.

5.1.3 *Print on flexible films*

While the aforementioned micro/nano fabrication processes show great potential for device miniaturization and high-density integration, their high cost and complex procedures often limit large-scale applications. Screen printing technology, a relatively inexpensive and scalable method for producing flexible films, has been widely adopted in the TE field in recent years [36, 240]. Bi_2Te_3 is a commercially successful inorganic TE materials with outstanding performance near room temperature. However, Bi_2Te_3 films prepared via screen printing typically suffer from poor density, leading to low σ and a tendency to crack under bending. That limits the overall device performance [251, 253]. Therefore, the ink formulation and sintering process are crucial factors in obtaining flexible films with high TE properties [32]. Figure 8(a) indicated single-crystal Ag-doped Bi_2Te_3 nanosheets and Te nanorods with controllable sizes via a specially designed solvothermal method [254]. Subsequently, highly (00*l*)-oriented Bi_2Te_3 films were obtained by screen printing and spark plasma sintering (SPS) technology. In this process, the Te nanorods acted as a "nano-binder", effectively bridging the Bi_2Te_3 nanosheets, significantly enhancing the film's density, and triggering an effective energy filtering effect. The results demonstrated that by optimizing n and mobility while maintaining a high S, a high PF of 18.5 $\mu W \cdot cm^{-1} \cdot K^{-2}$ was achieved at 303 K. Furthermore, a flexible device assembled on a PI substrate using two pairs of n-type Bi_2Te_3 and p-type $Bi_{0.4}Sb_{1.6}Te_3$ achieved a high ω_n of 3 $\mu W \cdot cm^{-2} \cdot K^{-2}$. Additionally, 3D printing, as a rapidly developing additive manufacturing technology, can construct block components layer by layer based on 3D computer-aided design models. As demonstrated in Fig. 8(b), Xu et al. utilized extrusion-based 3D printing for the high-efficiency, large-scale fabrication of high-performance TE cooling devices [244]. By optimizing the ink composition and concentration, n-type Ag_2Se and p-type $(Bi,Sb)_2Te_3$ inks suitable for 3D printing were obtained. The n-type ink was prepared by mixing Ag_2Se particles with a size range from 50 to 300 nm with glycerol at a 1:2 mass ratio. The p-type ink was formulated by mixing $Bi_{0.5}Sb_{1.5}Te_3$ powders with two inorganic solid binders, Bi nanoparticles and Sb_2Te_4 chalcogenide (ChaM), in ethylene glycol and xanthan gum.

During the subsequent sintering process for solvent removal, interfacial bonding between the inorganic particles was promoted, resulting in high ZT values of 1.42 for p-type and 1.3 for n-type at room temperature [244]. This work provides guidance for developing high-performance semiconductor particle ink formulations suitable for 3D printing. As seen in Fig. 8(c), Liu et al. controlled the ink formulation and printing parameters to fabricate TE arrays with micro-scale resolution and controllable dimensions using inkjet printing technology [39]. By further tuning the film microstructure, the printed Ag_2Se/15% Ag composite film exhibited (00*l*) texture characteristic, achieving a high PF of 1097 $\mu W \cdot m^{-1} \cdot K^{-2}$ at 377 K. Benefiting from the high integration density of the printed device, a record-high ω_n of 2 $\mu W \cdot K^{-2} \cdot cm^{-2}$ was achieved. The device also demonstrated excellent flexibility with less than 10% promotion in resistance after 3000 consecutive bending cycles under different radii. These works provide guidance for developing high-performance semiconductor particle ink formulations suitable for printing.

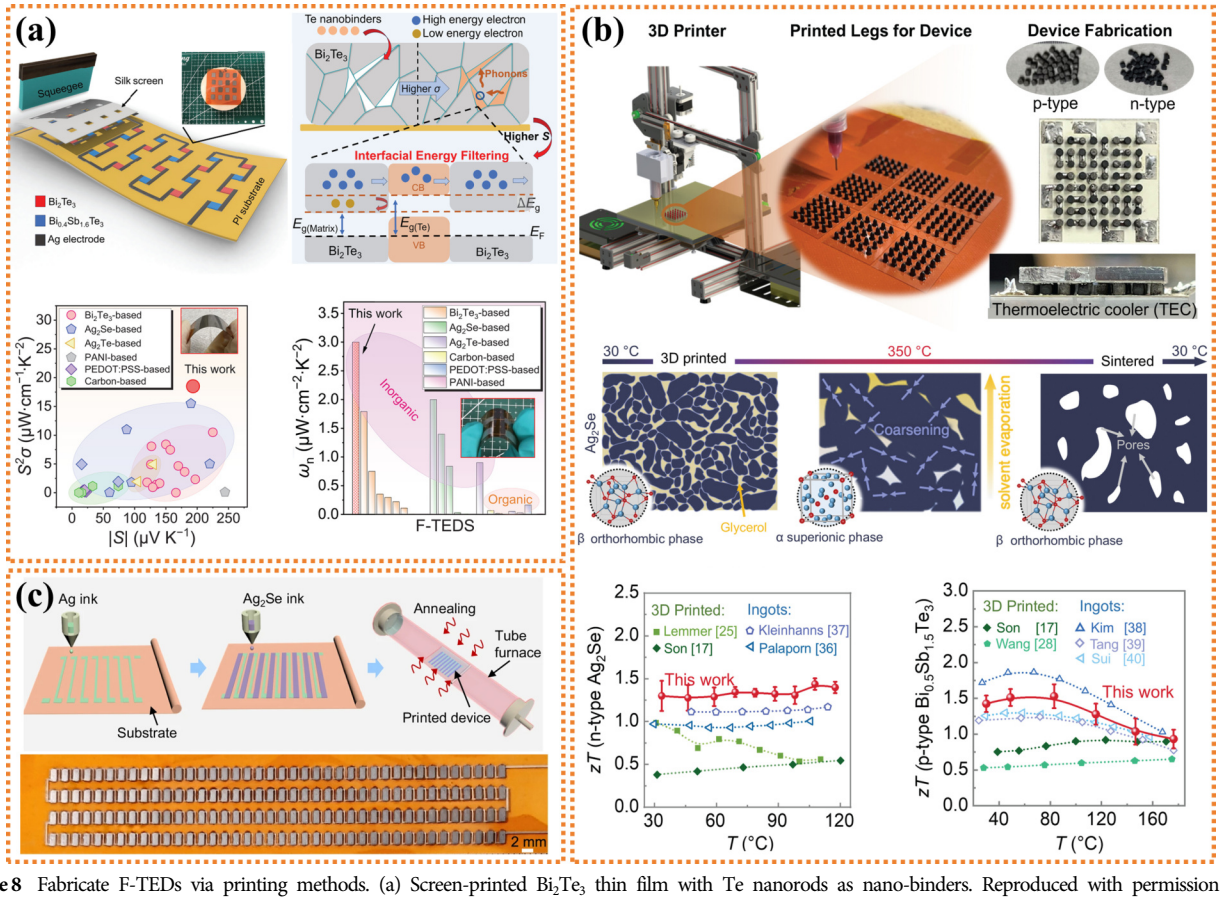

Figure 8 Fabricate F-TEDs via printing methods. (a) Screen-printed Bi_2Te_3 thin film with Te nanorods as nano-binders. Reproduced with permission from Ref. [254], © Chen, W. Y. et al. 2024. (b) 3D-printered TE materials enhanced by interfacial bonding. Reproduced with permission from Ref. [244], © Xu, S. D. et al. 2025. (c) Fully inkjet-printed Ag_2Se-based F-TEDs. Reproduced with permission from Ref. [39], © Liu, Y. et al. 2024.

5.2 Free-standing F-TEDs

Numerous F-TEDs with application potential have been fabricated by combining inorganic TE materials on flexible substrates in the past decade. However, this fabrication strategy also faces several limitations. Firstly, the flexible substrates used in the process are mostly polymer materials, which generally cannot withstand high processing temperatures and lack sufficient heat resistance. Secondly, the inherently low κ of polymers introduces high interfacial thermal resistance, reducing the temperature difference across the TE materials and limiting the device's power output. Finally, the significant modulus mismatch between the flexible polymers and the rigid inorganic TE materials makes the interface prone to delamination under long-term bending, stretching, and other deformations, leading to device failure. Consequently, the development of free-standing F-TE films without flexible substrates has attracted considerable attention in recent years [240, 255]. Next, we will introduce several common strategies for preparing free-standing F-TE films. Firstly, many ductile inorganic materials can be processed into film form through methods such as peeling or rolling. Secondly, self-supporting flexible films can be obtained after removing the growth substrate. Finally, many polymers that inherently possess TE properties can be further modified to enhance their performance.

5.2.1 *Inorganic free-standing films*

Due to the metal-like processability exhibited by materials such as Ag_2Q (Q = S, Se, Te) and AgCuQ, inorganic TE films with certain flexibility can be readily obtained by processing their ingots. For instance, Liang et al. effectively developed a few-micron-thick fully inorganic silver sulfide TE film using simple rolling process (Fig. 9(a)) [256]. The $Ag_2S_{0.45}Se_{0.45}Te_{0.1}$ film achieved a ZT value of 0.47 at room temperature, and a TEG fabricated with this material realized a V_{OC} of 1.19 mV and a ω of 1.8 mW·m^{-2}. As shown in Fig. 9(b), Gao et al. reported that various bulk brittle semiconductor materials, such as Cu_2Se, Ag_2Se, and $Bi_{90}Sb_{10}$, can be plastically deformed via warm metal processing. That was, they can be processed like metals at temperatures of 400–500 K into self-supported, large-area, high-quality films with thicknesses ranging from the macroscopic scale down to the micrometer scale [257].

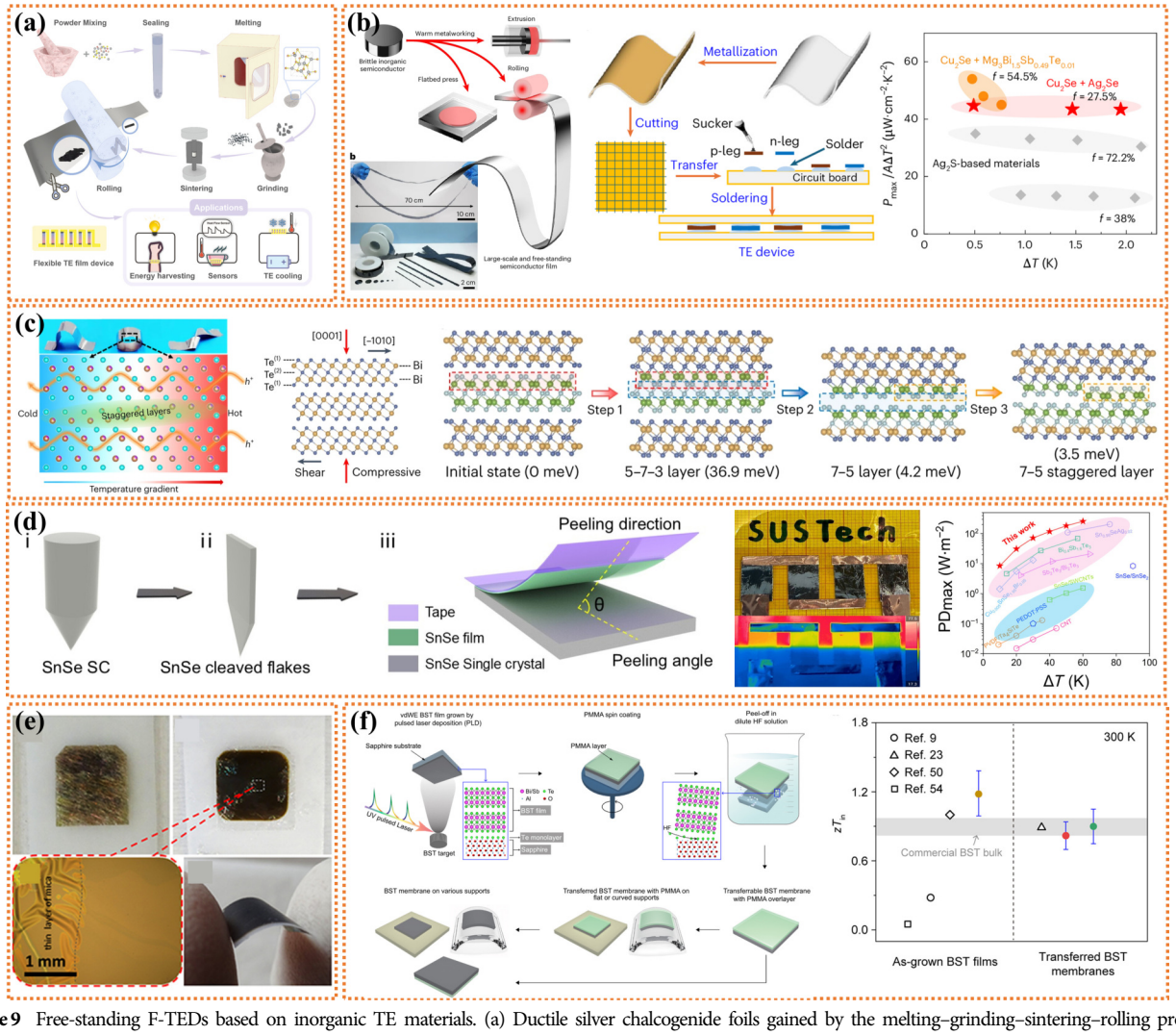

Figure 9 Free-standing F-TEDs based on inorganic TE materials. (a) Ductile silver chalcogenide foils gained by the melting–grinding–sintering–rolling process. Reproduced with permission from Ref. [256], © American Chemical Society 2022. (b) Warm-metalworking techniques for plastic manufacturing in brittle semiconductors. Reproduced with permission from Ref. [257], © Gao, Z. Q. et al., under exclusive licence to Springer Nature Limited 2025. (c) Flexible Bi_2Te_3 films exfoliated from corresponding single crystals. Reproduced with permission from Ref. [12], © Lu, Y. et al., under exclusive licence to Springer Nature Limited 2023. (d) Single-crystal SnSe film obtained by mechanical exfoliation. Reproduced with permission from Ref. [41], © American Chemical Society 2025. (e) The self-supported $Ca_3Co_4O_9$ thin films acquired through removing sacrificial substrate. Reproduced with permission from Ref. [258], © American Chemical Society 2017. (f) The exfoliation and transfer of vdWE $Bi_{0.5}Sb_{1.5}Te_3$ thin film. Reproduced with permission from Ref. [259], © American Chemical Society 2021.

The films processed in this way retained the excellent and tunable physical properties of the bulk materials, such as carrier mobilities as high as approximately 5000 $cm^2 \cdot V^{-1} \cdot s^{-1}$, and σ tunable over six orders of magnitude via chemical composition adjustment. A case study on a film-based TED demonstrated an ultra-high ω_n of 43–54 $\mu W \cdot cm^{-2} \cdot K^{-2}$. Interestingly, similar to the mechanical exfoliation of graphene, Lu et al. successfully exfoliated layered Bi_2Te_3 films by adhering Scotch tape closely onto the (000*l*) cleavage plane of a single-crystal Bi_2Te_3 (Fig. 9(c)) [12]. The study found that atomic rearrangement around the vdW gaps during exfoliation led to the spontaneous formation of a staggered-layer structure. This structure allowed stress propagation during bending, resulting in excellent flexibility of the film even after 1000 bending cycles. Simultaneously, it minimized the degradation of carrier transport along the direction of the thermal gradient. At room temperature, the n-type and p-type materials achieved *PF*s of 4.6 and 4.2 $mW \cdot m^{-1} \cdot K^{-2}$, respectively. This finding inspired to use this method exfoliating other layered inorganic materials with high *ZT* values, such as Bi_2Se_3 and SnSe. Figure 9(d) displayed high-quality SnSe single-crystal films obtained by combination of growing SnSe single crystals using the Bridgman method and the tape exfoliation technique [41]. These films maintained good flexibility while achieving a high *PF* of 24 $\mu W \cdot cm^{-1} \cdot K^{-2}$ at 300 K. Furthermore, a F-TED was designed and assembled on a PI substrate using two pairs of SnSe and $Bi_2Te_{2.7}Se_{0.3}$ films, achieving a ω of 257.4 $W \cdot m^{-2}$ under 60 K temperature difference. However, this method is not universally applicable to all inorganic TE semiconductors. Developing new inorganic TE materials with intrinsic plasticity and improving the TE performance of existing materials remain the research focus.

In contrast to the above top-down fabrication strategies, self-supported inorganic TE films can also be prepared using bottom-up method [260–262]. This approach requires a weak bond between the inorganic material and the substrate, allowing the substrate to be easily removed. As exhibited in Fig. 9(e), Paul et al. used mica as a sacrificial substrate to synthesize flexible inorganic calcium cobaltate ($Ca_3Co_4O_9$) films via reactive radio-frequency magnetron cosputtering [258]. Due to the weakly bound layered aluminosilicate structure of mica, the $Ca_3Co_4O_9$ films could be easily peeled off the substrate without compromising their functionality. Within the temperature range from room temperature to 673 K, the *PF* value of prepared flexible film exhibited nearly constant, approximately 1.2 $\mu W \cdot cm^{-1} \cdot K^{-2}$. Furthermore, there was very little performance change during the bending test with a radius of 14 mm. Additionally, van der Waals epitaxy (vdWE) is a technique that utilizes weak intermolecular forces between the inorganic film and the substrate to realize epitaxial growth. Its most significant feature is that it overcomes the strict requirements for lattice matching in traditional epitaxy, making it possible to grow high-quality, low-defect single-crystal films on any substrates [263–265]. As shown in Fig. 9(f), Fu et al. grew vdWE $Bi_{0.5}Sb_{1.5}Te_3$ (BST) films on a sapphire substrate using pulsed laser deposition [259]. Subsequently, the films were separated from the substrate via chemical etching and successfully transferred onto flat or curved glass and flexible PET. During the epitaxial growth, the weak vdW interaction between a pseudomorphic Te monolayer formed *in situ* on the sapphire substrate and the Te atomic layers in the BST film reduced the traditional clamping effect between the epitaxial film and the substrate. This ensured that the film could be separated from the substrate by selectively etching the Te monolayer using dilute HF solution. To protect the BST film during chemical etching and facilitate its transfer, a layer of poly(methyl methacrylate) (PMMA) approximately 100 nm was spin-coated onto the BST film and completely removed after the transfer was complete. Furthermore, to achieve strong adhesion to the carrier, the BST film was baked at 373–393 K. Because the BST film maintained high crystallinity during the peeling and transfer processes, it achieved a high *ZT* value of 0.9 at 300 K.

5.2.2 *Organic free-standing films*

In contrast to inorganic TE materials, the applications of conductive polymers in the TE field are constrained by their lower conductivity and the instability of n-type doping [42, 266, 267]. To address these challenges, researchers have employed molecular chain engineering. The TE properties of conjugated conductive polymers are closely related to their structural characteristics. Therefore, regulation of the polymer backbone and side chains can significantly influence their charge transport behavior and electrical properties. A fully conjugated backbone with alternating single and double bonds, formed by sp^2-hybridized carbon atoms creating a delocalized π-electron system, provides a high-speed channel for charge transport. The conjugation length and rigidity of backbone structure are the core factors determining the upper limit of its TE performance, as they fundamentally dictate the material's charge transport capability and conduction type through its band structure [268–270]. The donor-acceptor (D-A) alternating structure can systematically reduce the band gap and precisely control the energy level through the intramolecular charge transfer effect between the electron donor and acceptor units [57]. As shown in Fig. 10(a), Tang et al. summarized the optimal TE performance of doped conjugated polymers in a coordinate diagram through an extensive literature review [56]. The results indicated that the donor (D) units in D-π structure polymers helps with a higher degree of charge transfer with dopants, thus having a larger σ. In contrast, the acceptor (A) units in D-A type polymers promote energy disorder along the π-backbone, favoring a higher *S*. Most high-performance p-type π-conjugated polymers belong to the D-π structure. Considering the application of polymer TE materials in wearable devices, a high *S* is often required due to small temperature gradients. D-π polymers seem to be difficult to meet this demand. Therefore, the D-A structure could be a better platform for achieving superior TE performance. But simultaneously realizing higher σ while maintaining an excellent *S* (>100 $\mu V \cdot K^{-1}$) remains a primary challenge. Unlike the situation in p-type polymers, no obvious aggregation of data points was observed for n-type polymers. The main reason for this phenomenon is the lower n-type doping efficiency [56]. To match the σ of p- type polymers and construct all-polymer F-TEDs, A-π- and A-A-type structures might be better platforms. Higher n-type doping efficiency can be achieved through rational design of the polymer π-backbone [270]. Additionally, the polymer backbone structure that tends to a planar conformation will facilitate ordered intermolecular packing, thereby enhancing mobility [271, 272]. As can be seen in Fig. 10(b), Sun et al. prepared a structurally simple quinoid molecule, thieno[3,2-b]thiophene-2,5-dione (TTD), with small steric hindrance, strong electron-deficient character, and absence of isomers via a one-step synthesis [273]. Single-crystal structure analysis of TTD confirmed its quinoidal character, exhibiting a fully planarized backbone structure and a π-π stacking distance of 3.45 Å. Thanks to the strong electron affinity and quinoidal nature of the TTD unit, the polymers PQD and PQTD exhibited low lowest unoccupied molecular orbital (LUMO) energy levels of

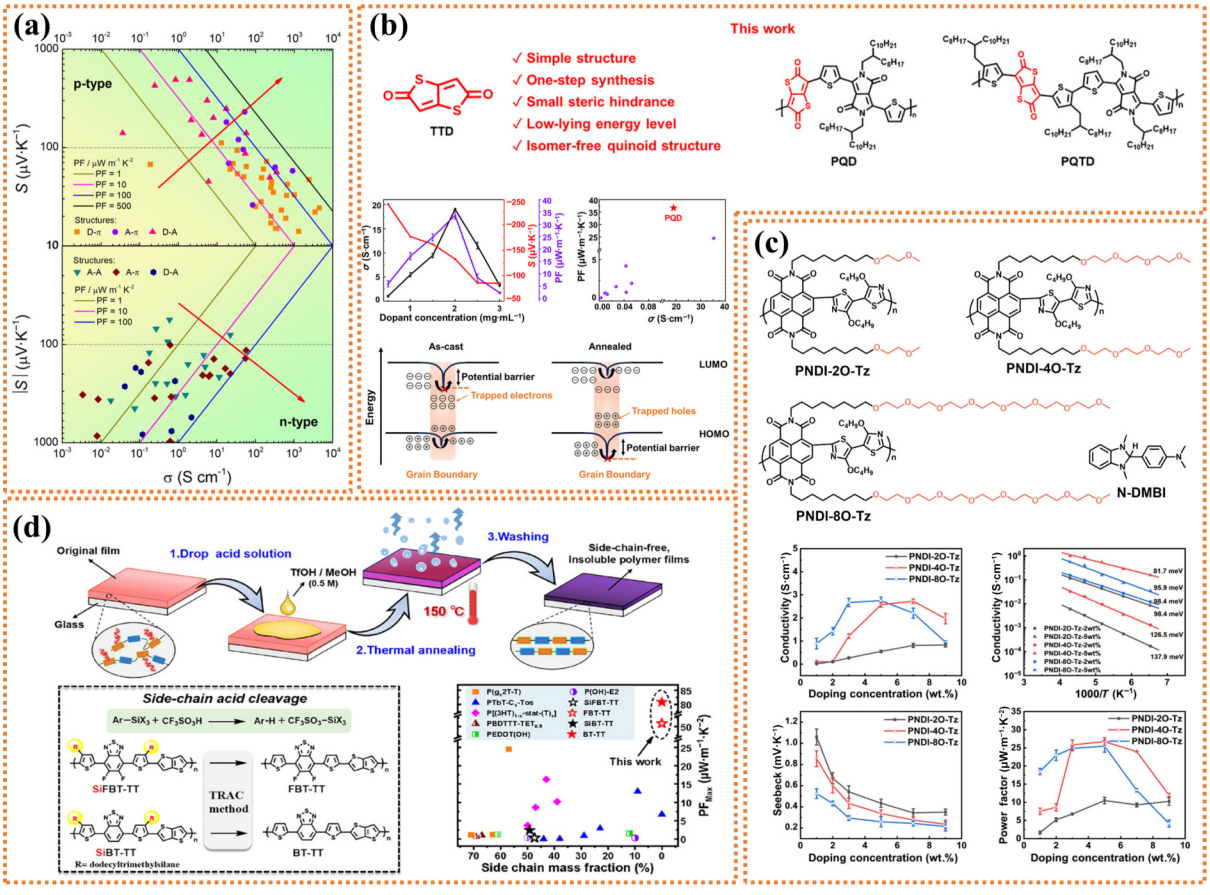

Figure 10 Regulate molecular chain structures to enhance the TE performance of free-standing organic film. (a) Summary of the best-performing p- and n-type Donor-Acceptor polymeric TE materials in literatures. Reproduced with permission from Ref. [56], © American Chemical Society, 2022. (b) Molecular design to gain a polymer backbone with planar conformation. Reproduced with permission from Ref. [273], © Wiley-VCH GmbH 2025. (c) Regulation of the side chain length. Reproduced with permission from Ref. [274], © American Chemical Society 2024. (d) TRAC method to remove silane side chains. Reproduced with permission from Ref. [275], © Wiley-VCH GmbH 2025.

–3.91 and –3.73 eV, respectively, and displayed a thermal population of radical states. Additionally, PQD and PQTD had n-type transport characteristics, with optimized electron mobilities reaching 0.19 and 0.011 $cm^2 \cdot V^{-1} \cdot s^{-1}$, respectively. Notably, the carrier polarity in organic field-effect transistors (OFET) based on PQD and PQTD transitioned from p-type to ambipolar, and eventually to n-type during thermal annealing. This transformation stemmed from the enhancement of crystallinity induced by the annealing treatment, which reduced the barrier for electron transport but increased the barrier for hole transport. After being n-type doped with the dopant molecule TAM, the PQD film gained a high σ of 19.2 $S \cdot cm^{-1}$ and a *PF* of 36.7 $\mu W \cdot m^{-1} \cdot K^{-2}$, with the *PF* being the highest value reported among n-type conjugated polymers containing quinoid structures [273].

The side chain structures also significantly influence the properties of TE materials. The effect of side chains on molecular packing and microscopic morphology can modulate charge transport. Introducing polar side chains can create stronger interactions with dopants, promoting a more uniform distribution of the dopants in the matrix. This improved the compatibility and prevented aggregation, which will damage the electrical performance. Thereby, the balance between σ and *S* was achieved through fine regulation of *n*. Furthermore, side chains with appropriate length and structure can induce ordered π-π stacking of the rigid conjugated backbone, forming crystalline or semi-crystalline regions, thereby significantly enhancing carrier mobility and conductivity [276–278]. Long and flexible alkyl side chains can increase the isolation and mobility among backbones, thereby improving the solubility to meet the requirements of solution processing. However, overly long side chains may cause molecular chain entanglement. What is more serious is that longer alkyl side chains will lead to excessive isolation and hinder charge transmission. For example, Peng et al. synthesized three naphthalenediimide (NDI)-based conjugated polymers with amphiphilic side chains that possessed ethylene glycol end-groups of varying lengths, as seen in Fig. 10(c) [274]. And the effects of side chain polarity, conformation, and length on doping efficiency, charge mobility, and TE performance were systematically investigated. The study found that the polarity of the conjugated polymer increased with the length of the ethylene glycol-terminated side chain. Simultaneously, the side chains adopted a more extended conformation in solution, which reduced the spatial obstruction to backbone π-stacking, thereby enhancing dopant-polymer compatibility. This was beneficial for improving both carrier mobility and doping efficiency. However, excessively long insulating side chains also dilute the charge transport pathways. Consequently, PNDI-4O-Tz, with a medium-length side chain, exhibited the best performance, achieving a σ of 2.76 $S \cdot cm^{-1}$ and *PF* of approximately 28.4 $\mu W \cdot m^{-1} \cdot K^{-2}$ [274]. To avoid the adverse effects of insulating side chains on the conductivity of conjugated polymers, Zhong et al. ingeniously introduced silane side chains into a benzothiadiazole (BT)-based conjugated polymer (Fig. 10(d)) [275]. After the polymer film was prepared via solution processing, the silane side chains were

rapidly cleaved under heating using trifluoromethanesulfonic (TfOH) acid. This termed thermal-assisted rapid acid cleavage (TRAC) method successfully helped the molecular packing orientation shift from a mixed face-on/edge-on to a predominantly edge-on orientation. Concurrently, the lamellar spacing and π-π stacking distance decreased significantly, indicating intense molecular packing of the skeleton. This markedly promoted backbone delocalization and facilitated rapid charge transport. Finally, the BT-TT film doped by $FeCl_3$ achieved an exceptional σ of up to 730 S·cm^{-1} and a *PF* of 81 μW·m^{-1}·K^{-2}, respectively [275]. Similarly, Li et al. reported a n-type conjugated polymer, P(Py2FT), characterizing a cationic backbone without side chains [279]. Compared with other polymers with long side chains, this polymer exhibited a shorter lamellar distance and a comparable π-π stacking distance. Simultaneously, the cationic units significantly increased the electron density of the LUMO along the entire connecting chain. This led to a shortening of C-C single bonds and an enhancement of backbone planarity upon doping. Ultimately, the P(Py2FT) film demonstrated an n-type σ of 28.1 S·cm^{-1} and a *PF* of 28.7 μW·m^{-1}·K^{-2}. These results indicate that side-chain-free polymer design is an effective method to enhance the electrical transport properties of TE polymers.

The aggregated state of polymers also plays a crucial role in their TE properties. Therefore, it can be significantly enhanced by precisely controlling their microstructural orientation, such as chain alignment and crystalline domain orientation. By applying external forces to make the polymer chains preferentially align along the charge transmission direction, highly ordered crystalline domains can be formed, which markedly reduces grain boundary scattering and improve the carrier mobility along the orientation direction. For this purpose, researchers have developed a series of physical and chemical methods to induce and optimize the microstructural orientation of polymers. Inducing the orientation of polymer chains through the shear force during the solution processing is the commonly used and most scalable method. That is, move the coating rod on the substrate to make the polymer solution flow under the shear force, and the molecular chains are straightened and aligned in the flow direction. As shown in Fig. 11(a), Wu et al. synergistically optimized TE property of a thiophene-based polymer thin film via blade coating, combining with the novel conformational locking molecular structure design [280]. Additionally, mechanical stretching is another common method for controlling the polymer's aggregated structure [281, 282]. In addition to the aforementioned physical methods, Chen et al. employed a chemical blending method by adding a small amount of nucleating agents to a thiophene-based polymer to achieve controllable modulation of the film's crystallization behavior (Fig. 11(b)) [283]. By adjusting the amount of nucleating agent, they successfully reduced the grain boundary resistance and promoted crystalline order within domains, thereby enhancing *PF* to 1894 S·cm^{-1}. Beyond microstructural orientation, manipulating the film structure through post process to reduce κ has also been exploited to improve TE performance. For example, Fig. 11(c) described a porous polymer PDPPSe-12 film using microstructure engineering, which exhibited not only high TE performance but also rich structural colors [43]. The porous structure enhanced phonon-like scattering, resulting in a reduction of κ over 50% for the film. This led to an increase in *ZT* value by 170%, reaching 0.52 at 363 K. The highly ordered porous structure endowed the PDPPSe-12 film with rich structural colors and excellent stretchability. Such high-performance, colorful and stretchable porous TE polymer has considerable application prospects for wearable energy harvesting. As depicted in Fig. 11(d), Wang et al. achieved a high *ZT* value by creating TE plastics with a periodic double-heterojunction architecture [47]. Each period consisted of two polymers forming sub-10 nm heterojunction layer and interpenetrating bulk-heterojunction interfaces. Surprisingly, such geometric configuration enables highly efficient charge transport while generating greatly increased interfacial phonon-like scattering, resulting in a remarkable suppression of κ by more than 60%. Compared to the single polymer, a *ZT* value as high as 1.28 was reached at 368 K. This property surpassed that of existing F-TE materials and commercial TE materials. What's more, the compatibility of this multi-heterojunction structure with solution-coating technology can meet the requirements for fabricating large-area F-TEDs.

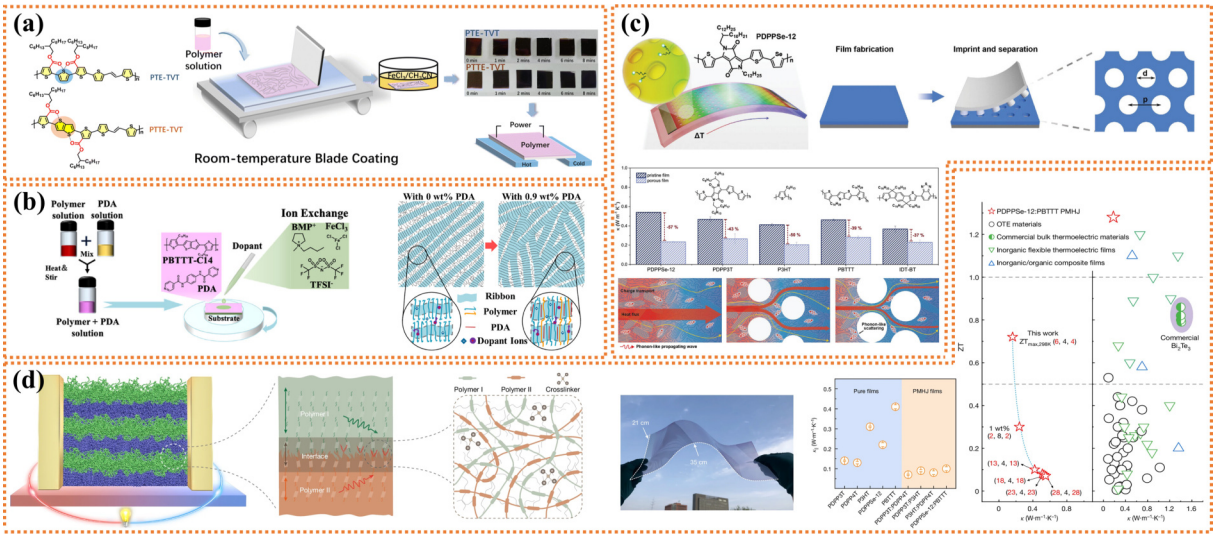

Figure 11 Regulate microstructural alignment and membrane structure to enhance the TE performance of free-standing organic film. (a) Induce the orientation of polymer chains through the shear force by blade coating. Reproduced with permission from Ref. [280], © The Royal Society of Chemistry 2023. (b) Add nucleating agent to promote semicrystalline conducting polymer crystallization. Reproduced with permission from Ref. [283], © Wiley-VCH GmbH 2025. (c) Introduce periodic porous structures to reduce the thermal conductivity of the film. Reproduced with permission from Ref. [43], © Wiley-VCH GmbH 2024. (d) Multi-heterojunctioned structure to reduce the thermal conductivity of the film. Reproduced with permission from Ref. [47], © Wang, D. Y. et al. under exclusive licence to Springer Nature Limited 2024.

5.2.3 *Inorganic/polymer composite free-standing films*

Benefiting from the solution processability of organic polymers, inorganic TE fillers can be introduced into organic polymer matrices or carbon materials via simple solution blending or *in-situ* synthesis methods. Subsequently, flexible self-supported TE films can be readily constructed using techniques like casting, spin-coating, printing, or vacuum filtration. The energy barriers that form at interfaces between inorganic fillers and the matrix can filter out low-energy charge carriers, which results in an enhanced *S*. To achieve higher TE performance, a high loading of fillers is usually required. Therefore, it is particularly important to ensure their uniform dispersion within the polymer solution and prevent agglomeration or sedimentation during preparation. As shown in Fig. 12(a), Culebras et al. synthesized positively charged PEDOT nanoparticles (PEDOT:NPs) dispersible in water and used them as a structural directing agent [284]. Employing an electrostatic layer-by-layer self-assembly method, they successfully deposited anionic PEDOT:PSS-stabilized double-walled carbon nanotubes (DWCNTs) and PEDOT:NPs aqueous solutions alternately onto a substrate, ultimately obtaining a fully organic composite film with hierarchical architectures. The results indicated that the highly ordered 3D conjugated network formed between the DWCNTs and the PEDOT matrix via strong π-π interactions facilitated charge transport within the film. A 20-bilayer film achieved a σ of 744 S·cm^{-1}, a *S* of 83 μV·K^{-1}, and a *PF* of 512 μW·m^{-1}·K^{-2} [284]. In another work, Zhang et al. prepared a self-supported flexible Ag_2Se/carbon composite film by screen-printing a formulated Ag_2Se/PVP/EG ink onto a PI substrate, followed by annealing in a vacuum furnace (Fig. 12(b)) [240]. During high-temperature annealing, the PVP gradually pyrolyzed and carbonized. Concurrently, the evaporation of EG from the bottom to the top

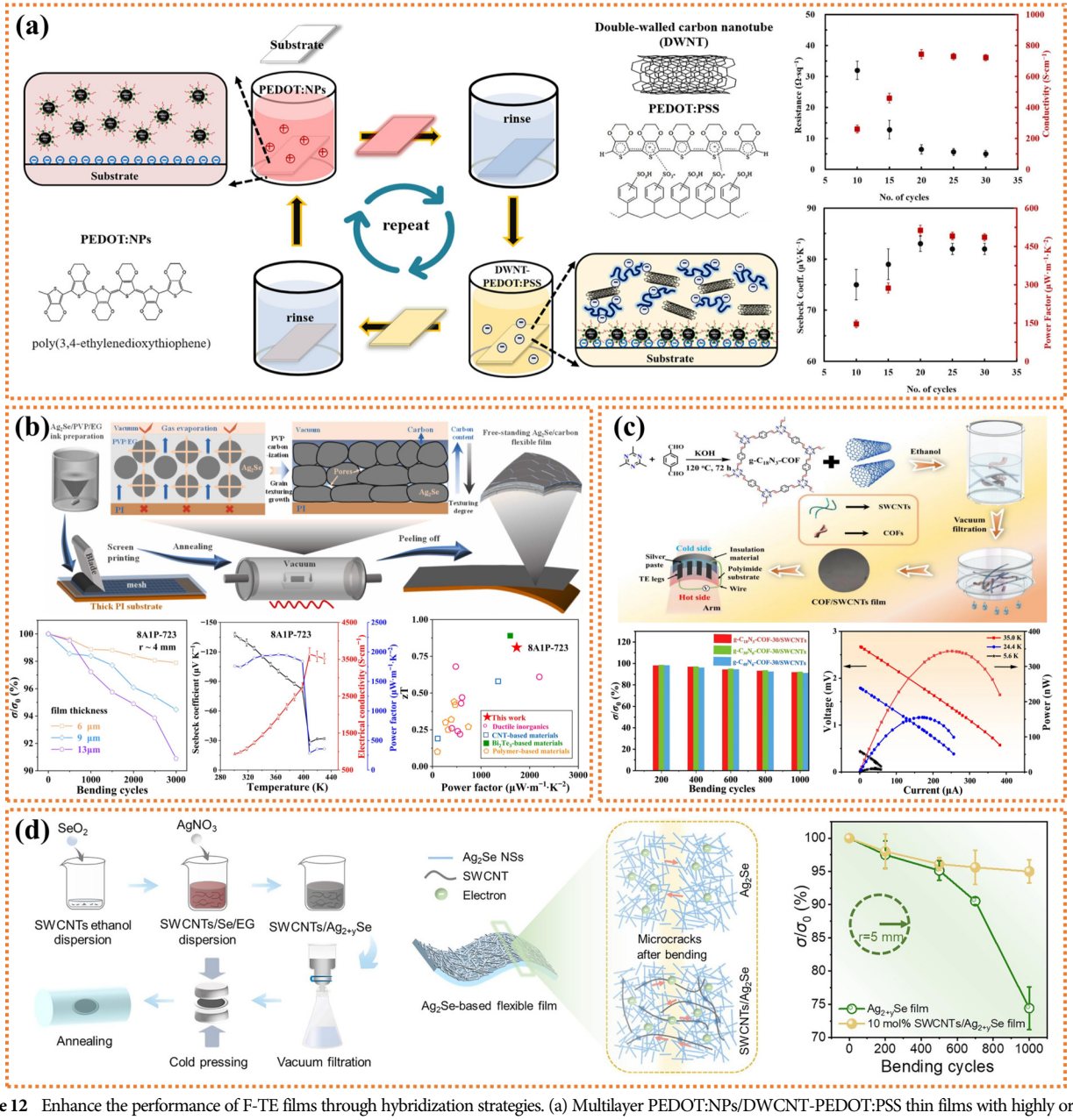

Figure 12 Enhance the performance of F-TE films through hybridization strategies. (a) Multilayer PEDOT:NPs/DWCNT-PEDOT:PSS thin films with highly ordered structure. Reproduced with permission from Ref. [284], © Elsevier B.V., 2023. (b) Free-standing Ag_2Se/carbon composite TE films. Reproduced with permission from Ref. [240], © Elsevier Ltd. 2025. (c) Flexible free-standing g-$C_{18}N_3$-COF/SWCNTs composite TE films. Reproduced with permission from Ref. [285], © Donghua University, Shanghai, China 2025. (d) SWCNTs/Ag_2Se films fabricated via *in situ* method. Reproduced with permission from Ref. [286], © Elsevier B.V. 2023.

surface of the composite film created a carbon content gradient distribution along the thickness direction. Accordingly, the Ag_2Se particles, constrained by both the substrate and the settled Ag_2Se layer, tended to grow with an in-plane textured orientation, while the Ag_2Se grains in the carbon-rich top layer preferred to grow freely into equiaxed crystals. Therefore, a weak texture gradient Ag_2Se grains was also established. Meanwhile, the evaporation led to the formation of numerous micropores in the film, which were beneficial for releasing stress and consuming energy during bending. As a result, the composite film exhibited excellent stability and flexibility, retaining over 90% of its σ after 3000 bending cycles with a radius of 4 mm. The removal of the underlying slurry weakened the adhesion between the film and the PI substrate, allowing the composite film to be easily peeled off after high-temperature annealing process. Regarding TE performance, the composite film exhibited a high *PF* of 1761 $\mu W \cdot m^{-1} \cdot K^{-2}$ and a *ZT* value of 0.81 at room temperature, because of the well-crystallized grains and the low κ caused by strong phonon scattering. A F-TED constructed by connecting such four film legs achieved a ω_{max} of 22.9 $W \cdot m^{-2}$ under ΔT = 31.4 K [240]. Beyond polymers, low-dimensional carbon materials are also used as flexible supports. In recent years, covalent organic frameworks (COFs), as a class of crystalline porous polymeric materials, have been explored for developing novel TE materials due to their π-extended skeletons, long-range ordered structures, and regular channels. As can be seen in Fig. 12(c), Wang et al. synthesized vinylene-linked COFs with a triazine core via Knoevenagel condensation [285]. They further modulated the lengths and diameters of the nano-/micro-fibers by changing the polyphenylene building blocks to ensure compatibility with subsequently used SWCNTs for obtaining high-quality thin films. Finally, flexible self-supported COF/SWCNTs composite films were prepared via simple vacuum-assisted filtration. The results showed that the film containing 30 wt.% g-$C_{18}N_3$-COF achieved the highest *PF* of 68.93 $\mu W \cdot m^{-1} \cdot K^{-2}$ at 420 K. And a F-TED was assembled by connecting four such legs in series with silver electrodes, releasing a ω_{max} of 0.32 $W \cdot m^{-2}$ at ΔT = 35 K. Furthermore, the device demonstrated outstanding stability, with a resistance change rate of less than 5% after 1000 bending cycles with a radius of 15 mm. To mitigate the additional contact resistance introduced by insufficient contact between the TE fillers and the support materials in the *ex-situ* methods, *in-situ* synthesis of the inorganic TE materials on the support surface is a common modification strategy [42, 287]. For example, Hu et al. grew Ag_2Se *in-situ* on the surface of SWCNTs, which was shown in Fig. 12(d) [286]. Subsequently, a SWCNTs/$Ag_{2+\gamma}Se$ film was successfully prepared on a nylon membrane via vacuum filtration. After drying, cold-pressing, and annealing, the film with 10 mol% SWCNTs exhibited a *PF* of 19.36 $\mu W \cdot cm^{-1} \cdot K^{-2}$ at 300 K, attributed to the increased *n* and enlarged effective mass caused by additional interstitial Ag introduced during the in-situ growth of Ag_2Se. This film still retained 95% of its initial σ after 1000 bending cycles with a radius of 5 mm. A F-TEG assembled from this material achieved a P_{out} of 0.72 μW. Table 1 summarizes the flexibility and output properties of advanced film-based TEDs in recent years.

6 Fiber-based F-TEDs

F-TEDs fabricated as thin films or on flexible substrates enable unidirectional bending to some extent and can conform to regular curved surfaces. However, in wearable applications, their dense structure results in inadequate breathability. And more importantly, it's difficult to achieve omnidirectional bending, thus the poor comfort limits their practical application in wearable scenarios requiring long-term wear. In contrast, fiber materials offer unique advantages, including light weight, breathability, stitchability and stretchability, allowing them to adapt readily to various mechanical deformations encountered in daily human activities. Therefore, fiber-based devices are widely utilized in the wearable field [288]. Some conductive polymers can be easily fabricated into TE fibers using wet-spinning, electrospinning and dip-coating methods.

6.1 Single TE fibers or yarns

6.1.1 Individual n-type or p-type TE fibers/yarns

Earlier studies focused on enhancing the performance of TE fibers and exploring the corresponding mechanisms. Individual n-type or p-type TE fibers were connected in series via wires to measure their output performance. Furthermore, owing to their distinct one-dimensional characteristics, these fibers can be woven into existing textiles or mesh support structures to more effectively establish a temperature gradient. For instance, as shown in Fig. 13(a), Komatsu et al. reported the TE performances of macroscopically weavable CNT fibers [289]. The Fermi level was tuned near the 1D van Hove singularity (VHS) through chemical treatment to obtain a higher *S*. Simultaneously, since the prepared CNTs fibers have high orientation, high density, high CNT aspect ratio and low impurity content, they exhibited ultra-high σ exceeding 10 $MS \cdot m^{-1}$, and a high *PF* of 14±5 $mW \cdot m^{-1} \cdot K^{-2}$ was obtained. A power generation unit was constructed by stitching 15 CNT fibers together with stainless steel threads into a cotton fabric and using Ag paste at the junctions to ensure reliable electrical connections. Connecting four such units in series within a circuit successfully powered an LED. As can be seen in Fig. 13(b), Wang et al. attempted to apply metal framework polymers to the TE field [80]. This is a novel class of polymers featuring a unique backbone structure formed by metal atoms bonding with each other through a metallic bond. This distinctive skeleton provides unique quantum confinement effects for charge transport, enabling the regulation of carrier transport properties. Meanwhile, various functional designs can be achieved by changing the metal atom types and ligand structure. They employed a shear-induced orientation strategy to align the nickel-based polymer (NBP) onto oriented CNTs, successfully preparing a novel NBP/CNT fiber. The introduction of NBP not only reduced defect density but also induced the dedoping effect, thereby achieving simultaneous improvements in σ and *S*. This led to a *PF* of 719.48 $\mu W \cdot m^{-1} \cdot K^{-2}$, which is 3.5 times that of pure CNT fibers. A power generation device was fabricated by connecting 9 NBP/CNT fibers in series using nylon thread coated by Ag and applying Ag paste at the interface to achieve ohmic contact. When woven into a cuff, this device generated an V_{OC} of 3.09 mV at a temperature difference of 8 K [80]. In order to address the shortcoming of n-type TE materials, Li et al. introduced the n-type TE material Ag_2Te into the PEDOT:PSS fiber matrix (Fig. 13(c)) [290]. High-performance n-type TE fibers required a sufficient content of Ag_2Te within the fiber. However, the poor compatibility between inorganic fillers and the organic matrix often limited the realization of high filler loading. They coated PEDOT:PSS on the surface of Ag_2Te nanowires (PC-Ag_2Te) through a liquid-phase reaction, thereby improving their dispersion within the matrix. Subsequently, the PEDOT:PSS/PC-Ag_2Te composite fibers with a high loading of 87.5 wt.% were prepared by wet-spinning technique. The

Table 1 The comparison of flexibility and output properties of advanced film-based TEDs in recent years

Materials	Bending radium (mm)/cycles	Normalized resistance change	*PF* (μW·cm^{-1}·K^{-2})	*ZT*	V_{OC} (mV)	P_{max} (μW)	ω_{max} (μW·m^{-2})	ω_n	Ref.
Ag_2Se	5/2000	8%	~36 (300 K)	1.15	~236.5 (100 pairs, ΔT=15 K)	—	~25.6	~9.09 μW·m^{-1}·K^{-2}	[3]
Ag_2Se	5/1000	<10%	30.8 (343 K)	0.9	27.1 (9 legs, ΔT=20 K)	0.58	8.07×10^6	1.82 μW·cm^{-2}·K^{-2}	[75]
Ag_2Se/Te	5/1000	<10%	25.7 (303 K)	1.06	77.6 (100 pairs, ΔT=20 K)	26.2	1.9×10^7	4.8 μW·cm^{-2}·K^{-2}	[36]
Ag_2Se/rGO	5/1500	<4%	37 (300 K)	~1.28	~408 (100 pairs, ΔT=26 K)	~100	6.7×10^7	9.8 μW·cm^{-2}·K^{-2}	[44]
$Ag_2(S,Se)$-Ag_2Se	5/500	<10%	~18 (298 K)	0.91 (323 K)	~36 (5 legs, ΔT=50 K)	~40	2.65×10^7	3000 μW·m^{-1}·K^{-2}	[25]
Cu_2Se	5/1000	<10%	10.75 (303 K)	~0.45	~24 (10 legs, ΔT=20 K)	~0.11	~5.7×10^6	—	[86]
Bi_2Te_3	4/1000	<10%	42 (p, 300 K) 46 (n, 300 K)	—	110.6 (5 pairs, ΔT=60 K)	260.5	3.21×10^8	1200 μW·m^{-1}·K^{-2}	[12]
Mg_3Bi_2	5/500	<10%	1.59 (333 K)	0.19	0.9 (2 legs, ΔT=2.5 K)	1.7×10^{-4}	1.67×10^4	—	[20]
Mg_3Bi_2	15/2000	<7%	35 (300 K)	~0.4	11.6 (6 pairs, ΔT=7.3 K)	1132.11	—	—	[181]
$(AgCu)_{0.998}Se_{0.22}S_{0.08}Te_{0.7}$	15/500	<5%	5.1 (300 K)	0.45	3.7 (6 pairs, ΔT=1.5 K)	203	—	30 μW·cm^{-2}·K^{-2}	[31]
$(AgCu)_{0.998}Te_{0.8}Se_{0.1}S_{0.1}$	—	—	8.37 (300 K)	~0.62	53.5 (6 pairs, ΔT=25 K)	15.12	1.26×10^6	—	[64]
SnSe	6/1000	14%	24(300 K)	—	40.1(2 pairs, ΔT=60 K)	111.2	2.57×10^8	—	[41]
SnSe	12/200	<20%	2.39(RT)	—	20.15(1 leg, ΔT=70 K)	~18	8.6×10^5		[16]
Ag_2Te	6/1000	8.8%	4.94(400 K)	0.19 (300 K)	8.1(4 legs, ΔT=32.5 K)	0.101(ΔT=30 K)		0.9 μW·cm^{-1}·K^{-2}	[32]
Ag_2Se	3/3000	<10%	10.97(377 K)	—	~30(125 legs, ΔT=40 K)	~0.8	—	2.0 μW·cm^{-1}·K^{-2}	[39]
PDPPSe-12	—	—	2.65(363 K)	0.52	13(16 legs, ΔT=28.7 K)	0.067	—	—	[43]
PDPPSe-12/PBTTT	—	—	6.28(368 K)	1.28	3.3(9 legs, wrist)	0.552(9 legs, ΔT=38 K)	—	1.12 μW·cm^{-1}·K^{-2}	[47]
CNTs	3/1000	10%	105(298 K)	—	1400(6 legs, ΔT=220 K)	175	—	—	[222]
Ag_2Se/Se/PPy	—	—	22.40(300 K)	0.94	21.20(6 legs, ΔT=34.1 K)	4.04	~3.76×10^7	6.47 μW·cm^{-1}·K^{-2}	[70]
Ag_2Se/C	4/3000	<10%	17.61(RT)	0.81	9.0(4 legs, ΔT=31.4 K)	5.5	2.29×10^7	4.65 μW·cm^{-1}·K^{-2}	[240]
PEDOT:PSS/SWCNT	45%/1000	<5%	~5.01	~0.012	7.3(6 legs, ΔT=58 K)	4.416	—	—	[206]

composite fibers successfully transformed into n-type conduction characteristics with increasing Ag_2Te content. The prepared composite fibers achieved a *S* of −61.3 μV·K^{-1} and a *PF* of 65.3 μW·m^{-1}·K^{-2}. Meanwhile, the elongation at break and tensile strength of this composite fiber were 47.37% and 6.59 MPa respectively, indicating excellent mechanical strength [290].

Compared with carbon-based or polymer-based TE materials, inorganic semiconductor materials have greater practical application potential due to their higher σ and larger *S*, which collectively result in higher *ZT* values. This makes them more suitable for meeting the increasing power demands of wearable devices [28]. In recent years, the thermal drawing technology has emerged as an efficient and cost-effective solution for processing high-performance inorganic TE materials into fibers that simultaneously possess high conversion efficiency and excellent flexibility. This process involves fixing one end of the preformed rod in the heating furnace, and then thermally drawing the fiber after the material is heated above its softening temperature. To obtain ultra-long and continuous fibers, it is necessary for the core and cladding materials of the fiber preform to match in terms of viscosity, melting point, thermal expansion coefficient, and thermal drawing temperature. As depicted in Fig. 13(d), Zhang et al. utilized this thermal stretching process to stretch a rod preform consisting of a SnSe core and a borosilicate glass cladding, obtaining ultra-long polycrystalline SnSe wires with high flexibility and mechanical stability [138]. Then, a post-treatment process of laser-induced directional recrystallization was employed to produce single-crystal SnSe TE fibers. During the initial thermal drawing, the rapid cooling rate and low fiber tension at high temperatures were conducive to the formation of the amorphous phase, resulting in poor TE properties. While, after a tiny region of the polycrystalline SnSe was irradiated by laser, it was heated to a

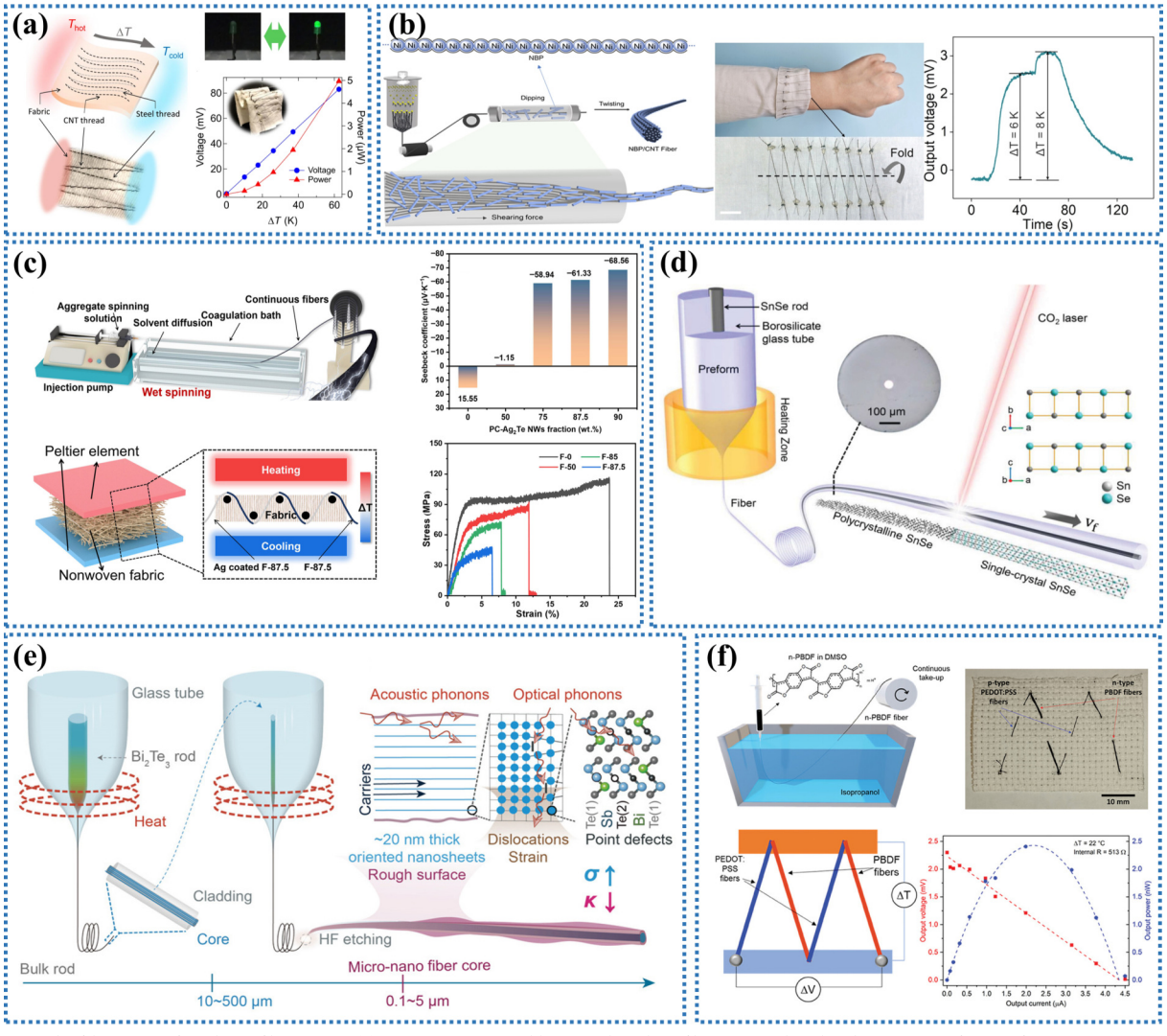

Figure 13 The fabrication of single TE fibers/yarns. (a) Macroscopic weavable CNTs-based TE fibers. Reproduced with permission from Ref. [289], © Komatsu, N. et al. 2021. (b) Flexible TE fibers from metal-backboned polymers. Reproduced with permission from Ref. [80], © Wiley-VCH GmbH 2024. (c) Flexible n-type PEDOT:PSS/PC-Ag_2Te NWs composite TE fibers. Reproduced with permission from Ref. [290], © American Chemical Society 2025. (d) Single crystalline SnSe fibers obtained through thermal drawing method and post-draw laser recrystallization process. Reproduced with permission from Ref. [138], © WILEY-VCH Verlag GmbH & Co. KGaA, Weinheim 2020. (e) Micro-nano TE fibers prepared by the glass-fiber-template thermal drawing method. Reproduced with permission from Ref. [291], © Wiley-VCH GmbH 2022. (f) n-type PBDF fibers obtained by wet-spinning method. Reproduced with permission from Ref. [292], © Wiley-VCH GmbH 2023.

molten state and then cooled again to crystallize, gaining single crystal. As a result, the single crystal SnSe fibers obtained an extremely high *ZT* value of 2 at 862 K, far surpassing that of the polycrystalline fiber [138]. In another study, Sun et al. employed a two-step thermal drawing process to fabricate micro/nano polycrystalline TE fibers by stretching bulk Bi_2Te_3-based material within a glass-fiber template (Fig. 13(e)) [291]. During the drawing process, stress-induced oriented nanocrystal and the creation of strain-distorted interfaces simultaneously enhanced σ and reduced κ. As a result, TE fibers with a diameter of 4 μm exhibited a remarkably high *ZT* value of 1.4 at 300 K, which was 40% higher than that of the corresponding bulk material. Moreover, these fibers demonstrated outstanding mechanical flexibility, with a resistance increase of less than 10% after 100 bending cycles with a radius 50 μm. The achieved bending strain of 4% approached the theoretical elastic limit of Bi_2Te_3 (~5.5%). As research progresses, this thermal drawing technique was extended to other material systems, such as $Ag_2Te_{0.6}S_{0.4}$ [293, 294]. However, it must be pointed out that fabricating F-TE fibers through this method often imposes stringent requirements on material selection, design, and precise control of the processing parameters, which limits its widespread application.

In the aforementioned cases of power generation devices, the use of another material as connecting wires for the TE fibers inevitably limits the further improvement of device output performance. Therefore, from the perspective of practical application, it is an inevitable choice to construct fiber-based F-TEDs by alternately connecting performance-matched n-type and p-type TE fibers in series. For instance, Ruben *et al.* made the first attempt to directly spin pure n-type polymer fibers using an isopropanol coagulation bath wet-spinning method, obtaining n-doped poly(3,7-dihydrobenzo[1,2-b:4,5-b']difuran-2,6-dione) (n-PBDF) fibers (Fig. 13(f)) [292]. By alternately connecting two bundles of n-type PBDF fibers with two bundles of p-type PEDOT:PSS fibers, a P_{out} of 2.40 nW was generated under a temperature difference of 22 K. Yin et al. impregnated CNT yarns (CNTYs) with oleylamine (OAm) for modification, obtaining a n-type OAm/CNTY yarns after drying in air [295]. The specific TE properties of this OAm/CNTY yarns

achieved a σ of 1353.18 S·cm^{-1}, a S of –80.48 μV·K^{-1}, and a PF of 876.25 μW·m^{-1}·K^{-2}. More importantly, during the impregnation process, the OAm was coated the surface of the CNT bundles and formed a dense structure within the yarns. The excellent stability of the dopant OAm contributed to the prevention of CNTs from adsorbing oxygen in the air. As a result, after being stored in air for 370 days, S and σ retained 96.90% and 90.01% of their initial levels, respectively, demonstrating the excellent air stability of this n-type material. A wearable TE generator was constructed by serially connecting 150 pairs of p-type pristine CNTY and n-type OAm/CNTY using conductive Ag paste. This device achieved V_{OC} of 705.94 mV and P_{out} of 44.34 μW under a temperature difference of 40 K [295].

6.1.2 *N-P alternating segmented TE fibers/yarns*

However, this method of connecting individual n-type and p-type TE fibers using electrodes or wires not only makes the device fabrication process and structure complicated, but also introduces interfacial resistance at the junctions, which limits the overall device performance. More critically, such junctions are particularly susceptible to fracture during frequent bending or stretching. Therefore, researches focusing on simultaneous integration of n-type and p-type TE segments within a single fiber has received widespread attention. As shown in Fig. 14(a), Zheng et al. innovatively developed hierarchical ternary coaxial TE strings [296]. This string consisted of p-type $Bi_{0.4}Sb_{1.3}Te_3$ (BST) and n-type $Bi_2Te_{3.3}Se_{0.2}$ (BTS) segments alternately connected by liquid metal on a PI filament, all encapsulated within a PDMS elastomer. Benefiting from the toughening effect of the PI filament and the excellent elastic deformation capability of the PDMS elastomer, the overall toughness and mechanical stability of the fiber string were enhanced. Furthermore, using a weaving machine, the TE fibers were woven together with elastic yarns into a F-TE fabric. This fabric exhibited good stretchability, flexibility, washability, and outstanding TE performance, achieving a ω of 0.58 W·m^{-2} at a temperature difference of 25 K. In practical application, it can power various wearable devices and continuously generate a stable cooling of 3.1 K [296]. Figure 14(b) demonstrated that Ding et al. prepared a p-n segmented F-TE fiber composed of SWCNTs and polyvinyl alcohol (PVA) hydrogel via a continuous alternating extrusion process [297]. Thanks to the network constituted by hydrocolloid and its rheological property, as well as the confinement of heterogeneous molecular particles within the continuous matrix, the alternately extruded gels maintained a clear p-n junction structure at the interfaces. The output performances of the fibers can be conveniently adjusted by varying the number of p-n segments, and its performance can be further enhanced by weaving into a textile.

In addition to the aforementioned method of preparing single fibers or yarns with alternating n/p-type TE components in a segmented manner, periodic modification of the already prepared fibers using different post-treatment methods is also a feasible

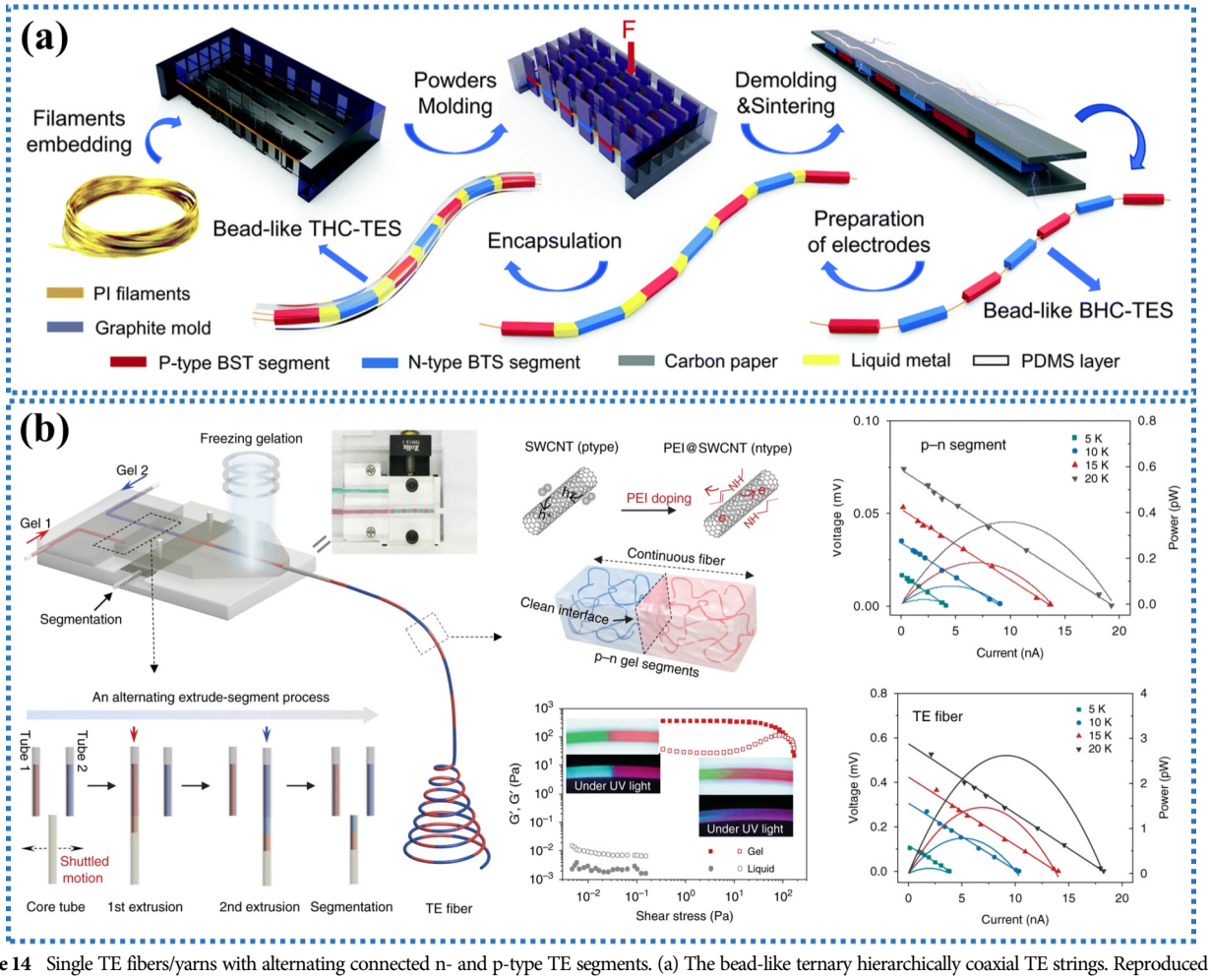

Figure 14 Single TE fibers/yarns with alternating connected n- and p-type TE segments. (a) The bead-like ternary hierarchically coaxial TE strings. Reproduced with permission from Ref. [296], © The Royal Society of Chemistry, 2022. (b) Preparation of p-n segmented flexible SWCNTs/PVA TE fiber via a continuous alternating extrusion process. Reproduced with permission from Ref. [297], © Ding, T. P. et al. 2020.

approach to achieve n/p component integration. The processes such as impregnation, spraying, and brushing have garnered significant research interest due to their simple operational and the elimination of need for custom molds or expensive specialized equipment, greatly simplifying the preparation of F-TE fibers [298]. As shown in Fig. 15(a), Sun et al. reported that CNTYs with sufficient tensile strength were obtained by twisting and coiling CNT films [299]. These yarns were subsequently immersed in a PEDOT:PSS solution for p-type doping. Then, using a polypropylene mask to periodically cover sections of the fiber, OAm was sprayed onto the exposed regions via electrostatic spraying to achieve n-type doping. There was a 2 mm undoped segment between each p/n section serving as an electrical connection. Finally, the doped CNTY was wrapped in acrylic fibers to prevent short circuits. Although the OAm caused a slight decrease in σ of the CNTY, a *PF* of 320 $\mu W \cdot m^{-1} \cdot K^{-2}$ was ultimately achieved due to the high *S* [299]. In another study, Zheng et al. wrapped CNTYs around a thin PET plate and coiled them into a stacked cylindrical structure (Fig. 15(b)) [37]. Then, two parallel Ag paste lines were coated to control the height of immersion into PEDOT:PSS aqueous solution and PEI/ethanol solution, thereby forming p-type and n-type segments, respectively. Finally, the prepared composite segmented TE yarns were twisted with PET filament to enhance their mechanical stability. To ensure high σ in CNTYs after twisting, Wu et al. obtained dense structured CNTYs through a wet-twisting method, where capillary forces between CNTs and water promoted the adhesion of adjacent CNTs [300]. The prepared CNTY was then wound around a PI plate, and segmentally modified by repeatedly brushing PEI or PEDOT:PSS solutions on either side of the plate, as illustrated in Fig. 15(c). To prevent dopant diffusion during brushing process, they increased the temperature to accelerate the evaporation of deionized water. The remaining PEI and PEDOT:PSS, with their higher boiling points and larger molecular chains, were difficult to migrate and eventually adsorbed onto the CNT surfaces, achieving n/p doping. The highly conductive Ag paste was brushed onto the cross-sectional ends to act as electrodes. By optimizing the brushing temperature and frequency, the *PF* of the CNTY was enhanced to 667 $\mu W \cdot m^{-1} \cdot K^{-2}$ [300]. Inspired by natural tendrils, Wang et al. designed a Janus helical hydrogel fiber capable of maintaining its original TE performance even under ultra-high elastic strain (Fig. 15(d)) [301]. Using a parallel dual-spinneret wet-spinning system, a plastic polyacrylic acid sodium (PANa) hydrogel microfiber composed of elastic PANa hydrogel and PEI-doped SWCNTs was prepared. Subsequent cold-drawing ingeniously utilized the strain mismatch between the two elastomers to generate a helical structure. PEI was then used to dope the SWCNTs, converting one half of the helical coil into n-type. This helical coil design enabled stable TE conversion under tensile strains as high as 650%, capable of driving an LCD screen with an amplifier and demonstrating high sensitivity ($-176\ \mu V \cdot K^{-1}$) in temperature detection. Furthermore, Kim et al. creatively developed seamlessly connected GO composite fibers by selectively subjecting a single GO fiber to varying degrees of chemical reduction [302]. The different reduction states of GO led to differences in the energy levels, resulting in different *S*. When used as a thermocouple, this GO composite fiber achieved a sensitivity of 12.5 $\mu V \cdot K^{-1}$, a linear correlation coefficient of 0.995,

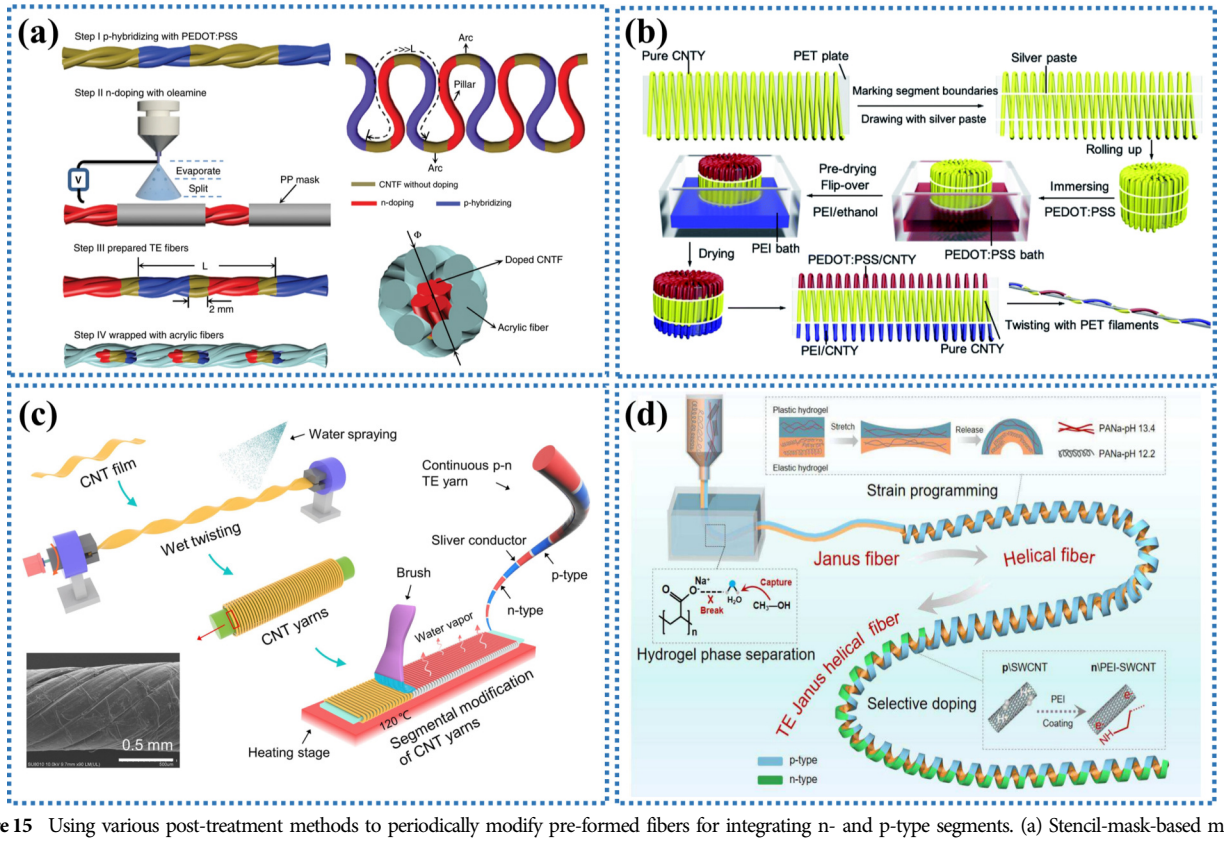

Figure 15 Using various post-treatment methods to periodically modify pre-formed fibers for integrating n- and p-type segments. (a) Stencil-mask-based method combined with electrospray technology. Reproduced with permission from Ref. [299], © Sun, T. T. et al. 2020. (b) Impregnation method. Reproduced with permission from Ref. [37], © The Royal Society of Chemistry 2020. (c) Spread coating method. Reproduced with permission from Ref. [300], © Elsevier B.V. 2023. (d) Janus helical PANa-SWCNT fibers fabricated by utilizing the biological strain mismatch mechanism. Reproduced with permission from Ref. [301], © American Chemical Society 2025.

and a response time of 0.24 s. Moreover, the thermocouple's sensitivity could be tuned by adjusting the reduction degrees. Although this work did not achieve n-type conversion, it provides a feasible concept for the development of segmented TE fibers.

6.2 TE textiles

6.2.1 *Integrate inorganic TE materials onto flexible textiles*

Utilizing textiles as flexible substrates for traditional rigid inorganic TE pillars is a common strategy for creating F-TEDs [303]. When constructing such devices containing rigid components, it is essential to carefully consider the reliable connections among the rigid parts, electrodes and substrate. Especially when deformation occurs, it is even more crucial to ensure that all parts maintain close contact. To address these challenges, Hou et al. proposed a F-TEG composed of p-type $Bi_{0.5}Sb_{1.5}Te_3$ and n-type $Bi_2Te_{2.7}Se_{0.3}$ rigid TE pillars, elastic fabric substrates, and conductive fabric electrodes, as shown in Fig. 16(a) [304]. A semi-automated assembly process was developed to ensure the alignment during the transfer of the electrode array. Thanks to the patterned elastic fabric substrate conforming well to the rigid TE pillars and the stretchability of the serpentine fabric electrodes, the F-TEG exhibited excellent flexibility, allowing it to fit well to any shape of heat sources and withstand 30% strain. This device generated a P_{max} of 64.10 μW and a V_{OC} of 111.49 mV under a temperature difference of 33.24 K. Beyond TE conversion, this device can also serve as electronic skin mounted on robots for health and motion monitoring [304]. However, significant energy was wasted due to the large internal resistance of the device. Therefore, reducing device internal resistance by optimizing the interface connection and improving the conductivity of the electrodes is a key point that needs to be carefully considered in the device design. Apart from serving as flexible substrates for rigid inorganic TE materials, modifying the textiles through processes like solution coating, spraying, or sputtering can also get functional fabrics with TE properties. For instance, Arimatsu et al. reported a breakthrough in the *S* by coating a felt fiber substrate with a solution of PEDOT doped with the low-molecular-weight p-toluenesulfonic acid (PTSA) [305]. This PEDOT:PTSA/felt composite exhibited extraordinary TE performance. Its *S* widely tunable from -2100 $\mu V \cdot K^{-1}$ (n-type) to 3100 $\mu V \cdot K^{-1}$ (p-type), which was two orders of magnitude higher than that of conventional PEDOT materials. And the corresponding *PFs* reached up to 2400 $\mu W \cdot m^{-1} \cdot K^{-2}$ (p-type) and 1100 $\mu W \cdot m^{-1} \cdot K^{-2}$ (n-type). This research indicated that this giant *S* is closely related to the tensile strain of the C_β-C_β bonds in the PEDOT molecules, rather than changes in carrier concentration, suggesting that switching between p-type and n-type conduction can be achieved simply by adjusting the PTSA concentration within the PEDOT system [305]. As illustrated in Fig. 16(b), Newby et al. developed a fully graphene-based F-TEG using screen-printing technology [306]. They used amine-functionalized n-type graphene and metal-doped p-type graphene inks, with DMSO as the solvent and polyurethane (PU) as the binder and protective agent, to directly print multiple p-n junction TE modules onto cotton fabric without requiring post-treatment or high-temperature annealing. This device generated a V_{OC} of 5.24 mV under a 40 K temperature difference and a P_{out} of 62.4 μW (ΔT=16.5 K). Despite the convenience of these surface modification techniques for imparting TE function, their application faces significant limitations. For instance, the functional coatings formed by these methods are mostly physically attached to the fabric fibers, with weak interfacial bonding strength. Furthermore, the inherent breathability, moisture permeability, and softness of the textile may be seriously sacrificed because the fabric pores can be blocked by coatings, which adversely impacts wearing comfort.

6.2.2 *Weave TE fibers/yarns into fabrics*

Wearable TEDs generally utilize human skin as the hot side and the external environment as the cold side. The human body serves as a continuous heat source with a temperature of approximately 37 °C. In contrast, the environmental temperature can fluctuate

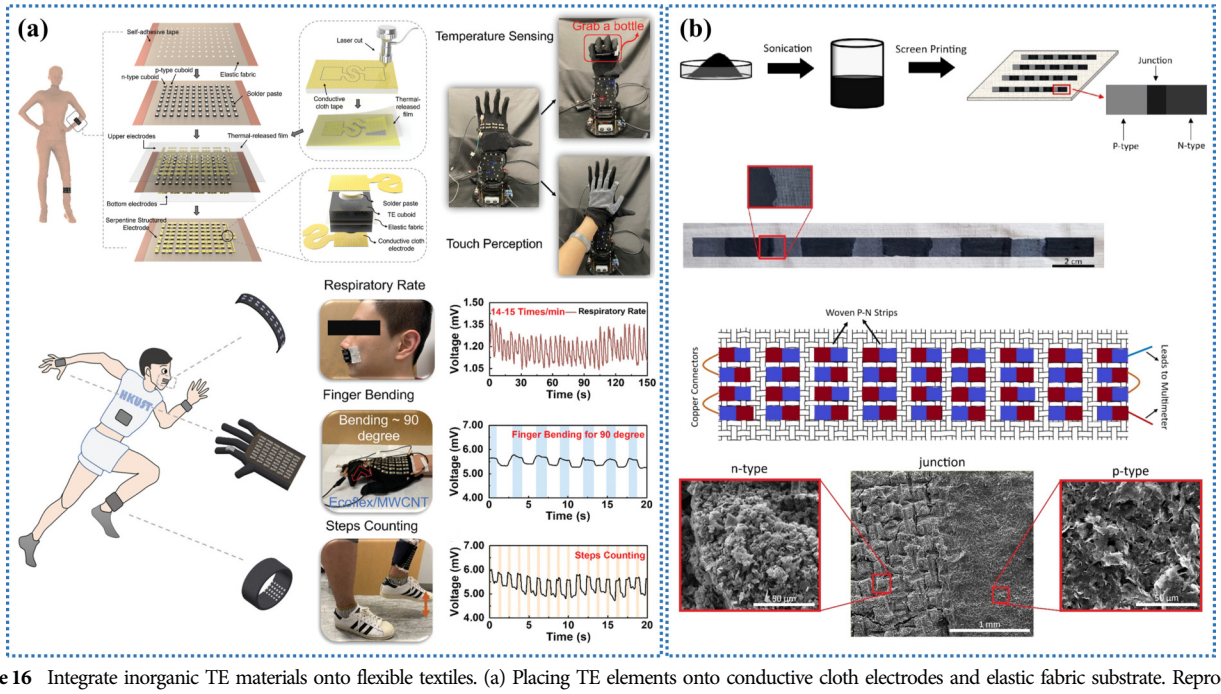

Figure 16 Integrate inorganic TE materials onto flexible textiles. (a) Placing TE elements onto conductive cloth electrodes and elastic fabric substrate. Reproduced with permission from Ref. [304], © Hou, Y. et al. Advanced Science published by Wiley-VCH GmbH 2021. (b) Printing p- and n-type graphene inks onto woven cotton substrates. Reproduced with permission from Ref. [306], © Newby, S. et al. Published by American Chemical Society 2025.

greatly ranging from –40 to 40 °C depending on the geographic area and season. Thus, a larger temperature gradient can be established in the thickness direction. Although, some studies have proposed origami schemes that convert planar devices into the thickness direction and achieved higher TE performance, this method usually compromises devices' stretchability. Due to the stitchability of fiber materials, TE fibers or yarns can be woven directly into fabrics using advanced weaving technologies. This strategy allows for the creation of larger temperature gradients along the thickness direction and the high-density integration through reasonable weaving structure design. For instance, Lee et al. fabricated strips with a sheath-core structure by alternately depositing n-type Bi_2Te_3 and p-type Sb_2Te_3 onto highly aligned polyacrylonitrile (PAN) nanofiber sheets (Fig. 17(a)) [48]. These strips were interconnected by sputtered gold strips. The nanofiber membrane was then twisted into F-TE yarns and woven into fabrics by zigzag, garter, and plain knitting. Due to the shorter TE leg length in the plain-weave fabric leading to lower resistance, it achieved a power per area of 0.62 $W{\cdot}m^{-2}$ under a 55 K temperature difference. As shown in Fig. 17(b), Sun et al. fabricated n/p alternating doped CNTYs and bent them into "TE rings". which were then directly woven into a fabric using a unique alternating interlocking weaving structure [299]. This weaving method utilized the inherent elasticity of the fibers to enable the rings to stand up automatically within the fabric, forming a self-supporting 3D structure distinguished from other textile-based devices. This design efficiently took advantage of the vertical temperature difference between the human body and the environment for power generation. This TE textile demonstrated outstanding performance with a ω of 70 $mW{\cdot}m^{-2}$ at a 44 K temperature difference and excellent stretchability over 80% in the longitudinal direction with minimal performance degradation (<3.2%). It could be attached to human joints, generating power stably during movement [299]. Recently, He et al. reported a 3D F-TE fabric characterized by rigid interior and flexible exterior (Fig. 17(c)) [307]. This 3D spacer fabric was produced using a double-needle bar warp knitting machine, interweaving polyester filaments of different stiffnesses. One side was formed by warp knitting and satin weave, creating a hexagonal mesh was achieved through a solution impregnation method. After the fabric was immersed in a CNT aqueous dispersion to get a conductive substrate, p-type fabrics were prepared by dipping into PEDOT:PSS solution and post-treatment with DMSO, while n-type fabrics were prepared by impregnating with an OAM/ethanol solution. The novel weaving method created numerous small static air pockets within the fabric, endowing it with ultra-low κ (<0.05 $W{\cdot}m^{-1}{\cdot}K^{-1}$), high breathability (1300 $mm{\cdot}s^{-1}$), and excellent elasticity (>10,000 compression cycles). These properties worked for a stable temperature gradient across the fabric thickness, which enables an ultra-fast response of 240 ms and high-precision temperature detection of 0.02 K. Furthermore, the TE and piezoresistive signals can be completely decoupled. This allowed the output voltage to remain stable even under compressive strains up to 50%. The research demonstrated the practical potential of this fabric by integrating it into a smart mask and glove for real-time respiration monitoring, high-temperature warning, and gesture language recognition based on machine learning [307].

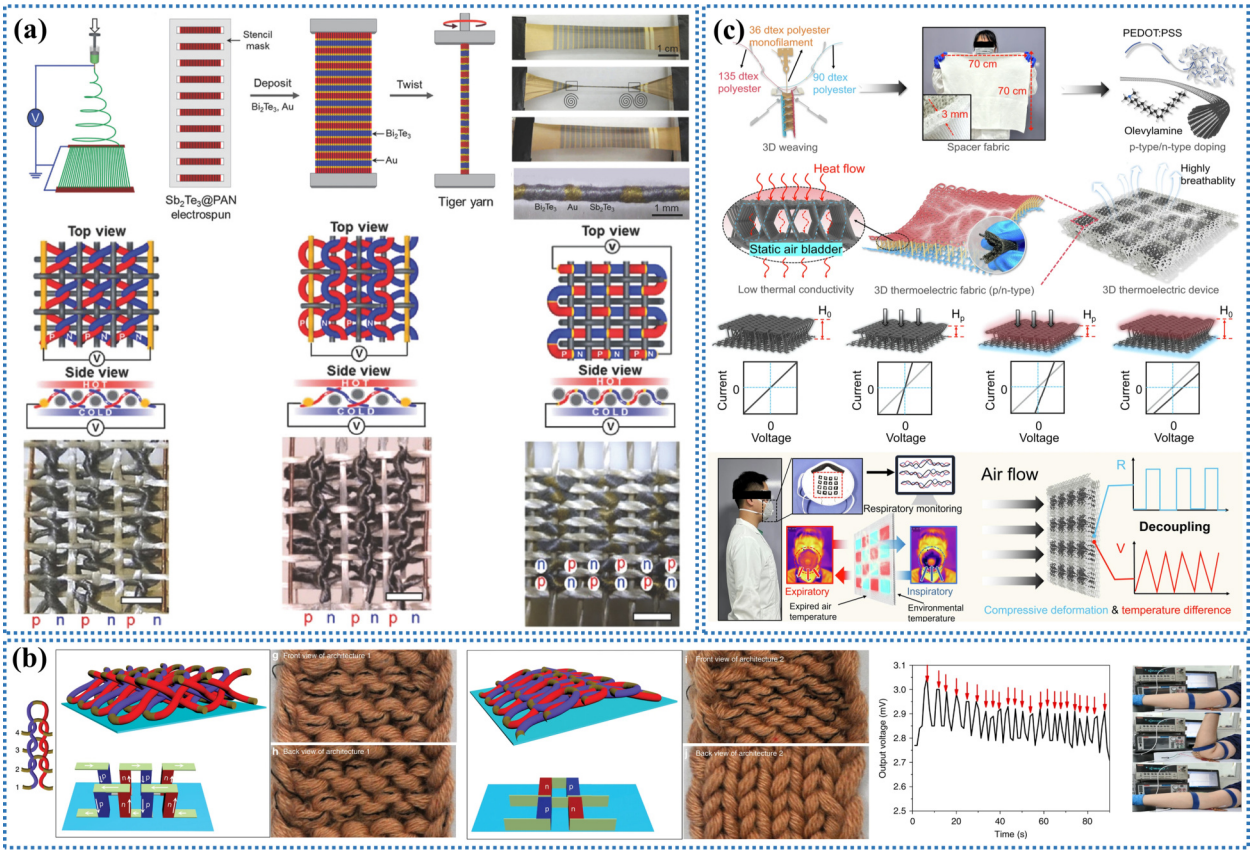

Figure 17 Prepare F-TEDs by weaving fibers/yarns using various weaving methods. (a) Realizing zigzag-stitch, garter-stitch, and plain-weave TE textiles by weaving tiger yarns. Reproduced with permission from Ref. [48], © WILEY-VCH Verlag GmbH & Co. KGaA, Weinheim 2016. (b) Configuring TE textiles by alternately interlocking TE loops and conventional fabrics. Reproduced with permission from Ref. [299], © Sun, T. T. et al. 2020. (c) Preparing spacer TE fabric for smart wearables. Reproduced with permission from Ref. [307], © He, X. Y. et al. 2025.

6.2.3 *Weave TE fibers/yarns into support structures*

To better utilize the temperature difference across the fabric thickness and achieve higher output power, another straightforward method is weaving the prepared TE fibers or yarns into thick textile substrates or 3D support structures [290]. For instance, Wen et al. enhanced the dispersion of SWCNTs in the PEDOT:PSS aqueous solution by *in-situ* polymerizing PANI on the SWCNT surfaces as an intermediate layer, as can be seen in Fig. 18(a) [191]. The introduction of numerous interfaces provided a more effective energy filtering effect for charge carriers. Furthermore, each individual composite fiber was periodically coated with Ag paste to obtain 8 pairs of serially connected p-type TE legs. Weaving these composite fibers into a commercial bracelet via plain weaving yielded a voltage of 23.2 mV and a remarkably high ω of 27.2 mW·cm^{-2} under a temperature difference of 11.4 K between the human body and the environment. Figure 18(b) displayed an ultra-elastic porous silicone substrate fabricated via 3D printing, and the prepared p/n alternately doped CNTYs were inserted into this substrate in a wavy geometry to align with the heat flow direction [300]. Finally, the device was encapsulated with silicone, granting it excellent waterproofness and enabling stable operation during activities like

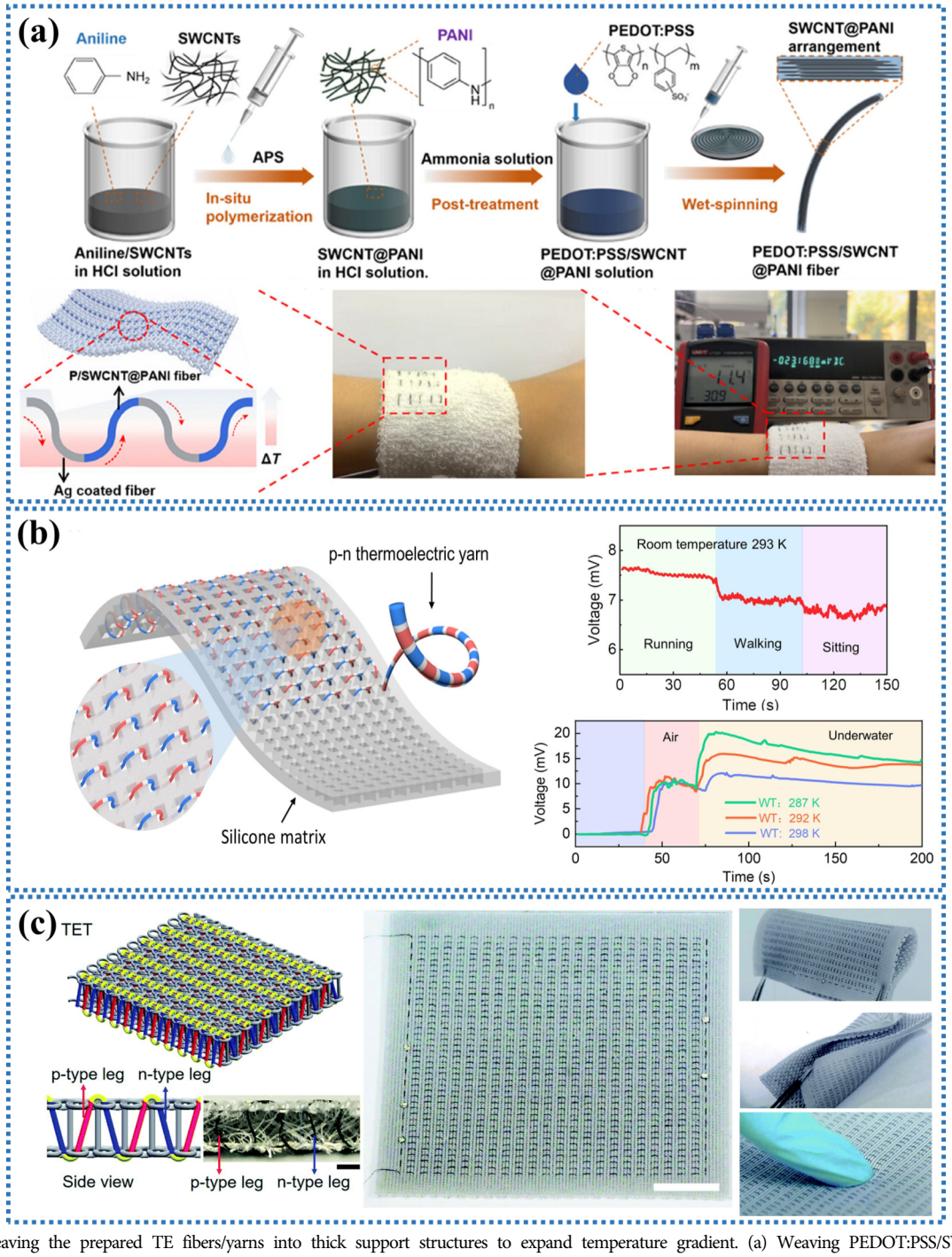

Figure 18 Weaving the prepared TE fibers/yarns into thick support structures to expand temperature gradient. (a) Weaving PEDOT:PSS/SWCNT@PANI composites TE fibers into a commercial bracelet. Reproduced with permission from Ref. [191], © Wiley-VCH GmbH 2025. (b) Encapsulating n-p CNTYs into silicone matrix. Reproduced with permission from Ref. [300], © Elsevier B.V. 2023. (c) Weaving n-p CNTYs into 3D spacer fabrics. Reproduced with permission from Ref. [37], © The Royal Society of Chemistry 2020.

running and swimming. Similarly, some reported works described the use of 3D spacer fabrics as flexible substrates for TE fibers. This scheme often requires other insulating fibers or yarns to serve as spacer yarns, separating the cold and hot ends and providing support points for the TE fibers/yarns [298, 308]. As shown in Fig. 18(c), Zheng et al. wove their prepared p/n segmented CNTYs into a warp-knitted spacer fabric substrate [37]. This device achieved a lateral areal density of approximately 7.7 mm^2 per pair and a ω of 51.5 $mW{\cdot}m^{-2}$ under a temperature difference of 47.5 K. It should be noted that the F-TEDs designed by this method require that the height of the support material should match the segmented length of the TE fibers/yarns, in order to ensure junctions are precisely distributed at the cold and hot ends. This imposes very high requirements on the manufacturing precision. Meanwhile, since the response of the support materials and the TE fibers/yarns to deformations like stretching or compression is different, it is difficult to ensure the perfect contact between junctions and target surfaces, thereby affecting the overall performance of the device [309, 310]. Table 2 summarizes the mechanical and output properties of advanced fiber-based TEDs in recent years.

7 Applications

7.1 F-TEGs

Collecting thermal energy from irregular heat source and human skin surfaces to generated electricity is one of the potential applications of F-TEDs based on the Seebeck effect. Especially in the field of wearable electronics, F-TEGs can be closely adhered to the skin surface to achieve efficient thermal contact, thereby making the best of small ambient temperature gradients for power generation [73, 246, 311, 312]. It is expected to reduce reliance on chemical batteries or decrease the charging frequency, providing an ideal micro-energy solution for self-powered wearable electronic devices. As illustrated in the Fig. 19(a), Zhang et al. successfully developed a high-performance F-TE film [44], consisting of Ag_2Se nanowires as the primary TE component, reduced graphene oxide (rGO) as the conductive network, and a nylon membrane as the flexible substrate. The hot-pressing process induced a strong (013) crystallographic orientation in the Ag_2Se nanowires, significantly enhancing carrier mobility and electrical conductivity. The incorporation of rGO further decoupled S and σ through an energy filtering effect, while its high-intensity interfaces between rGO and Ag_2Se effectively scattered phonons, decreasing κ below 0.9 $W{\cdot}m^{-1}{\cdot}K^{-1}$. Consequently, the film achieved a record-high PF of 37 $\mu W{\cdot}cm^{-1}{\cdot}K^{-2}$ and a ZT value of 1.28 at 300 K. Furthermore, the nylon membrane ensured excellent flexibility and stability, maintaining 96.9% of its original σ after 1500 bent cycles at a 5 mm bending radius. During the device fabrication, silicone hemispheres were introduced to support TE legs, which simultaneously increased the contact area with the heat source and created an effective out-of-plane temperature gradient. More importantly, the appropriate compressibility and hardness of hemispheres weakened the deformation applied to the TE legs, effectively avoiding the damage or fracture due to its limited flexibility, thereby enhancing device reliability. A fabricated F-TEG, comprising 100 TE couples, achieved a maximum P_{out} of 100 μW and an ultra-high ω_n of 9.8 $\mu W{\cdot}cm^{-2}{\cdot}K^{-2}$, at ΔT = 26 K. In a practical application scenario, this F-TEG could generate a V_{OC} of approximately 120 mV by exploiting an out-of-plane ΔT of about 8 K between the human body and ambient environment, successfully powering a thermohygrometer (1.5 V) and a wristwatch (3 V) [44]. It should be noted that this energy supply was achieved through parallel capacitors and a boost circuit, rather than directly provided real-time power supply to the device. Therefore, it has become a research hotspot that how to achieve an integrated and flexible design among power generation module, energy storage and conversion system. Smart wristband is a kind of popular wearable device and plays an important role in human health monitoring. Figure 19(b) showed a self-powered multi-functional health monitoring wristband, integrating with F-TEG, an energy management system (EMS), and a health monitoring system (HMS) [49]. By a synergistic strategy of supersaturated nanostructure and anti-site defects for $Bi_{0.5}Sb_{1.5}Te_3$-based TE material, its room-temperature ZT was increased to 1.2. When worn this bracelet on the wrist, a remarkably high ω of 153.3 $\mu W{\cdot}cm^{-2}$ was achieved during walking in 5.6 °C ambient temperature, ranking among the highest values reported for F-TEGs. In terms of EMS circuit design, the cold start process of commercial converter ADP5091 was bypassed by using the LTC3108 chip, reducing its minimum operating voltage from 380 to 80 mV, simultaneity. To further enhance the conversion efficiency, a low-quiescent-current inverting voltage-off scheme and an anti-reflux circuit were applied. Consequently, the efficiency of the converter increased from 26% to 47.7%. Whereafter, the HMS implemented numerous strategies to reduce the average power consumption for long-term operation, such as dynamic sampling, first-in-first-out (FIFO) buffering and Bluetooth intermittent connection, successfully achieving continuous monitoring and wireless transmission of multimodal signals including temperature, humidity, heart rate, step count and blood oxygen [49].

Table 2 The comparison of the mechanical and output properties of advanced fiber-based TEDs in recent years

Materials	Elongating at a break	Tensile stress (MPa)	PF ($\mu W{\cdot}m^{-1}{\cdot}K^{-2}$)	V_{OC} (mV)	P_{max} (nW)	Ref.
PEDOT:PSS/Te	13%	205	233.5	12.1 (30 legs, ΔT=15 K)	5.3	[67]
PEDOT:PSS/Ag_2Te	47.37%	6.59	65.3	—	—	[290]
Ni-backboned polymer/CNTs	—	—	719.48	3.09 (9 legs, ΔT=8 K)	—	[80]
PEDOT:PSS	11%	458.2	~55.4	0.49 (2 legs, ΔT=25 K)	—	[211]
poly(3,7-dihydrobenzo[1,2-b:4,5-b'] difuran-2,6-dione)	16.8%	248	91	~2.3 (2 pairs, ΔT=22 K)	2.40	[292]
CNT/OAm	33.82%	278.38	876.25	705.94 (150 pairs, ΔT=40 K)	44,340	[295]
DWCNT/PU	100%	—	149.7	218 (108 pairs, ΔT=30 K)	16,900	[298]
Graphene	—	—	—	0.91 (36 pairs, ΔT=16.5 K)	62,400	[306]
Ag/Ag_2Se	—	—	850	12.5 (6 pairs, ΔT=40 K)	156	[309]

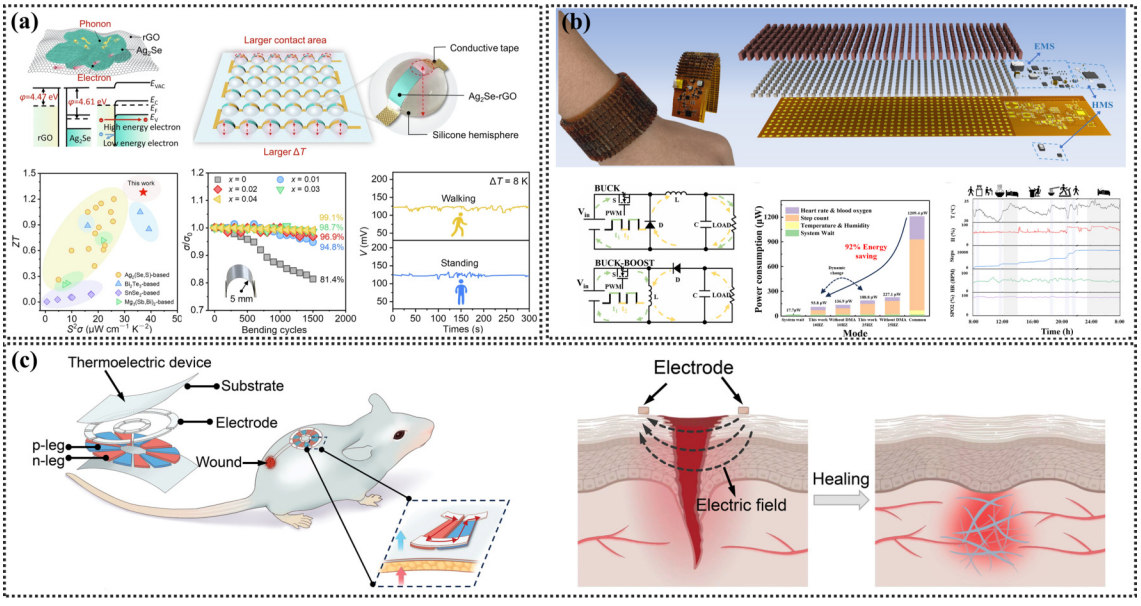

Figure 19 Applications of F-TEGs. (a) Ag_2Se-rGO composite films used for energy harvesting. Reproduced with permission from Ref. [44], © Zhang, L. et al. 2025. (b) High-power-density F-TEGs used for supplying energy for a wearable multimodal health monitoring bracelet. Reproduced with permission from Ref. [49], © Liang, L. L. et al. Published by Elsevier Inc. 2025. (c) F-TEGs used for accelerating wound healing. Reproduced with permission from Ref. [50], © Wiley-VCH GmbH 2024.

In addition to their utilization in self-powered devices, F-TEGs also play a significant role in accelerating wound healing. Electrical stimulation, as a bioelectric signal, can regulate cellular proliferation and migration processes. Therefore, enhancing the endogenous electric field (EEF) via exogenous stimulation, which was spontaneously formed near the wound, has become an effective strategy for accelerating the healing process [313, 314]. For instance, as demonstrated in Fig. 19(c), Zhang et al. alternately deposited Bi_2Te_3-based TE legs on a flexible PI substrate through magnetron sputtering, successfully developing a completely flexible circular TEG [50]. This device could generate 10 mV voltage at a temperature difference of 10 K between the skin and environment. It was significantly improved by this generated electricity that fibroblasts cells migrated and propagated, as well as vascular endothelial growth factor was activated for expression, achieving 4 days faster wound healing than natural healing process [50]. Operating without any external amplifier circuit, this device converted ubiquitous thermal energy into bioelectrical signals that promote tissue regeneration, a novel design for self-powered bioelectronics. Similarly, Qin et al. incorporated Ag_2Se nanoparticles with excellent room-temperature TE properties into a biocompatible gelatin methacrylate (GelMA) matrix, fabricating Ag_2Se @GelMA hybrid TE hydrogels through photocuring [315]. When applied as a wound dressing, this hydrogel could enhance the EEF, thereby facilitating cellular proliferation, migration and angiogenesis, achieving almost complete wound closed within 15 days.

7.2 F-TECs

Precise temperature management is another significant application of F-TEDs, which is based on the Peltier effect, the inverse of the Seebeck effect [102, 316, 317]. For example, to address the issues of high cost and complex fabrication of current inorganic F-TE materials, Chen et al. developed a simple, low-cost method involving hydrothermal synthesis, screen printing, and SPS to preparate high-performance flexible Ag_2Se films [36]. Figure 20(a) showed that the introduction of Te as a nano-binderand dopant significantly enhanced the film's densification. Furthermore, an energy filtering effect generated at the interfaces selectively scattered low-energy carriers, resulting in a concurrent incremental S and σ. It was also found that Te diffused into the Ag_2Se lattice and substituted for Se at the Te-Ag_2Se boundaries during annealing, creating lattice defects that intensified phonon scattering and reduced the κ_{lat}. Ultimately, the Ag_2Se film with 5 wt.% Te gained a high PF of 25.7 $\mu W \cdot cm^{-1} \cdot K^{-2}$ and an excellent ZT value of 1.06 at 303 K, while also demonstrating remarkable mechanical durability, with less than 5% performance degradation after 1000 bending cycles. Based on this n-type film and p-type $Bi_{0.4}Sb_{1.6}Te_3$ film also doped with 5 wt.% Te, an F-TED with a triangular p-n junction structure was designed. This structure effectively increased the length of the TE legs without adding vertical space, thereby facilitating the establishment of a larger temperature difference. Additionally, according to the principle of energy band alignment, Cu tape and Ag paste were respectively selected as the contact electrodes for the n-type legs and p-type legs, respectively. The optimized device achieved a ω_n of 4.8 $\mu W \cdot cm^{-2} \cdot K^{-2}$ under a 20 K temperature difference and reached a ΔT_{max} of 29.8 K when driven by a current of 92.4 mA [36]. To meet customization for different heat sources and power, Sun et al. developed a F-TED with self-healing and modular assembly capabilities [246]. By selectively encapsulating the liquid metal EGaIn electrodes with carbon nanotube-doped self-repairing materials, the κ between electrodes and the TE legs was enhanced to 0.9 $W \cdot m^{-1} \cdot K^{-1}$, significantly reducing parasitic heat loss. Compared with the non-selectively encapsulated devices, this selective encapsulation strategy resulted in a 185% increased ΔT across the TE legs and a 171% increase P_{out}. Ultimately, an excellent ω_n of 3.14 $\mu W \cdot cm^{-2} \cdot K^{-2}$ was achieved. Benefiting from the dynamic disulfide bonds and hydrogen bonds in the disulfide cross-linked polyurethane (DSPU) matrix, as well as the fluidity of EGaIn electrodes, this F-TED gained remarkable ability of autonomous repairing at room temperature, restoring its mechanical and electrical properties. Moreover, the design features Lego-like modular assembly capability, allowing for series

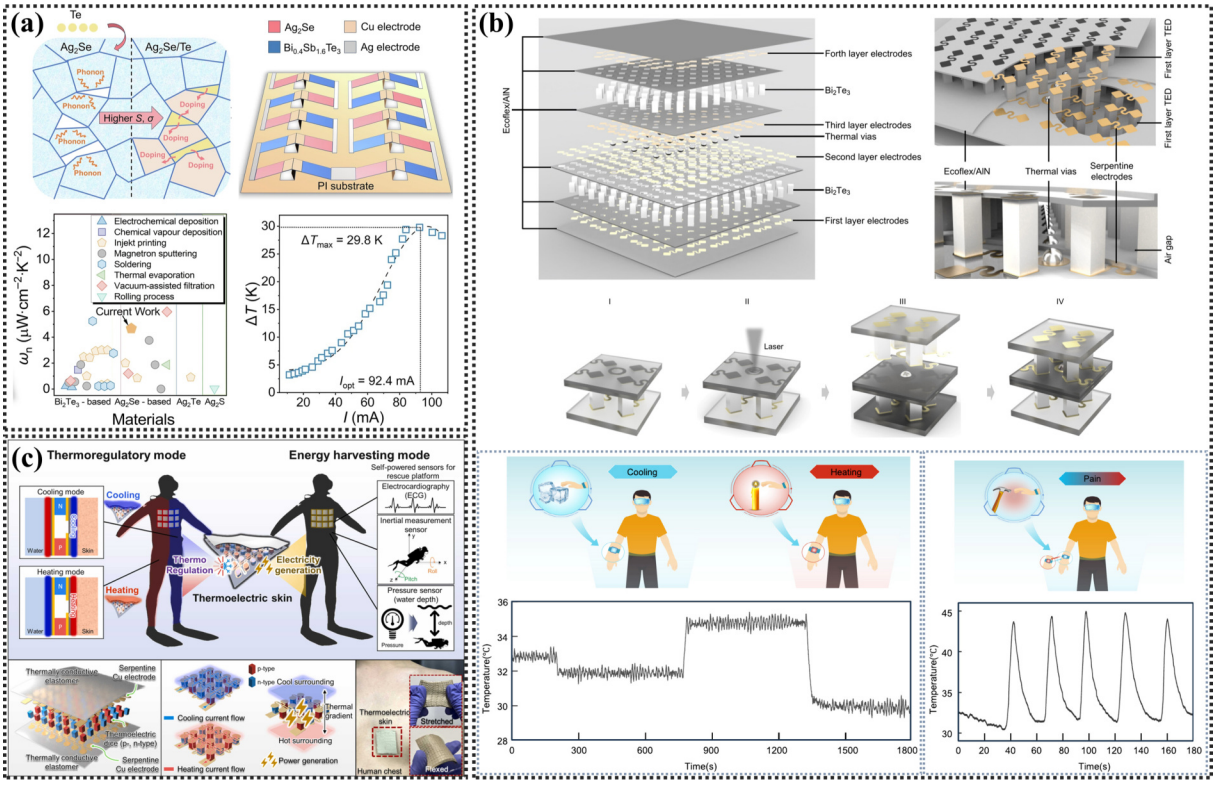

Figure 20 Applications of F-TECs. (a) Screen-printed Ag_2Se/Te films used for cooling. Reproduced with permission from Ref. [36], © Chen, W. Y. et al. 2025. (b) Stretchable F-TED with 3D stacked structure used for virtual sensation. Reproduced with permission from Ref. [52]. © American Chemical Society 2025. (c) Multimodal TE skins used for underwater energy collection and human body temperature regulation. Reproduced with permission from Ref. [318], © Elsevier Ltd. 2022.

connection via exposed liquid metal electrodes, with the output voltage increasing linearly with the number of modules. A stacked double-layer tower structure further enhanced ΔT_{max} to 6.2 K. These applications demonstrate the potential of the active cooling functionality of F-TEDs for thermal management [246].

When applying an electric current to a TED for active cooling, the hot and cold sides can be swapped by reversing the current direction. Thus, TECs are also widely used in scenarios requiring dynamic heating and cooling [319]. For instance, the cooling performance in stretchable F-TEDs is limited by the poor heat dissipation caused by the extremely low κ of elastic encapsulation materials. To address this core issue, Huang et al. successfully fabricated a high-performance stretchable TED by stacking multilayer TE unit, as depicted in Fig. 20(b) [52]. They optimized the packaging materials by incorporating the aluminum nitride (AlN) nanoparticles into the Ecoflex elastomer to enhance its heat conduction properties. Further, a 3D stacking structure was innovatively proposed, integrating two layers of TE unit networks. The thermal transfer efficiency between the layers was significantly improved by thermal vias created by through laser ablation technology. The manufactured device exhibited excellent stretchability, with a resistance change of less than 1% at 30% strain, and outstanding temperature regulation capability of stable 10 °C skin cooling. Due to the TED's advantages, such as higher precision, lower overheating risk, and greater cooling capacity compared to resistive heating, a closed-loop temperature control system based this stacked TED was developed for rapid and precise programmed control of skin temperature, not only realizing virtual thermal sensation but also simulating virtual pain perception through the thermal grill illusion effect [52]. Furthermore, Yeongju Jung et al. specifically designed a soft and stretchable multi-modal TED for underwater environments, which can simultaneously achieve energy collection and temperature regulation [318]. Due to the significant temperature gradient between seawater and human skin, as well as the circulating seawater being able to immediately absorb the heat generated at the hot side, the challenges of lower output efficiency for TED can be naturally solved underwater. Meanwhile, this device could be freely stretched and adhered to complex surfaces because of the stretchable serpentine circuit array and the thermally conductive elastic substrate. As a proof of concept, multiple TE units were integrated into a diving suit, constructing a self-powered platform that could self-power the wireless embedded physiological sensors in real time and keep body temperature to availably prevent hypothermia through a proportional–integral–derivative (PID) feedback algorithm. These results demonstrated its enormous potential in underwater rescue and special operations [318]. Additionally, owing to the precise temperature control capability of TEDs, they have also been attempted for de-icing, and the flexible devices are more advantageous for adhering to target surfaces [320]. F-TECs capable of active cooling and heating are being applied in increasingly diverse fields. However, their high performance, reliability, and large-scale fabrication still require further verification.

7.3 F-TE sensors

Flexible electronic skin (FES) is a soft material that mimics the characteristics and functions of human skin [321–324]. It integrates various sensors, electronic components and functional units, possessing flexibility, stretchability and biocompatibility. Thereby, it can perceive environmental conditions like real skin,

such as pressure, temperature, humidity and airflow, converting these physical or chemical signals into electrical signals for processing and transmission [325]. Based on the temperature-voltage correspondence during operation, TEDs are widely utilized for precise temperature identification [290, 326]. Compared with traditional thermistors and resistance temperature detectors, TEDs have advantages such as wider operating temperature range, superior mechanical stability and longer service life. To achieve high spatial and temporal resolution for biomimetic temperature sensing, it is necessary to address the additional resistance introduced by the splicing process and to effectively separate the hot and cold sides for obtaining needful temperature gradient [327]. As shown in Fig. 21(a), Chen et al. reported a jointless p-n integrated TE composite fabricated via a selective filtration method. By optimizing the filtration rate and pressure, the width of the p-n junction between p-type SWCNTs and n-type Bi_2Te_3 was reduced to approximately 2 mm, significantly lowering the interfacial barriers. This device structure did not require the conductive materials. Instead, a polylactic acid (PLA) insulating layer was introduced between the TE module and the heat source to limit the hot end to only contact the p-n junction, thereby forming a temperature gradient in the horizontal direction. This jointless p-n integrated TED achieved a P_{out} of 3.07 mV at ΔT of 30 K, and exhibited excellent linear response, fast response time (<0.1 s), and low signal fluctuation. Furthermore, developed an intelligent TE sensing system choosing this jointless module as sensing element. When integrating it into the robotic arm, this system demonstrated accurate identification of heat source temperature with a temporal resolution below 0.1 K and enabled independent temperature perception and response for each area smaller than 1 cm × 1 cm with high spatial resolution. If a heat source approached the robotic arm and exceeded the set temperature threshold, the corresponding finger will perform a bouncing action [327]. This research provides a new strategy for the application of bionic temperature sensors in fields such as humanoid robotics and health monitoring. Moreover, Fig. 21(b) illustrated a dual-modal sensing arrays that combined a stepped micro-cone pressure sensing array with a Bi_2Te_3-based temperature sensing array [53]. For such multimodal sensors, avoiding interference between different signals and decoupling these signals are the primary issues that needs to be addressed. By adopting a vertical integration structure of TE/pressure sensing arrays, this sensor device not only ensures the wide range (0.032–27 kPa), high sensitivity and fast response (18 ms) characteristics of the pressure sensing array, but also does not cause cross-interference with the temperature signal during operation. And with the deep learning algorithm, the accuracy rate of this dual-modal sensing array in the object recognition task was as high as 98.3% [53]. Furthermore, the perception of multiple physical quantities within a single device based on different sensing mechanisms has also become a research focus. Recently, Zeng et al. achieved simultaneous sensing and output of piezoelectric and TE signals in the out-of-plane direction within a mesh structure composed of obliquely grown Te-NWs. This flexible multimodal sensor exhibited a strain sensitivity of 0.454 V, a strain rate sensitivity of 0.0154 V s, and a temperature sensitivity

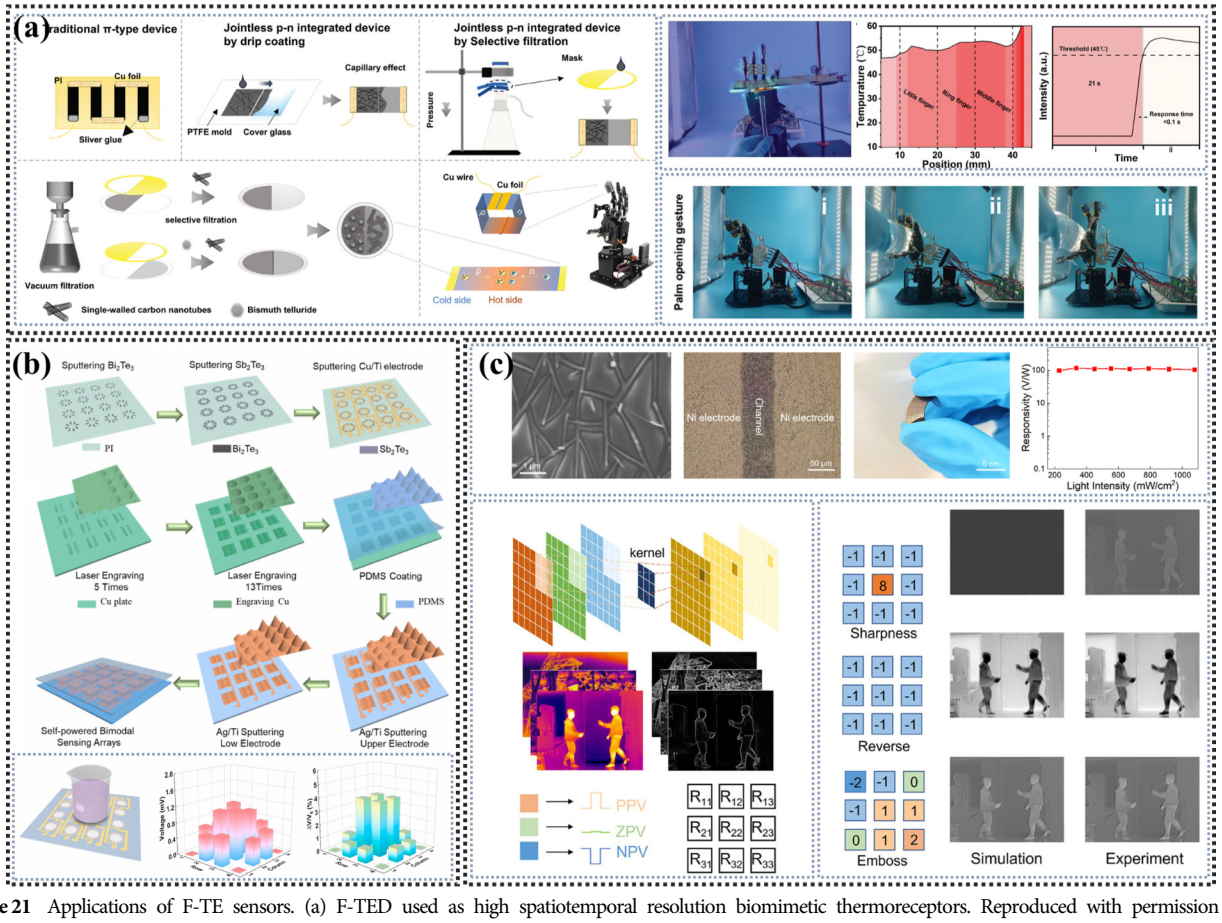

Figure 21 Applications of F-TE sensors. (a) F-TED used as high spatiotemporal resolution biomimetic thermoreceptors. Reproduced with permission from Ref. [327], © Wiley-VCH GmbH 2024. (b) Bi_2Te_3-based F-TED for self-powered temperature-pressure sensing. Reproduced with permission from Ref. [53], © Published by Elsevier Ltd. 2024. (c) Flexible photothermoelectric Te nanomesh arrays used for Infrared in-sensor computing. Reproduced with permission from Ref. [328], © Liao, J. C. et al. Advanced Materials published by Wiley-VCH GmbH 2025.

of 225.1 μV·K^{-1}, which was superior to most reported multimodal sensors [329]. Furthermore, the accurate temperature detection precision and rapid temporal response of TE temperature detectors also make them widely applicable in the fields of early fire warning and intelligent fire safety monitoring [330–332]. For instance, Zhou et al. reported a TE yarn fabricated based on CNTs films, through a combination of chemical modification and mechanical twisting processes. By weaving these yarns into firefighting suits, a self-powered wireless fire warning system can be constructed. It performed stably at high temperatures (>500 K) and exhibited ultra-fast response characteristics (threshold voltage 2 mV, response time < 0.5 s), capable of real-time sensing of temperature gradients and heat source distance in fire environments [331, 333].

Some traditional inorganic semiconductor TE materials, such as copper sulfide (CuS), SnSe, Bi_2Te_3 and PbSe, possess localized surface plasmon resonance effect or narrow bandgap, which can efficiently absorb light and generate heat [334–337]. Moreover, conductive polymers like PPy and PANI, have favorable photothermal effects and flexible processability. They are often combined with carbon materials, including graphene and CNTs, or inorganic nanomaterials to synergistically enhance their photothermal performance [336, 338–340]. Hence, the development of photothermoelectric (PTE) materials shows great application potential in industrial detection, homeland security, medical diagnostics and other fields [341–344]. For instance, Liao et al. developed a flexible PTE detector array based on a Te nanomesh, which realized infrared in-sensor computing (Fig. 21(c)) [328]. They employed a multi-scale vdW growth method to deposit Te nanomesh on a PI substrate at low temperature of 150 °C. Benefit from self-welding process, the Te nanomesh could achieved good contact via lateral vapor growth, showing excellent mechanical and electrical properties. Leveraging the photothermal effect and the Seebeck effect, the detector demonstrated a high responsivity of 120 V·W^{-1} and a S of 356 μV·K^{-1} under 1550 nm infrared light, operating without external power source. Due to the unique high-symmetry bidirectional response of Te nanomesh, it was suitable for convolution kernel, enabling to edge detection and feature extraction with an accuracy highly consistent with the simulation results [328]. Similarly, Guo et al. presented a flexible and wearable infrared detector that combines photothermal-electric coupling with a Te-based TE multilayer film and an infrared-absorbing PI substrate, achieving contactless thermosensation over a wide temperature range [345]. It is evident that the development of F-TE sensors is expanding from conventional temperature measurement into emerging fields such as healthcare, the Internet of Things and advanced robotics, among others.

8 Conclusions and outlooks

This review systematically summarizes recent advancements in flexible TE materials and devices. It includes fundamental theories, optimization of various flexible TE materials, strategies for device design, as well as construction and performance of film-based and fibrous F-TEDs. It also emphasizes the wide applications of F-TEDs in energy harvesting, cooling and sensing. Finally, this review highlights the major challenges and prospects for future development as follows:

(1) Material optimization: Although the development of F-TE materials has progressed significantly over the past decades, their output performance still falls short compared to that of bulk materials. On one hand, the development of plastic inorganic TE materials lies in overcoming the inherent trade-off between TE performance and mechanical flexibility. Deeper investigations into their evolution mechanisms will provide valuable insights for the innovative development of these materials. On the other hand, the improvement of organic TE materials depends on seeking a balance between S and σ through reasonable molecular structure design and appropriate doping regulation. For organic/inorganic TE composite materials, a high loading fraction of inorganic TE components with strong interfacial coupling will lead to satisfactory output performance. This will benefit from the compatibility of various components and the precise control of phase structure during the preparation process.

(2) Durability and stability: Flexible devices are generally required to endure frequent deformations. Thus, the interfaces between components become the main bottleneck that affects the reliability and stability of flexible devices. The Ag paste and Cu wires are the most common connection materials used in flexible devices. However, they usually lack flexibility or stretchability. Exploring new conductive materials, such as liquid metals or Ag nanowires, as interconnection materials may help alleviate the reliability issues at the interfaces. Additionally, various designs of flexible circuits that can relieve the stress concentration are also worth considering. Furthermore, the devices will have an extended service life with additional encapsulation. Finally, it is essential to assess the devices flexibility, stretchability, durability and stability under complex conditions.

(3) Thermal management: Effective thermal management can enhance the output power or cooling efficiency of F-TEDs. To achieve efficient heat collection and dissipation, it is crucial to use thermal interface materials that exhibit high thermal conductivity, excellent flexibility, and strong interfacial adhesion. This combination can make the best of minute temperature gradient. Additionally, the temperature gradient within confined spaces can be further expanded by integrating other thermal management materials, such as radiative cooling materials, photothermal conversion materials, and phase change materials.

(4) Integrations: From the perspective of practical application, the energy harvested by F-TEDs from the human body or the environment is both extremely limited, and unstable due to human activities and environment temperature fluctuations. This leads to a severe mismatch between the TE power supply module and the stable, higher voltage/current requirements of downstream electronic components. Therefore, it is necessary to develop interfaces, flexible integrated circuits, and functional modules with low resistance from a holistic system perspective. Furthermore, the synergistic effect of various forms of energy such as light, heat, and electricity can be achieved within a single device by integrating TE components with other energy conversion modules, which can effectively mitigate the limitations of single-mode energy collection.

(5) Artificial intelligence (AI): In the field of TE research, the introduction of AI is expected to accelerate the discovery of new materials through the combination of machine learning models and high-throughput screening, thereby reducing trial-and-error costs. Furthermore, it can also help simulate the thermal stress distribution and electrical output of devices under various conditions, achieving system-level device design and optimization, etc. And a standardized database is urgently needed to be established.

Ultimately, the future advancement of F-TEDs will depend on synergistic, multidisciplinary innovation encompassing materials

design, device engineering, circuit optimization, and system-level integration, paving the way toward fully self-powered, intelligent, and sustainable wearable electronics.

Acknowledgements

The authors thank the support of the National Key R&D Program of China (2024YFB3816000 and 2024FYB3814102), the National Natural Science Foundation of China (Nos. 52401258, 52125205, 52250398, 52192614 and 52532005), Natural Science Foundation of Beijing Municipality (L223006 and 2222088), Shenzhen Science and Technology Program (Grant No. KQTD20170810105439418), and the Fundamental Research Funds for the Central Universities. The authors also thank Xuzhou B&C Chemical Co. Ltd for providing the photoresist (HTA116, HTA112, B&C Chemicals) used in our work.

Declaration of conflicting interests

The authors declare no conflicting interests regarding the content of this article.

Data availability

All data needed to support the conclusions in the paper are presented in the manuscript and/or the Supplementary Materials. Additional data related to this paper may be requested from the corresponding author upon request.

References

[1] Zhou, K. K.; Zhao, Y.; Sun, X. P.; Yuan, Z. Q.; Zheng, G. Q.; Dai, K.; Mi, L. M.; Pan, C. F.; Liu, C.; Shen, C. Y. Ultra-stretchable triboelectric nanogenerator as high-sensitive and self-powered electronic skins for energy harvesting and tactile sensing. *Nano Energy* **2020**, *70*, 104546.

[2] Zheng, Y.; Liu, T.; Wu, J. P.; Xu, T. T.; Wang, X. D.; Han, X.; Cui, H. Z.; Xu, X. F.; Pan, C. F.; Li, X. Y. Energy conversion analysis of multilayered triboelectric nanogenerators for synergistic rain and solar energy harvesting. *Adv. Mater.* **2022**, *34*, 2202238.

[3] Zhang, L.; Shang, H. J.; Dong, H.; Gu, H. W.; Ding, F. Z. Ultra-high-performance Ag_2Se-based flexible thermoelectric generator. *Energy Environ. Sci.* **2025**, *18*, 8292–8302.

[4] Zhou, S. S.; Shi, X. L.; Li, L.; Liu, Q.; Hu, B. X.; Chen, W. Y.; Zhang, C. Y.; Liu, Q. F.; Chen, Z. G. Advances and outlooks for carbon nanotube-based thermoelectric materials and devices. *Adv. Mater.* **2025**, *37*, 2500947.

[5] Shi, X. L.; Li, N. H.; Li, M.; Chen, Z. G. Toward efficient thermoelectric materials and devices: Advances, challenges, and opportunities. *Chem. Rev.* **2025**, *125*, 7525–7724.

[6] Zhang, C.; Xiao, R. F.; Wu, M. X.; Wu, T. X.; Liu, X.; Gan, F.; Zhao, J.; Mo, J. P.; Chen, S. Z.; Che, C. Y. et al. High-performance jointless all-organic Ohmic junction thermoelectric generators. *Nano Energy* **2025**, *142*, 111188.

[7] Ma, X. J.; Lin, C. H.; Yang, H. Y.; Fu, Y. H.; Liang, K.; Bao, X.; Ye, S.; Wang, J.; Zhao, P.; Chen, J. et al. Elevating thermoelectric performance in the sub-ambient temperature range for electronic refrigeration. *Innovation* **2025**, *6*, 100864.

[8] Shi, H. N.; Wen, Y.; Bai, S. L.; Chang, C.; Su, L. Z.; Gao, T.; Liu, S. B.; Liu, D. R.; Qin, B. C.; Qin, Y. X. et al. Crystal symmetry modification enables high-ranged in-plane thermoelectric performance in n-type SnSe crystals. *Nat. Commun.* **2025**, *16*, 1788.

[9] Wang, S. Q.; Bai, S. L.; Chen, P. P.; Zhan, S. P.; Tian, Y.; Wang, L.; Liu, D. R.; Peng, J. Y.; Li, Y. C.; Gao, D. Z. et al. Off-center distortions and resonant levels: A pathway to enhance power generation and thermoelectric cooling in PbSe crystals. *J. Am. Chem. Soc.* **2025**, *147*, 15827–15837.

[10] Chen, Y.; Wang, T. Y.; Gao, G. H.; The principles and recent advancements in self-powered wearable fiber sensors. *Mater. Chem. Front.* **2025**, *9*, 1618–1649.

[11] Cheng, H.L.; Wang, Z. Y.; Guo, Z. J.; Lou, J.; Han, W. J.; Rao, J.; Peng, F. Cellulose-based thermoelectric composites: A review on mechanism, strategies and applications. *Int. J. Biol. Macromol.* **2024**, *275*, 132908.

[12] Lu, Y.; Zhou, Y.; Wang, W.; Hu, M. Y.; Huang, X. G.; Mao, D. S.; Huang, S.; Xie, L.; Lin, P. J.; Jiang, B. B. et al. Staggered-layer-boosted flexible Bi_2Te_3 films with high thermoelectric performance. *Nat. Nanotechnol.* **2023**, *18*, 1281–1288.

[13] Wang, X. M.; Chen, Z. W.; Zhang, S. X.; Zhang, X. Y.; Zhou, R.; Li, W.; Luo, J. Pei, Y. Z. Enhanced cryogenic thermoelectric cooling of $Bi_{0.5}Sb_{1.5}Te_3$ by carrier optimization. *InfoMat* **2025**, *7*, e12663.

[14] Zhao, L. D.; Lo, S. H.; Zhang, Y. S.; Sun, H.; Tan, G. J.; Uher, C.; Wolverton, C.; Dravid, V. P.; Kanatzidis, M. G. Ultralow thermal conductivity and high thermoelectric figure of merit in SnSe crystals. *Nature* **2014**, *508*, 373–377.

[15] Liu, D. R.; Wang, D. Y.; Hong, T.; Wang, Z. Y.; Wang, Y. P.; Qin, Y. X.; Su, L. Z.; Yang, T. Y.; Gao, X.; Ge, Z. H. et al. Lattice plainification advances highly effective SnSe crystalline thermoelectrics. *Science* **2023**, *380*, 841–846.

[16] Ning, X. K.; Ran, Y. M.; Han, J. Y.; Wang, S. F. Unlocking room-temperature thermoelectric and flexibility in freestanding single-crystalline SnSe membrane through metastable-phase engineering. *Adv. Funct. Mater.*, in press, DOI: 10.1002/adfm.202518193.

[17] Qin, Y. X.; Qin, B. C.; Hong, T.; Zhang, X.; Wang, D. Y.; Liu, D. R.; Wang, Z. Y.; Su, L. Z.; Wang, S. N.; Gao, X. et al. Grid-plainification enables medium-temperature PbSe thermoelectrics to cool better than Bi_2Te_3. *Science* **2024**, *383*, 1204–1209.

[18] Gao, D. Z.; Wen, Y.; Bai, S. L.; Wang, S. Q.; Liu, S. B.; Li, Y. C.; Wang, L.; Zang, W. J.; Su, X. L.; Gao, X. et al. Robustly boosting thermoelectric performance of n-type PbSe via lattice plainification and dynamic doping. *Small* **2024**, *20*, 2407556.

[19] Zhao, P.; Xue, W. H.; Zhang, Y.; Zhi, S. Z.; Ma, X. J.; Qiu, J. M.; Zhang, T. Y.; Ye, S.; Mu, H. M.; Cheng, J. X. et al. Plasticity in single-crystalline Mg_3Bi_2 thermoelectric material. *Nature* **2024**, *631*, 777–782.

[20] Hu, B. X.; Shi, X. L.; Cao, T. Y.; Liu, S. Q.; Zhang, M.; Lyu, W. Y.; Yin, L. C.; Tesfamichael, T.; Liu, Q. F.; Chen, Z. G. High-performing flexible Mg_3Bi_2 thin-film thermoelectrics. *Adv. Sci.* **2024**, *11*, 2409788.

[21] Bao, X.; Liu, K. J.; Xue, W. H.; Yao, H. H.; Ma, X. J.; Li, X. F.; Ye, S.; Cao, F.; Mao, J.; Zhang, Q. Multiscale phonon scattering for ultra-low thermal conductivity in Co-doped ZrCoBi half-heusler. *Adv. Funct. Mater.* **2024**, *34*, 2404279.

[22] Duan, S. C.; Bao, X.; Huang, J. W.; Shi, R. P.; Fei, L. F.; Xue, W. H.; Yao, H. H.; Li, X. F.; Wang, J.; Liu, X. J. et al. Spinodal decomposition promoting high thermoelectric performance in half-heusler. *Joule* **2025**, *9*, 101854.

[23] Qin, B. C.; Wang, D. Y.; Liu, X. X.; Qin, Y. X.; Dong, J. F.; Luo, J. F.; Li, J. W.; Liu, W.; Tan, G. J.; Tang, X. F. et al. Power generation and thermoelectric cooling enabled by momentum and energy multiband alignments. *Science* **2021**, *373*, 556–561.

[24] Li, N. H.; Shi, X. L.; Zhang, C.; Li, M.; Wang, X. D.; Zhang, M.; Chen, W. Y.; Chen, Y. Q.; Golberg, D.; Qi, D. C. et al. Manganese doping induced record-high medium-temperature AgCuTe thermoelectrics. *Energy Environ. Sci.* **2025**, *18*, 8860–8875.

[25] Wu, H.; Shi, X. L.; Li, M.; Gao, H.; Liu, W. D.; Zhu, M.; Yin, L. C.; Wang, D. Z.; Duan, J. G.; Chen, Z. G. et al. Sandwich engineering advances ductile thermoelectrics. *Adv. Mater.* **2025**, *37*, 2503020.

[26] Li, H. T.; Chen, L. D.; Guo, Z.; Wu, G.; Tan, X. J.; Zhang, Q.; Cai, J. F.; Sun, Q. Q.; Noudem, J. G.; Sun, P. et al. Ultra-low lattice thermal conductivity realizing ultra-high performance

$Bi_{0.48}Sb_{1.52}Te_3$-based thermoelectric material and module. *Energy Environ. Sci.* **2024**, *17*, 6091–6101.
[27] Haldar, I.; Taneja, V.; Goyal, N.; Ubaid, M.; Sarkar, D.; Kedia, D. K.; Saurabh, K.; Singh, S.; Pal, K.; Ravishankar, N. et al. Conduction band convergence and modular nanostructures: Driving high thermoelectric performance in n-type PbSe. *Angew. Chem., Int. Ed.* **2025**, *64*, e202510305.
[28] Jang, H.; Ahn, J.; Jeong, Y.; Ha, J. H.; Jeong, J. H.; Oh, M. W.; Park, I.; Jung, Y. S. Flexible all-inorganic thermoelectric yarns. *Adv. Mater.* **2024**, *36*, 2408320.
[29] Gong, Y. R.; Ying, P.; Zhang, Q. T.; Liu, Y. Q.; Huang, X. Q.; Dou, W.; Zhang, Y. J.; Li, D.; Zhang, D. W.; Feng, T. et al. Realizing the high thermoelectric performance of highly preferentially oriented SnSe based nanorods via band alignment. *Energy Environ. Sci.* **2024**, *17*, 1612–1623.
[30] Ge, B. Z.; Lee, H.; Im, J.; Choi, Y.; Kim, S. Y.; Lee, J. Y.; Cho, S. P.; Sung, Y. E.; Choi, K. Y.; Zhou, C. J. et al. Engineering an atomic-level crystal lattice and electronic band structure for an extraordinarily high average thermoelectric figure of merit in n-type PbSe. *Energy Environ. Sci.* **2023**, *16*, 3994–4008.
[31] Yang, Q. Y.; Yang, S. Q.; Qiu, P. F.; Peng, L. M.; Wei, T. R.; Zhang, Z.; Shi, X. Chen, L. D. Flexible thermoelectrics based on ductile semiconductors. *Science* **2022**, *377*, 854–858.
[32] Du, J. J.; Zhang, B. T.; Jiang, M.; Zhang, Q. H.; Zhang, K. Y.; Liu, Y.; Wang, L. J.; Jiang, W. Inkjet printing flexible thermoelectric devices using metal chalcogenide nanowires. *Adv. Funct. Mater.* **2023**, *33*, 2213564.
[33] Yu, M.; Li, H.; Li, Y. C.; Wang, S. H.; Li, Q. K.; Wang, Y. P.; Li, B. B.; Zhu, K.; Liu, W. S. Ionic thermoelectric gels and devices: Progress, opportunities, and challenges. *EnergyChem* **2024**, *6*, 100123.
[34] Chi, C.; Liu, G. Z.; An, M.; Zhang, Y. F.; Song, D. X.; Qi, X.; Zhao, C. Y.; Wang, Z. Q.; Du, Y. Z.; Lin, Z. Z. et al. Reversible bipolar thermopower of ionic thermoelectric polymer composite for cyclic energy generation. *Nat. Commun.* **2023**, *14*, 306.
[35] Wang, Y. F.; Mwakitawa, I. M.; Yang, H.; Song, M. Y.; Huang, Q.; Li, X. Z.; Zhang, P. C.; Fang, W.; Hu, L. J.; Zhou, Y. L. et al. Advancing ionic thermoelectric materials for heat recovery. *Prog. Mater. Sci.* **2026**, *156*, 101575.
[36] Chen, W. Y.; Li, M.; Wang, X. D.; Otte, J.; Zhang, M.; Zhang, C. Y.; Cao, T. Y.; Hu, B. X.; Li, N. H.; Liu, W. D. et al. Flexible Ag_2Se-based thin-film thermoelectrics for sustainable energy harvesting and cooling. *Nat. Commun.* **2025**, *16*, 7579.
[37] Zheng, Y. Y.; Zhang, Q. H.; Jin, W. L.; Jing, Y. Y.; Chen, X. Y.; Han, X.; Bao, Q. Y.; Liu, Y. P.; Wang, X. H.; Wang, S. R. et al. Carbon nanotube yarn based thermoelectric textiles for harvesting thermal energy and powering electronics. *J. Mater. Chem. A* **2020**, *8*, 2984–2994.
[38] Lee, B.; Cho, H.; Park, K. T.; Kim, J. S.; Park, M.; Kim, H.; Hong, Y.; Chung, S. High-performance compliant thermoelectric generators with magnetically self-assembled soft heat conductors for self-powered wearable electronics. *Nat. Commun.* **2020**, *11*, 5948.
[39] Liu, Y.; Zhang, Q. H.; Huang, A. B.; Zhang, K. Y.; Wan, S.; Chen, H. Y.; Fu, Y. T.; Zuo, W. S.; Wang, Y. Z.; Cao, X. et al. Fully inkjet-printed Ag_2Se flexible thermoelectric devices for sustainable power generation. *Nat. Commun.* **2024**, *15*, 2141.
[40] Wei, T. R.; Qiu, P. F.; Zhao, K. P.; Shi, X. Chen, L. D. Ag_2Q-based (Q=S, Se, Te) silver chalcogenide thermoelectric materials. *Adv. Mater.* **2023**, *35*, 2110236.
[41] Chen, X. Y.; Li, J. H.; Wang, J. R.; Meng, Q. Y.; Li, S. Y.; Ding, T. P.; Yang, J. M.; Mao, D. S.; Hu, M. Y.; He, J. Q. Single-crystal SnSe film for high-performance flexible thermoelectric generators. *Chem. Mater.* **2025**, *37*, 7316–7325.
[42] Liu, K.; Wang, J. Y.; Pan, X. R.; Tian, S. Y.; Liu, Y. D.; Zhang, Z.; Di, Y. Q.; Chen, J. P.; Wu, C. W.; Deng, X. Y. et al. n-Type thermoelectric elastomers. *Nature* **2025**, *644*, 920–926.
[43] Zhao, Y.; Li, Z. Y.; Wang, D. Y.; Zhang, X.; Ji, Z.; Niu, L. X.; Di, Y. Q.; Guan, Y.; Liu, L. Y.; Zou, Y. et al. High performance and colorful polymer thermoelectrics with imprinted porous film. *Adv. Mater.* **2024**, *36*, 2407692.
[44] Zhang, L.; Shi, X. L.; Shang, H. J.; Gu, H. W.; Chen, W. Y.; Li, M.; Huang, D. X.; Dong, H.; Wang, X. L.; Ding, F. Z. et al. High-performance Ag_2Se-based thermoelectrics for wearable electronics. *Nat. Commun.* **2025**, *16*, 5002.
[45] Liu, Y. M.; Shi, X. L.; Li, M.; Cao, T. Y.; Wu, H.; Wang, D. Z.; Wu, T.; Yin, L. C.; Liu, W. D.; Chen, Z. G. et al. Cu_2Se hybridization advances high-performance flexible single-walled carbon nanotube based thermoelectrics. *J. Colloid Interface Sci.* **2025**, *698*, 138049.
[46] Yang, Y.; Hu, H. J.; Chen, Z. Y.; Wang, Z. Y.; Jiang, L. M.; Lu, G. X.; Li, X. J.; Chen, R. M.; Jin, J.; Kang, H. C. et al. Chen, Y. Stretchable nanolayered thermoelectric energy harvester on complex and dynamic surfaces. *Nano Lett.* **2020**, *20*, 4445–4453.
[47] Wang, D. Y.; Ding, J. M.; Ma, Y. Q.; Xu, C. L.; Li, Z. Y.; Zhang, X.; Zhao, Y.; Zhao, Y.; Di, Y. Q.; Liu, L. Y. et al. Multi-heterojunctioned plastics with high thermoelectric figure of merit. *Nature* **2024**, *632*, 528–535.
[48] Lee, J. A.; Aliev, A. E.; Bykova, J. S. ; de Andrade, M. J.; Kim, D.; Sim, H. J.; Lepró, X.; Zakhidov, A. A.; Lee, J. B.; Spinks, G. M. et al. Woven-yarn thermoelectric textiles. *Adv. Mater.* **2016**, *28*, 5038–5044.
[49] Liang, L. L.; Liu, X. S.; Li, P.; Wang, W.; Kuang, N. L.; Zhang, Y.; Kang, Y. M.; Yao, G.; Huang, Z. L.; Zhou, C. J. et al. A wearable multimodal health monitoring bracelet powered by high-power-density flexible thermoelectric generators. *Device* **2025**, *3*, 100748.
[50] Zhang, Y. W.; Ge, B. Z.; Feng, J. H.; Kuang, N. L.; Ye, H. L.; Yuan, Z. L.; Wu, M. Y.; Jiang, B. B.; Li, J.; Sun, Q. et al. High-performance self-powered flexible thermoelectric device for accelerated wound healing. *Adv. Funct. Mater.* **2024**, *34*, 2403990.
[51] Zhu, P. C.; Luo, X. P.; Lin, X. R.; Qiu, Z. C.; Chen, R. R.; Wang, X. C.; Wang, Y. L.; Deng, Y.; Mao, Y. C. A self-healable, recyclable, and flexible thermoelectric device for wearable energy harvesting and personal thermal management. *Energy Convers. Manage.* **2023**, *285*, 117017.
[52] Huang, Z. L.; Yang, L. P.; Chen, T.; Zhou, R.; Jiang, Y.; Jiang, B. B.; Xue, D. F.; Lin, Y. Three-dimensional stacked stretchable thermoelectric device for virtual sensation. *ACS Appl. Mater. Interfaces* **2025**, *17*, 5446–5454.
[53] Wang, Y. L.; Sun, Y.; Li, W. Q.; Li, P.; Wang, J.; Zhu, P. C.; Qi, S. Y.; Tang, J. H.; Deng, Y. Self-powered temperature pressure sensing arrays with stepped microcone structure and Bi_2Te_3-based films for deep learning-assisted object recognition. *Mater. Today Phys.* **2024**, *49*, 101588.
[54] He, C. J.; Shi, X. L.; Li, N. H.; Li, M.; Pei, J. Chen, Z. G. Ductile inorganic thermoelectrics: Advances, challenges, and perspectives. *Adv. Energy Mater.* **2025**, *15*, e03115.
[55] Qiu, P. F.; Deng, T. T.; Chen, L. D.; Shi, X. Plastic inorganic thermoelectric materials. *Joule* **2024**, *8*, 622–634.
[56] Tang, J. H.; Pai, Y. H.; Liang, Z. Q. Strategic insights into semiconducting polymer thermoelectrics by leveraging molecular structures and chemical doping. *ACS Energy Lett.* **2022**, *7*, 4299–4324.
[57] Li, H.; Song, J.; Xiao, J.; Wu, L. L.; Katz, H. E.; Chen, L. D. Synergistically improved molecular doping and carrier mobility by copolymerization of donor-acceptor and donor-donor building blocks for thermoelectric application. *Adv. Funct. Mater.* **2020**, *30*, 2004378.
[58] Liu, J. Z.; Chen, S. Q.; Ju, Y. Y.; Zhuo, M. P.; Zhang, K. Q. Research progress in flexible solar thermoelectric devices. *Mater. Today* **2025**, *88*, 585–596.
[59] Zhang, L.; Shi, X. L.; Yang, Y. L.; Chen, Z. G. Flexible thermoelectric materials and devices: From materials to applications. *Mater. Today* **2021**, *46*, 62–108.
[60] Hao, Y. N.; He, X. Y.; Wang, L. M.; Qin, X. H.; Chen, G. M.; Yu,

J. Y. Stretchable thermoelectrics: Strategies, performances, and applications. *Adv. Funct. Mater.* **2022**, *32*, 2109790.
[61] Blackburn, J. L.; Ferguson, A. J.; Cho, C. Grunlan, J. C. Carbon-nanotube-based thermoelectric materials and devices. *Adv. Mater.* **2018**, *30*, 1704386.
[62] Shah, S. Z. H.; Tjiu, W. W.; Dai, H. W.; Recatala-Gomez, J.; Kasongo-Ntumba, P.; Serrano-Claumarchirant, J. F.; Zhang, W. M.; Repaka, D. V. M.; McCullough, I.; Fenwick, O. et al. Enhanced charge transport at the interface in P3HT-tellurium nanowires hybrid materials for high thermoelectric performance. *Adv. Funct. Mater.* **2026**, *36*, e15055.
[63] Wei, T. R.; Guan, M. J.; Yu, J. J.; Zhu, T. J.; Chen, L. D.; Shi, X. How to measure thermoelectric properties reliably. *Joule* **2018**, *2*, 2183–2188.
[64] Li, N. H.; Shi, X. L.; Liu, S. Q.; Li, M.; Cao, T. Y.; Zhang, M.; Lyu, W. Y.; Liu, W. D.; Qi, D. C.; Chen, Z. G. Strategic vacancy engineering advances record-high ductile AgCu(Te, Se, S) thermoelectrics. *Nat. Commun.* **2025**, *16*, 2812.
[65] Liu, S. B.; Wen, Y.; Bai, S. L.; Shi, H. N.; Qin, Y. X.; Qin, B. C.; Liu, D. R.; Cao, Q.; Gao, X.; Su, L. Z. et al. Lattice plainification leads to high thermoelectric performance of p-type PbSe crystals. *Adv. Mater.* **2024**, *36*, 2401828.
[66] Zhu, Y. C.; Wang, D. Y.; Hong, T.; Hu, L.; Ina, T.; Zhan, S. P.; Qin, B. C.; Shi, H. N.; Su, L. Z.; Gao, X. et al. Multiple valence bands convergence and strong phonon scattering lead to high thermoelectric performance in p-type PbSe. *Nat. Commun.* **2022**, *13*, 4179.
[67] Wen, N. X.; Guan, X.; Zuo, X. Q.; Guo, Y.; Chen, Z. H.; Li, C. W.; Xu, H.; Pan, L. J.; Fan, Z. Investigations of morphology and carrier transport characteristics in high-performance PEDOT:PSS/tellurium binary composite fibers produced via continuous wet-spinning. *Adv. Funct. Mater.* **2024**, *34*, 2315677.
[68] Li, X.; Cai, K. F.; Gao, M. Y.; Du, Y.; Shen, S. Recent advances in flexible thermoelectric films and devices. *Nano Energy* **2021**, *89*, 106309.
[69] Yang, S. Q.; Qiu, P. F.; Chen, L. D.; Shi, X. Recent developments in flexible thermoelectric devices. *Small Sci.* **2021**, *1*, 2100005.
[70] Li, Y. T.; Lou, Q.; Yang, J. M.; Cai, K. F.; Liu, Y.; Lu, Y. M.; Qiu, Y.; Lu, Y.; Wang, Z. X.; Wu, M. M. et al. Exceptionally high power factor Ag_2Se/Se/polypyrrole composite films for flexible thermoelectric generators. *Adv. Funct. Mater.* **2022**, *32*, 2106902.
[71] Liu, Q. Y.; Shi, X. L.; Cao, T. Y.; Chen, W. Y.; Li, L.; Chen, Z. G. Advances and challenges in inorganic bulk-based flexible thermoelectric devices. *Prog. Mater. Sci.* **2025**, *150*, 101420.
[72] Shi, X. L.; Wang, L. J.; Lyu, W. Y.; Cao, T. Y.; Chen, W. Y.; Hu, B. X.; Chen, Z. G. Advancing flexible thermoelectrics for integrated electronics. *Chem. Soc. Rev.* **2024**, *53*, 9254–9305.
[73] Han, Y. S.; Tetik, H. Malakooti, M. H. 3D soft architectures for stretchable thermoelectric wearables with electrical self-healing and damage tolerance. *Adv. Mater.* **2024**, *36*, 2407073.
[74] Wu, B.; Lin, Y. J.; Tian, Y. Q.; Wei, W.; Xu, Y. H.; Hu, Y. H.; Li, J. M.; Li, K. R.; Hou, C. Y.; Zhang, Q. H. et al. Bioinspired wearable thermoelectric device constructed with soft-rigid assembly for personal thermal management. *Adv. Funct. Mater.* **2024**, *34*, 2402319.
[75] Cao, T. Y.; Shi, X. L.; Hu, B. X.; Yang, Q. S.; Lyu, W. Y.; Sun, S.; Yin, L. C.; Liu, Q. Y.; Chen, W. Y.; Wang, X. D. et al. Advancing Ag_2Se thin-film thermoelectrics via selenization-driven anisotropy control. *Nat. Commun.* **2025**, *16*, 1555.
[76] Luo, S. Y.; Wang, C. H.; She, Z. W.; Su, W.; Yan, Z. Y-type flexible micro thermoelectric generator using novel encapsulation structure for power enhancement. *Energy Convers. Manage*. **2024**, *301*, 117950.
[77] She, Z. W.; Wang, C. H.; Chen, X. Y.; Jian, X. D. Investigation on the structural design and performance optimization of micro Y-type thermoelectric devices utilizing flexible electrical connections of liquid metal. *Energy Convers. Manage.* **2025**, *327*, 119607.
[78] He, H. X.; Xie, Y. C.; Zuo, Q. S.; Chen, W.; Shen, Z.; Ma, Y.; Zhang, H. H.; Zhu, G. H.; Ouyang, Y. X. Optimization analysis for thermoelectric performance improvement of biconical segmented annular thermoelectric generator. *Energy* **2024**, *306*, 132397.
[79] Zaher, M. H.; Abdelsalam, M. Y.; Cotton, J. S. Non-dimensional design optimization of annular thermoelectric generators integrated in waste heat recovery applications. *Energy Convers. Manage.* **2022**, *253*, 115141.
[80] Wang, N.; Zeng, K. W.; Zheng, Y. Y.; Jiang, H. Y.; Yang, Y. B.; Zhang, Y. F.; Li, D. K.; Yu, S. H.; Ye, Q.; Peng, H. S. High-performance thermoelectric fibers from metal-backboned polymers for body-temperature wearable power devices. *Angew. Chem., Int. Ed.* **2024**, *63*, e202403415.
[81] Deng, Q.; Shi, X. L.; Li, M.; Tan, X. B.; Li, R. H.; Wang, C.; Chen, Y.; Dong, H. L.; Ang, R. Chen, Z. G. Lattice defect engineering advances n-type PbSe thermoelectrics. *Nat. Commun.* **2025**, *16*, 656.
[82] Shittu, S.; Li, G. Q.; Zhao, X. D.; Ma, X. L. Review of thermoelectric geometry and structure optimization for performance enhancement. *Appl. Energy* **2020**, *268*, 115075.
[83] Zhang, Y.; Xing, C. C.; Wang, D. Y.; Genç, A.; Lee, S. H.; Chang, C.; Li, Z.; Zheng, L. Y.; Lim, K. H.; Zhu, H. T. et al. Realizing high power factor and thermoelectric performance in band engineered $AgSbTe_2$. *Nat. Commun.* **2025**, *16*, 22.
[84] Parzer, M.; Kositz, A.; Süß, J.; Garmroudi, F.; Mori, T. Bauer, E. Enhanced thermopower by double-site substitution of Ti in $Fe_2(VAL)_{1-x}Ti_{2x}$. *Mater. Today Phys.* **2025**, *54*, 101712.
[85] Bai, S. L.; Hu, Y. X.; Zhan, S. P.; Gao, T.; Qin, B. C.; Zhao, L. D. Symmetry-breaking amplifies lone pair expression and orbital splitting for promising chain-like thermoelectrics. *J. Am. Chem. Soc.* **2025**, *147*, 27059–27067.
[86] Yang, D.; Zhang, D. L.; Ao, D. W.; Nisar, M.; Mansoor, A.; Chen, Y. X.; Li, F.; Ma, H. L.; Liang, G. X.; Zhang, X. H. et al. High thermoelectric performance of aluminum-doped cuprous selenide thin films with exceptional flexibility for wearable applications. *Nano Energy* **2023**, *117*, 108930.
[87] Wang, N.; Li, M. L.; Xiao, H. Y.; Gao, Z. B.; Liu, Z. J.; Zu, X. T.; Li, S. A.; Qiao, L. Band degeneracy enhanced thermoelectric performance in layered oxyselenides by first-principles calculations. *npj Comput. Mater.* **2021**, *7*, 18.
[88] Zheng, Z. H.; Shi, X. L.; Ao, D. W.; Liu, W. D.; Li, M.; Kou, L. Z.; Chen, Y. X.; Li, F.; Wei, M.; Liang, G. X. et al. Harvesting waste heat with flexible Bi_2Te_3 thermoelectric thin film. *Nat. Sustain.* **2023**, *6*, 180–191.
[89] Xue, Z. F.; Huang, X. G.; Lin, W. X.; Cui, W. J.; Yang, Z.; Zhao, W.; Sun, C. L.; Li, G. F.; Van Tendeloo, G.; Sang, X. H. Competing grain growth pathways in anisotropic Bi_2Te_3-based thermoelectric nanoplates. *Adv. Mater.* **2026**, *38*, e10614.
[90] Ren, Q.; Zhu, B. A.; Tang, G.; Hong, J. W. Highly deformable van der Waals chalcogenides with superior thermoelectric performance from interpretable machine learning. *Small* **2025**, *21*, 2412745.
[91] Guloy, A. M.; Ramlau, R.; Tang, Z. J.; Schnelle, W.; Baitinger, M.; Grin, Y. A guest-free germanium clathrate. *Nature* **2006**, *443*, 320–323.
[92] Shisodia, S.; Sahraoui, A. H.; Duponchel, B.; Singh, D. P.; Depriester, M. Optimization of thermoelectric parameters for quantum dot-assisted polymer nanocomposite. *Energy Adv.* **2024**, *3*, 1037–1046.
[93] Wan, D.; Bai, S. L.; Fan, S. R.; Li, B. X.; Huang, X. Y.; Zhao, H. Y.; Wang, Z. Q.; Li, Z.; Liu, Y.; Kang, P. et al. Machine learning-guided design of high-performance Mg-based thermoelectrics: Insights into thermal expansion effects. *Sci. Bull.* **2025**, *70*, 3764–3773.
[94] Gao, Z. Q.; Wei, T. R.; Deng, T. T.; Qiu, P. F.; Xu, W.; Wang, Y. C.; Chen, L. D.; Shi, X. High-throughput screening of 2D van der Waals crystals with plastic deformability. *Nat. Commun.* **2022**, *13*, 7491.
[95] Zuo, W. S.; Chen, H. Y.; Yu, Z. Y.; Fu, Y. T.; Ai, X.; Cheng, Y. X.; Jiang, M.; Wan, S.; Fu, Z. Q.; Liu, R. et al. Atomic-scale

interface strengthening unlocks efficient and durable Mg-based thermoelectric devices. *Nat. Mater.* **2025**, *24*, 735–742.
[96] Jia, B. H.; Huang, Y.; Wang, Y.; Zhou, Y. S. Y.; Zhao, X. D.; Ning, S. T.; Xu, X.; Lin, P. J.; Chen, Z. Q.; Jiang, B. B. et al. Realizing high thermoelectric performance in non-nanostructured n-type PbTe. *Energy Environ. Sci.* **2022**, *15*, 1920–1929.
[97] Hu, M. H.; Li, M.; Wang, D. Z.; Yin, L. C.; Wu, H.; Liu, W. D.; Shi, X. L.; Wang, Y. F.; Liu, Q. F.; Chen, Z. G. Revisiting cobalt dopability in GeTe system to design modulation-doped thermoelectrics. *Adv. Funct. Mater.* **2025**, *35*, 2421837.
[98] Fan, S. F.; Gao, Y. W.; Rezania, A. Thermoelectric performance and stress analysis on wearable thermoelectric generator under bending load. *Renew. Energy* **2021**, *173*, 581–595.
[99] Liu, Y. H.; Shi, Y. G.; Li, J.; Guo, X. F.; Wang, Y. C.; Xiang, Q. P.; Guo, S. M.; Ze, R. D.; Zeng, J.; Xiang, Y. C. et al. Comprehensive performance prediction and power promotion for wearable thermoelectric generator with flexible encapsulation in practical application. *Energy Convers. Manage.* **2020**, *220*, 113080.
[100] Sauerschnig, P.; Saitou, N.; Koshino, M.; Ishida, T.; Yamamoto, A. Ohta, M. Improving the long-term stability of PbTe-based thermoelectric modules: From nanostructures to packaged module architecture. *ACS Appl. Mater. Interfaces* **2024**, *16*, 46421–46432.
[101] Wang, Y. L.; Zhu, P. C.; Li, W. Q.; Liu, X. B.; Li, H.; Deng, Y.; Tan, M. High interfacial thermal stability of flexible flake-structured aluminum thin-film electrodes for Bi_2Te_3-based thermoelectric devices. *ACS Appl. Mater. Interfaces* **2022**, *14*, 12920–12926.
[102] Ren, S.; Zhang, M. H.; Ye, S. Y.; Wu, K.; Sun, Z.; Du, Y.; Fang, J. Highly efficient multi-layer flexible heatsink for wearable thermoelectric cooling. *Chem. Eng. J.* **2024**, *499*, 155914.
[103] Yusufu, E.; Sugahara, T.; Okajima, M.; Nambu, S. Suganuma, K. Effects of microstructure of Ni barrier on bonding interface diffusion behaviors of Bi–Te-based thermoelectric material. *J. Alloys Compd.* **2020**, *817*, 152731.
[104] Tian, Y.; Qin, B. C.; Li, J. N.; Zhao, L. D. Hierarchical topology optimization for minimizing SnSe-based thermoelectric interfacial depletion. *Sci. Bull.* **2025**, *70*, 3466–3469.
[105] Tan, M.; Shi, X. L.; Liu, W. D.; Jiang, Y.; Liu, S. Q.; Cao, T. Y.; Chen, W. Y.; Li, M.; Lin, T.; Deng, Y. et al. Enabling ultra-flexible inorganic thin-film-based thermoelectric devices by introducing nanoscale titanium layers. *Nat. Commun.* **2025**, *16*, 633.
[106] Sun, Y. X.; Guo, F. K.; Feng, Y.; Li, C.; Zou, Y. C.; Cheng, J. X.; Dong, X. Y.; Wu, H.; Zhang, Q.; Liu, W. S. et al. Performance boost for bismuth telluride thermoelectric generator via barrier layer based on low Young's modulus and particle sliding. *Nat. Commun.* **2023**, *14*, 8085.
[107] Li, X.; Lin, Y. X.; Cui, L.; Li, C. N.; Yang, Z. H.; Zhao, S. C.; Hao, T. L.; Wang, G. Q.; Heo, J. Y.; Yu, J. C. et al. Stretchable and lithography-compatible interconnects enabled by self-assembled nanofilms with interlocking interfaces. *ACS Appl. Mater. Interfaces* **2023**, *15*, 56233–56241.
[108] Jung, S. J.; Shin, J.; Lim, S. S.; Kwon, B.; Baek, S. H.; Kim, S. K.; Park, H. H.; Kim, J. S. Porous organic filler for high efficiency of flexible thermoelectric generator. *Nano Energy* **2021**, *81*, 105604.
[109] Wei, H. X.; Zhang, J.; Han, Y.; Xu, D. Y. Soft-covered wearable thermoelectric device for body heat harvesting and on-skin cooling. *Appl. Energy* **2022**, *326*, 119941.
[110] Kuang, N. L.; Niu, A. J.; Wang, W.; Zuo, Z. X.; Zhan, T. Z.; Wang, H. D. High performance flexible thermoelectric generator using bulk legs and integrated electrodes for human energy harvesting. *Energy Convers. Manage.* **2022**, *272*, 116337.
[111] Yang, W. K.; Liu, S.; Wang, Z. Q.; Liu, H.; Pan, C. F.; Liu, C. T.; Shen, C. Y. Bioinspired composite fiber aerogel pressure sensor for machine-learning-assisted human activity and gesture recognition. *Nano Energy* **2024**, *127*, 109799.
[112] Ding, Q. F.; Sun, X. L.; Zhu, Z.; Yan, S. J.; Xia, Z. L.; Hou, Y.; Wang, Z. Y. Long-lasting heat dissipation of flexible heat sinks for wearable thermoelectric devices. *ACS Appl. Mater. Interfaces* **2024**, *16*, 31228–31236.
[113] Wang, Y. T.; Yang, D. W.; Li, D.; Lyu, J. N.; Liu, Y. T.; Zhang, M. Q.; Gou, W. J.; Gao, Y. F.; Zhang, Z. N.; Li, C. Y. et al. Thermally enhanced substrate design for flexible thermoelectric devices via ultrasonic welding. *J. Mater. Chem. A* **2025**, *13*, 6493–6501.
[114] Li, J. H.; Yang, D. W.; Lyu, J. N.; Liu, Y. T.; Wang, Y. T.; Zhang, Z. N.; Zheng, Y.; Jia, Y. Z.; Wang, Z. A.; Pan, Z. C. et al. High efficient personal thermoregulatory device: Metallized interface layer between flexible polyimide substrate and foam copper heat sink enables thermal resistance reduction. *Appl. Mater. Today* **2024**, *37*, 102139.
[115] Liu, J. Z.; Jiang, W. K.; Zhuo, S.; Rong, Y.; Li, Y. Y.; Lu, H.; Hu, J. C.; Wang, X. Q.; Chen, W. F.; Liao, L. S. et al. Large-area radiation-modulated thermoelectric fabrics for high-performance thermal management and electricity generation. *Sci. Adv.* **2025**, *11*, eadr2158.
[116] Waktole, D. A.; Jia, B. R.; Wang, W.; Zuo, Z. X. Integration of tau-shaped fins and perforated polyimide substrate for enhanced power output in flexible thermoelectric generator for human body heat harvesting. *J. Power Sources* **2025**, *626*, 235757.
[117] Abe, H.; Takashiri, M.; Hara, S.; Arai, T.; Sasaki, N.; Tanaka, S. Performance evaluation of flexible thermoelectric generator with Bi_2Te_3 thin-film. *Appl. Therm. Eng.* **2024**, *248*, 123258.
[118] Khan, S.; Kim, J.; Roh, K.; Park, G.; Kim, W. High power density of radiative-cooled compact thermoelectric generator based on body heat harvesting. *Nano Energy* **2021**, *87*, 106180.
[119] Liang, J.; Huang, M. Z.; Zhang, X. F.; Wan, C. L.; Structural design for wearable self-powered thermoelectric modules with efficient temperature difference utilization and high normalized maximum power density. *Appl. Energy* **2022**, *327*, 120067.
[120] Zhang, Y.; Gao, J.; Zhu, S. J.; Li, J. H.; Lai, H. J.; Peng, Y.; Miao, L. Wearable thermoelectric cooler based on a two-layer hydrogel/nickel foam heatsink with two-axis flexibility. *ACS Appl. Mater. Interfaces* **2022**, *14*, 15317–15323.
[121] Zhao, X. C.; Zheng, F.; Li, Y. J.; Song, G. Y.; Zhou, Y. X.; Xiong, Y. C.; Liu, X. J. Flexible thermoelectric generator with integrated Cu foam heat sink and embedded composite substrate for enhanced body heat harvesting. *Therm. Sci. Eng. Prog.* **2025**, *63*, 103750.
[122] Rezania, A.; Yousefi, E. Nejad, A. A. Zero-cooling energy thermoelectric system by phase change material heat sink integrated with porous copper foam. *J. Energy Storage* **2023**, *59*, 106507.
[123] Mousavi, S. A. A.; Aghakhani, H.; Baghapour, B.; Lv, S. Integrating radiative cooling and thermoelectric: A comprehensive review. *Renew. Sustain. Energy Rev.* **2025**, *222*, 115946.
[124] Liu, X. H.; Zhang, W. R.; Zhang, X.; Zhou, Z. G.; Wang, C. F.; Pan, Y. M.; Hu, B.; Liu, C. T.; Pan, C. F.; Shen, C. Y. Transparent ultrahigh-molecular-weight polyethylene/MXene films with efficient UV-absorption for thermal management. *Nat. Commun.* **2024**, *15*, 3076.
[125] Hou, Y. Z.; Pan, Y. M.; Zhou, Z. Y.; Liu, C. T.; Shen, C. Y.; Liu, X. H. Review on cell structure regulation and performances improvement of porous poly(lactic acid). *Macromol. Rapid Commun.* **2023**, *44*, 2300065.
[126] Chen, C.; Xu, F. Q.; Wu, Y. B.; Li, X. L.; Xu, J. L.; Zhao, B.; He, Z.; Yang, J.; Zhang, W. Q.; Liu, J. W. Manipulating hetero-nanowire films for flexible and multifunctional thermoelectric devices. *Adv. Mater.* **2024**, *36*, 2400020.
[127] Hou, Y. Z.; Pan, Y. M.; Liu, X. H.; Ma, J.; Liu, C. T.; Shen, C. Y. A structural bioplastic metafilm for durable passive radiative cooling. *Cell Rep. Phys. Sci.* **2025**, *6*, 102664.
[128] Hou, M. T.; Chen, H.; Li, S.; Zhang, X. R.; Chen, J.; Jiang, Z. Y.; Wang, C. H.; Lai, N. C.; Ding, Y. L. A tri-mode photothermal, phase-change, and radiative-cooling film for all-day thermoelectric generation. *Adv. Mater.* **2025**, *37*, 2505601.
[129] Zhu, S. J.; Miao, L.; Gao, J.; Chen, J. L.; Zhou, Q.; Pan, Z. N.;

Zhang, Z. W.; Liang, J. S.; Yang, X. Y.; Mori, T. Wearable thermoelectric generator integrated with photothermal and radiative cooling for multi-environment compatibility. *Nano Energy* **2025**, *144*, 111328.

[130] Wu, Z. H.; Zhang, S.; Liu, Z. K.; Mu, E. Z.; Hu, Z. Y. Thermoelectric converter: Strategies from materials to device application. *Nano Energy* **2022**, *91*, 106692.

[131] Huo, W. X.; Xia, Z. Q.; Gao, Y.; Guo, R.; Huang, X. Flexible thermoelectric devices with flexible heatsinks of phase-change materials and stretchable interconnectors of semi-liquid metals. *ACS Appl. Mater. Interfaces* **2023**, *15*, 29330–29340.

[132] Wang, Y. C.; Fu, C. G.; Shi, X.; Chen, L. D.; Zhu, T. J. Inorganic thermoelectric semiconductors with room temperature plasticity. *Appl. Phys. Lett.* **2024**, *125*, 200504.

[133] Shi, X.; Chen, H. Y.; Hao, F.; Liu, R. H.; Wang, T.; Qiu, P. F.; Burkhardt, U.; Grin, Y.; Chen, L. D. Room-temperature ductile inorganic semiconductor. *Nat. Mater.* **2018**, *17*, 421–426.

[134] Ge, B. Z.; Li, R. Y.; Zhu, M. H.; Yu, Y.; Zhou, C. J. Deformation mechanisms of inorganic thermoelectric materials with plasticity. *Adv. Energy Sustain. Res.* **2024**, *5*, 2300197.

[135] Hrickova, G.; Mihok, F.; Molcanova, Z.; Ballokova, B.; Mamrilla, W.; Dzunda, R.; Lukacs, P.; Pietrikova, A.; Saksl, K. The effect of Ge doping on α-Ag_2S's thermoelectric and mechanical properties. *Inorganics* **2024**, *12*, 98.

[136] Zhang, W. T.; Yu, R.; Xiao, C. Y.; Ma, H. Q.; Li, W. J.; Zhai, P. C.; Li, G. D.; Duan, B. Pressure induced bands convergence and strength enhancement in thermoelectric semiconductor β-InSe. *J. Alloys Compd.* **2023**, *947*, 169687.

[137] Jiang, X.; Zhao, T. Q.; Wang, D. Anisotropic ductility and thermoelectricity of van der Waals GeAs. *Phys. Chem. Chem. Phys.* **2023**, *25*, 27542–27552.

[138] Zhang, J.; Zhang, T.; Zhang, H.; Wang, Z. X.; Li, C.; Wang, Z.; Li, K. W.; Huang, X. M.; Chen, M.; Chen, Z. et al. Single-crystal SnSe thermoelectric fibers via laser-induced directional crystallization: From 1D fibers to multidimensional fabrics. *Adv. Mater.* **2020**, *32*, 2002702.

[139] Deng, T. T.; Gao, Z. Q.; Qiu, P. F.; Wei, T. R.; Xiao, J.; Wang, G. S.; Chen, L. D.; Shi, X. Plastic/ductile bulk 2D van der Waals single-crystalline $SnSe_2$ for flexible thermoelectrics. *Adv. Sci.* **2022**, *9*, 2203436.

[140] Ge, B. Z.; Li, C.; Lu, W. Q.; Ye, H. L.; Li, R. Y.; He, W. K.; Wei, Z. L.; Shi, Z. Q.; Kim, D.; Zhou, C. J. et al. Dynamic phase transition leading to extraordinary plastic deformability of thermoelectric $SnSe_2$ single crystal. *Adv. Energy Mater.* **2023**, *13*, 2300965.

[141] Wang, T.; Chen, H. Y.; Qiu, P. F.; Shi, X.; Chen, L. D. Thermoelectric properties of Ag_2S superionic conductor with intrinsically low lattice thermal conductivity. *Acta Phys. Sin.* **2019**, *68*, 090201.

[142] Yuan, X. J.; Qiu, P. F.; Sun, C. Y.; Yang, S. Q.; Wu, Y.; Chen, L. D.; Shi, X. Extraordinary self-powered Y-shaped flexible film thermoelectric device for wearables. *Energy Environ. Sci.* **2024**, *17*, 4968–4976.

[143] Yang, S. Q.; Liu, J.; Zhao, X. F.; Qiu, P. F.; Shi, X. Effect of plastic hot-rolling on thermoelectric properties in $Ag_2Se_{0.65}S_{0.35}$ ductile materials. *Mater. Today Phys.* **2025**, *53*, 101707.

[144] Peng, L. M.; Yang, S. Q.; Wei, T. R.; Qiu, P. F.; Yang, J.; Zhang, Z.; Shi, X.; Chen, L. D. Phase-modulated mechanical and thermoelectric properties of $Ag_2S_{1-x}Te_x$ ductile semiconductors. *J. Materiomics* **2022**, *8*, 656–661.

[145] Liu, J.; Xing, T.; Gao, Z. Q.; Liang, J. S.; Peng, L. M.; Xiao, J.; Qiu, P. F.; Shi, X.; Chen, L. D. Enhanced thermoelectric performance in ductile Ag_2S-based materials via doping iodine. *Appl. Phys. Lett.* **2021**, *119*, 121905.

[146] Chang, Y.; Mao, W. Y.; Zhang, Y.; Dong, Z. R.; Zhang, Y. P.; Li, L. K.; Zhang, J. Y.; Luo, J. Ductile $Ag_{5.98}SSe_{0.6}Te_{1.4}$ with high room-temperature thermoelectric performance. *Small* **2025**, *21*, e02985.

[147] Liang, J. S.; Wang, T.; Qiu, P. F.; Yang, S. Q.; Ming, C.; Chen, H. Y.; Song, Q. F.; Zhao, K. P.; Wei, T. R.; Ren, D. D. et al. Flexible thermoelectrics: From silver chalcogenides to full-inorganic devices. *Energy Environ. Sci.* **2019**, *12*, 2983–2990.

[148] Pei, Y. Z.; Heinz, N. A.; Snyder, G. J. Alloying to increase the band gap for improving thermoelectric properties of Ag_2Te. *J. Mater. Chem.* **2011**, *21*, 18256–18260.

[149] Ferhat, M.; Nagao, J. Thermoelectric and transport properties of β-Ag_2Se compounds. *J. Appl. Phys.* **2000**, *88*, 813–816.

[150] He, S. Y.; Li, Y. B.; Liu, L.; Jiang, Y.; Feng, J. J.; Zhu, W.; Zhang, J. Y.; Dong, Z. R.; Deng, Y.; Luo, J. et al. Semiconductor glass with superior flexibility and high room temperature thermoelectric performance. *Sci. Adv.* **2020**, *6*, eaaz8423.

[151] Liang, J. S.; Qiu, P. F.; Zhu, Y.; Huang, H.; Gao, Z. Q.; Zhang, Z.; Shi, X.; Chen, L. D. Crystalline structure-dependent mechanical and thermoelectric performance in $Ag_2S_{1-x}S_x$ system. *Research* **2020**, *2020*, 6591981.

[152] Liang, J. S.; Liu, J.; Qiu, P. F.; Ming, C.; Zhou, Z. Y.; Gao, Z. Q.; Zhao, K. P.; Chen, L. D.; Shi, X. Modulation of the morphotropic phase boundary for high-performance ductile thermoelectric materials. *Nat. Commun.* **2023**, *14*, 8442.

[153] Wang, Y. C.; Li, A. R.; Hu, H. P.; Fu, C. G.; Zhu, T. J. Reversible room temperature brittle-plastic transition in $Ag_2Te_{0.6}S_{0.4}$ inorganic thermoelectric semiconductor. *Adv. Funct. Mater.* **2023**, *33*, 2300189.

[154] Hu, H. P.; Wang, Y. C.; Fu, C. G.; Zhao, X. B.; Zhu, T. J. Achieving metal-like malleability and ductility in $Ag_2Te_{1-x}S_x$ inorganic thermoelectric semiconductors with high mobility. *Innovation* **2022**, *3*, 100341.

[155] Liu, S. B.; Qin, Y. X.; Wen, Y.; Shi, H. N.; Qin, B. C.; Hong, T.; Gao, X.; Cao, Q.; Chang, C.; Zhao, L. D. Efforts toward the fabrication of thermoelectric cooling module based on n-type and p-type PbTe ingots. *Adv. Funct. Mater.* **2024**, *34*, 2315707.

[156] Xu, L. Q.; Hong, T.; Liu, S. B.; Wang, S. N.; Liu, D. R.; Zhou, T. H.; Xiao, Y.; Zhao, L. D. Cost-effective symmetric PbSe-based device for thermoelectric cooling. *Adv. Mater.* **2025**, *37*, 2502705.

[157] Silpawilawan, W.; Tanuslip, S. A.; Chetty, R.; Ohta, M.; Ohishi, Y.; Muta, H.; Kurosaki, K. Realizing excellent n- and p-type niobium-based half-Heusler compounds based on thermoelectric properties and high-temperature stability. *Adv. Electron. Mater.* **2020**, *6*, 2000083.

[158] Wu, H.; Shi, X. L.; Mao, Y. Q.; Li, M.; Liu, W. D.; Wang, D. Z.; Yin, L. C.; Zhu, M.; Wang, Y. F.; Duan, J. G. et al. Optimized thermoelectric performance and plasticity of ductile semiconductor $Ag_2S_{0.5}Se_{0.5}$ via dual-phase engineering. *Adv. Energy Mater.* **2023**, *13*, 2302551.

[159] Gao, Z. Q.; Yang, Q. Y.; Qiu, P. F.; Wei, T. R.; Yang, S. Q.; Xiao, J.; Chen, L. D.; Shi, X. P-type plastic inorganic thermoelectric materials. *Adv. Energy Mater.* **2021**, *11*, 2100883.

[160] Shen, K. L.; Yang, Q. Y.; Qiu, P. F.; Zhou, Z. Y.; Yang, S. Q.; Wei, T. R.; Shi, X. Ductile p-type AgCu(Se,S,Te) thermoelectric materials. *Adv. Mater.* **2024**, *36*, 2407424.

[161] Huang, B.; Li, G. D.; Duan, B.; Zhai, P. C.; Goddard III, W. A. Synergetic evolution of sacrificial bonds and strain-induced defects facilitating large deformation of the Bi_2Te_3 semiconductor. *ACS Appl. Energy Mater.* **2020**, *3*, 3042–3048.

[162] Jia, R. X.; Liu, Q. Q.; Gao, X. L.; Huang, B.; Li, G. D.; Guo, Z. G. Mechanism of bonding and defect evolution of deformed Sb_2Te_3 semiconductors under temperature effects. *J. Phys. Chem. A* **2025**, *129*, 8139–8147.

[163] Yin, S. B.; Zhao, C. H.; Zhang, B. P.; Zhao, W. B.; Zhang, C. C.; Li, L. J. Recent progress on two-dimensional van der Waals thermoelectric materials with plasticity. *J. Materiomics* **2025**, *11*, 100850.

[164] Wei, T. R.; Jin, M.; Wang, Y. C.; Chen, H. Y.; Gao, Z. Q.; Zhao, K. P.; Qiu, P. F.; Shan, Z. W.; Jiang, J.; Li, R. B. et al. Exceptional plasticity in the bulk single-crystalline van der Waals semiconductor InSe. *Science* **2020**, *369*, 542–545.

[165] Deng, T. T.; Gao, Z. Q.; Qiu, P. F.; Zhou, Z. Y.; Ming, C.; Liu, Z. P.; Li, Z.; Yang, S. Q.; Wei, T. R.; Wang, G. S. et al. High thermoelectric power factors in plastic/ductile bulk $SnSe_2$-based crystals. *Adv. Mater.* **2024**, *36*, 2304219.
[166] Liu, Z. P.; Deng, T. T.; Qiu, P. F.; Zheng, W. W.; Li, Z.; Zhou, Z. Y.; Shi, X. Mechanical and thermoelectric properties of Na-intercalated $SnSe_2$ crystals. *ACS Appl. Energy Mater.* **2024**, *7*, 8973–8980.
[167] Chen, P.; Yuan, C.; Wu, H.; Yan, Y. C.; Zhang, B.; Gong, X. N.; Liu, J.; Li, D. F.; Ding, G. Q.; Zhou, X. Y. et al. Strong phonon softening and carrier modulation for achieving superior thermoelectric performance in n-type plastic $SnSe_2$ single crystals. *J. Mater. Sci. Technol.* **2025**, *230*, 120–128.
[168] Chen, Z. G.; Shi, X. L.; Zhao, L. D.; Zou, J. High-performance SnSe thermoelectric materials: Progress and future challenge. *Prog. Mater. Sci.* **2018**, *97*, 283–346.
[169] Su, L. Z.; Wang, D. Y.; Wang, S. N.; Qin, B. C.; Wang, Y. P.; Qin, Y. X.; Jin, Y.; Chang, C.; Zhao, L. D. High thermoelectric performance realized through manipulating layered phonon-electron decoupling. *Science* **2022**, *375*, 1385–1389.
[170] Li, J. J.; Qi, Y. P.; Yang, Q.; Yue, L. Y.; Yao, C. Y.; Chen, Z. J.; Meng, S.; Xiang, D.; Cao, J. M. Femtosecond electron diffraction reveals local disorder and local anharmonicity in thermoelectric SnSe. *Adv. Mater.* **2024**, *36*, 2313742.
[171] Qin, B. C.; Kanatzidis, M. G.; Zhao, L. D. The development and impact of tin selenide on thermoelectrics. *Science* **2024**, *386*, eadp2444.
[172] Shi, W. R.; Gao, M. X.; Wei, J. P.; Gao, J. F.; Fan, C. W.; Ashalley, E.; Li, H. D.; Wang, Z. M. Tin selenide (SnSe): Growth, properties, and applications. *Adv. Sci.* **2018**, *5*, 1700602.
[173] Rongione, N. A.; Li, M.; Wu, H.; Nguyen, H. D.; Kang, J. S.; Ouyang, B. Y.; Xia, H. Y.; Hu, Y. J. High-performance solution-processable flexible SnSe nanosheet films for lower grade waste heat recovery. *Adv. Electron. Mater.* **2019**, *5*, 1800774.
[174] Morozova, N. V.; Korobeynikov, I. V.; Miyajima, N. Ovsyannikov, S. V. Giant room-temperature power factor in p-type thermoelectric SnSe under high pressure. *Adv. Sci.* **2022**, *9*, 2103720.
[175] Wang, L. Q.; Sato, N.; Peng, Y.; Chetty, R.; Kawamoto, N.; Nguyen, D. H.; Mori, T. Realizing high thermoelectric performance in n-type $Mg_3(Sb, Bi)_2$-based materials via synergetic Mo addition and Sb–Bi ratio refining. *Adv. Energy Mater.* **2023**, *13*, 2301667.
[176] Zhang, F.; Chen, C.; Yao, H. H.; Bai, F. X.; Yin, L.; Li, X. F.; Li, S.; Xue, W. H.; Wang, Y. M.; Cao, F. et al. High-performance n-type Mg_3Sb_2 towards thermoelectric application near room temperature. *Adv. Funct. Mater.* **2020**, *30*, 1906143.
[177] Mao, J.; Zhu, H. T.; Ding, Z. W.; Liu, Z. H.; Gamage, G. A.; Chen, G.; Ren, Z. F. High thermoelectric cooling performance of n-type Mg_3Bi_2-based materials. *Science* **2019**, *365*, 495–498.
[178] Li, J.; Zhang, S.; Jia, F.; Zheng, S. Q.; Shi, X. L.; Jiang, D. Q.; Wang, S. Y.; Lu, G. W.; Wu, L. M.; Chen, Z. G. Point defect engineering and machinability in n-type Mg_3Sb_2-based materials. *Mater. Today Phys.* **2020**, *15*, 100269.
[179] Zhang, Z. M.; Gao, Z. Q.; Deng, T. T.; Song, Q. F.; Chen, L. D.; Bai, S. Q. Plastic $Mg_3(Sb,Bi)_2$-based thermoelectric compounds with enhanced texture via cold-deformation. *J. Mater. Chem. A* **2024**, *12*, 8893–8899.
[180] Li, A. R.; Wang, Y. C.; Li, Y. Z.; Yang, X. L.; Nan, P. F.; Liu, K.; Ge, B. H.; Fu, C. G.; Zhu, T. J. High performance magnesium-based plastic semiconductors for flexible thermoelectrics. *Nat. Commun.* **2024**, *15*, 5108.
[181] Hu, M. Y.; Yang, J. M.; Wang, Y.; Xia, J. C.; Gan, Q.; Yang, S. H.; Xu, J. P.; Liu, S. L.; Yin, W.; Jia, B. H. et al. Helical dislocation-driven plasticity and flexible high-performance thermoelectric generator in α-Mg_3Bi_2 single crystals. *Nat. Commun.* **2025**, *16*, 128.
[182] He, Z. P.; Sun, B. N.; Lu, H.; Sun, X. D.; Xu, Z. S.; Liang, Y. G.; Lu, Q. C.; Yu, Y.; Hu, K. Y.; Poddar, S. et al. Focus-tunable real-time imaging system based on ultrathin perovskite curved image sensor with hierarchical mesh design. *Sci. Adv.* **2025**, *11*, eadw7826.
[183] Hao, X.; Wang, J.; Wang, H. High power output density organic thermoelectric devices for practical applications in waste heat harvesting. *Chem. Soc. Rev.* **2025**, *54*, 1957–1985.
[184] He, H.; Zhong, Z. T.; Fan, P.; Zhao, W. C.; Yuan, D. F. Regulating optoelectronic and thermoelectric properties of organic semiconductors by heavy atom effects. *Small* **2025**, *21*, 2405156.
[185] Khelifi, W.; Luscombe, C. K. Recent developments in indacenodithiophene and indacenodithienothiophene-based donor-acceptor conjugated polymers: From design to device performance in organic electronics. *Prog. Polym. Sci.* **2024**, *151*, 101804.
[186] Paleti, S. H. K.; Kim, Y.; Kimpel, J.; Craighero, M.; Haraguchi, S.; Müller, C. Impact of doping on the mechanical properties of conjugated polymers. *Chem. Soc. Rev.* **2024**, *53*, 1702–1729.
[187] Abbasi, M. S.; Sultana, R.; Ahmed, I.; Adnan, M.; Shah, U. A.; Irshad, M. S.; Vu, H. N.; Do, L. T.; Thi Vu, H. H.; Pham, T. D. et al. Contemporary advances in organic thermoelectric materials: Fundamentals, properties, optimization strategies, and applications. *Renew. Sustain. Energy Rev.* **2024**, *200*, 114579.
[188] Nayak, R.; Shetty, P.; M, S.; Rao, A.; K V, S.; Wagle, S.; Nayak, S.; Kamath, V.; Shetty, N. Saquib, M. Formulation and optimization of copper selenide/PANI hybrid screen printing ink for enhancing the power factor of flexible thermoelectric generator: A synergetic approach. *Ceram. Int.* **2024**, *50*, 25779–25791.
[189] Yang, J. J.; Jiang, Q. L.; Zhang, J.; Xu, J. K.; Liu, J.; Liu, P. P.; Liu, G. Q.; Wang, Y. Y.; Jiang, F. X. *In situ* fabricated PEDOT:PSS:PANI with enhanced thermoelectric performance by organic solvent and CSA treatment. *Synthetic Met.* **2020**, *269*, 116546.
[190] Ji, D. Z.; Li, B. S.; Raj, B. T.; Li, X.; Zhang, D. W.; Rezeq, M.; Cantwell, W.; Zheng, L. X. *In situ* surface polymerization of PANI/SWCNT bilayer film: Effective composite for improving seebeck coefficient and power factor. *Adv. Mater. Interfaces* **2025**, *12*, 2400566.
[191] Wen, N. X.; Zuo, X. Q.; Zhou, J. J.; Sun, C.; Chen, C.; Jiang, D. Y.; Xu, H.; Wang, W.; Pan, L. J.; Fan, Z. Boosting thermoelectric performance of wet-spun PEDOT:PSS-based organic/inorganic composite fibers via a dual-interfacial engineering approach. *Small* **2025**, *21*, 2500866.
[192] Kumar, M.; Meena, D.; Singh, M. Meena, R. Impact of Ag–ZnO integration on charge transportation in PANI: An enhanced polymer-based thermoelectric generator. *Mater. Sci. Eng. B* **2025**, *322*, 118648.
[193] Debnath, A.; Das, J.; Deb, K.; Bhowmik, K. L.; Saha, B. Camphor sulfonic acid incorporation in SnO_2/polyaniline nanocomposites for improved thermoelectric energy conversion. *Sustain. Energy Fuels* **2022**, *6*, 1332–1344.
[194] Debnath, A.; Deb, K.; Sarkar, K.; Saha, B. Improved thermoelectric performance in TiO_2 incorporated polyaniline: A polymer-based hybrid material for thermoelectric generators. *J. Electron. Mater.* **2020**, *49*, 5028–5036.
[195] Beyrami, H.; Nazarzadeh Zare, E.; Golshan, M.; Kucińska-Lipka, J.; Zare, I.; Kang, N.; Saeb, M. R.; Salami-Kalajahi, M.; Kang, H.; Makvandi, P. Engineered intrinsically conducting polymer/MXene smart platforms: Fabrication, clinical translatability, and biomedical applications. *Coordin. Chem. Rev.* **2025**, *540*, 216802.
[196] Zhong, K. J.; Xiang, J.; Liu, Y.; Song, C. L.; Mu, Y. T.; Yao, T.; Zhao, K.; Gu, T. F.; Jia, P. X.; Zhang, W. Y. Fabrication of a high strength, swelling resistance, and conductive hydrogel for flexible underwater sensor via ketalization. *Chem. Eng. J.* **2025**, *511*, 161885.
[197] Masoumi, S.; O'Shaughnessy, S.; Pakdel, A. Organic-based flexible thermoelectric generators: From materials to devices. *Nano Energy* **2022**, *92*, 106774.
[198] Qi, G. J.; Huang, L. Y.; Wang, H. L. Highly conductive free standing polypyrrole films prepared by freezing interfacial polymerization. *Chem. Commun.* **2012**, *48*, 8246–8248.
[199] Al-Otaibi, A.; Attar, A.; Baghdadi, N.; Salah, N.; Zoromba, M. S.; Abdel-Aziz, M. H. Ternary composites of PPy/MWCNTs/metals

hydroxide for thermoelectric applications. *J. Mater. Sci. Mater. Electron.* **2024**, *35*, 924.

[200] Wang, Y.; Jin, L. G.; Wang, C. F.; Liu, H. P.; Mao, C. Y.; Liu, X. M.; Li, Z. Y.; Zhu, S. L.; Jiang, H.; Cui, Z. D. et al. Microwave-excited thermoelectric catalysis of organic-inorganic nanohybrid for highly effective treatment of *Staphylococcus aureus*-infected osteomyelitis. *Small* **2025**, *21*, 2500915.

[201] Bai, T. B.; Liu, Y. L.; Li, T. M.; Li, P. L.; Song, N. X.; Cui, Y. W.; Zhou, L.; Zheng, Y. A. Hierarchical wood evaporator with hydrogen-bond modulation for anti-fouling desalination and synchronous waste-heat thermoelectric generation. *Chem. Eng. J.* **2025**, *525*, 170315.

[202] Long, Y. T.; Li, X.; Li, Y.; Wang, L. K.; Zhu, H. Y.; Shi, G. Hygroscopic assisted solar photo-thermal-electric conversion system for all-day power generation and daytime water collection. *Chem. Eng. J.* **2024**, *494*, 152615.

[203] Dong, X. Y.; Zhou, X. M.; Liu, Y.; Xiong, S. X.; Cheng, J. Y.; Jiang, Y. Y.; Zhou, Y. H. Two-in-one alcohol-processed PEDOT electrodes produced by solvent exchange for organic solar cells. *Energy Environ. Sci.* **2023**, *16*, 1511–1519.

[204] Ma, X. L.; Wang, C. F.; Wei, R. L.; He, J. Q.; Li, J.; Liu, X. H.; Huang, F. C.; Ge, S. P.; Tao, J.; Yuan, Z. Q. et al. Bimodal tactile sensor without signal fusion for user-interactive applications. *ACS Nano* **2022**, *16*, 2789–2797.

[205] Zhang, J. J.; Ye, C. C.; Wei, G. W.; Guo, L.; Cai, Y. H.; Li, Z.; Wu, X. Z.; Sun, F. Y.; Li, Q. K.; Wang, Y. P. et al. Polaron interfacial entropy as a route to high thermoelectric performance in DAE-doped PEDOT:PSS films. *Natl. Sci. Rev.* **2024**, *11*, nwae009.

[206] Zhang, M.; Cao, X. Y.; Wen, M.; Chen, C. L.; Wen, Q. C.; Fu, Q.; Deng, H. Highly electrical conductive PEDOT:PSS/SWCNT flexible thermoelectric films fabricated by a high-velocity non-solvent turbulent secondary doping approach. *ACS Appl. Mater. Interfaces* **2023**, *15*, 10947–10957.

[207] Du, M. Z.; Wen, Y.; Chen, Z. J.; Xu, Y. C.; Qin, J.; Cheng, H. L.; Du, Y.; Zhang, K.; Shin, S.; Ouyang, J. Y. A polymer film with very high seebeck coefficient and overall thermoelectric properties by secondary doping, dedoping engineering and ionic energy filtering. *Adv. Funct. Mater.* **2025**, *35*, 2411815.

[208] Wu, T.; Shi, X. L.; Liu, W. D.; Li, M.; Yue, F.; Huang, P.; Liu, Q. F.; Chen, Z. G. High thermoelectric performance and flexibility in rationally treated PEDOT:PSS fiber bundles. *Adv. Fiber Mater.* **2024**, *6*, 607–618.

[209] He, X. Y.; Wu, C. L.; Zhang, T. W.; Chen, Z. J.; Wang, L. M.; Ouyang, J. Y. Ultrahigh thermoelectric properties of PEDOT:PSS films by dedoping and π-π overlapping with 4-(1,3-dimethyl-2,3-dihydro-1h-benzoimidazol-2-yl)phenyl)dimethylamine (N-DMBI). *Adv. Funct. Mater.* **2025**, *35*, 2506872.

[210] Shi, S. C.; Hsieh, Y. C.; Rahmadiawan, D. Cellulose nanocrystal and self-assembling lignin enhanced the PEDOT/PSS/PVA composite on mechanical and self-powered wearable properties. *ACS Omega* **2025**, *10*, 14666–14675.

[211] Deng, Y. Y.; Shi, X. L.; Wu, T.; Yue, Y. C.; Liu, W. D.; Li, M.; Yue, F.; Huang, P.; Liu, Q. F.; Chen, Z. G. Optimization of wet-spun PEDOT:PSS fibers for thermoelectric applications through innovative triple post-treatments. *Adv. Fiber Mater.* **2024**, *6*, 1616–1628.

[212] Xu, Y. C.; Sun, W.; Chen, Z. J.; Ouyang, J. Y. PEDOT:PSS films with very high thermoelectric properties through water-swollen assisted reduction with a tetrakis(dimethylamino)ethylene solution. *Adv. Funct. Mater*. **2024**, *34*, 2410929.

[213] Mardi, S.; Pea, M.; Notargiacomo, A.; Yaghoobi Nia, N. ; di Carlo, A.; Reale, A. The molecular weight dependence of thermoelectric properties of poly (3-hexylthiophene). *Materials* **2020**, *13*, 1404.

[214] Liao, Z. X.; Wang, S. C.; Gao, C. M.; Wang, L. Combining chemical doping and thermal annealing to optimize the thermoelectric performance of the poly(3-hexylthiophene). *Compos. Commun.* **2022**, *34*, 101255.

[215] Kim, B. J.; Chung, S.; Sim, S.; Lee, H.; Lee, J.; Cho, K. Boosting thermoelectric performance of doped conjugated polymers through π-π aggregates-induced percolation pathway. *Nano Energy* **2025**, *146*, 111547.

[216] Biswas, P.; Kong, L. C.; Tian, Z. T. Donor-acceptor conjugated polymers as high-mobility semiconductors: Prospects for organic thermoelectrics. *Nanoscale* **2025**, *17*, 23896–23914.

[217] Lee, T. S.; Lee, S. B.; Choi, D. Y.; Suh, E. H.; An, T. K.; Jeong, Y. J.; Jang, J.; Kim, Y. H. Doping and thermoelectric behaviors of donor-acceptor polymers with extended planar backbone. *Macromol. Res.* **2021**, *29*, 887–894.

[218] Ullah, A.; Nadeem, M.; Hasnain, M.; Adamu, M.; Fan, N.; Afzal, T.; Zhang, X. T.; Jiao, F. Enhanced thermoelectric performance of triisopropylsilylethynyl benzo[1,2-b:4,5-b']dithiophene-based donor-acceptor copolymers via doping improved charge transport. *J. Power Sources* **2025**, *657*, 238167.

[219] Yang, C. Y.; Jin, W. L.; Wang, J.; Ding, Y. F.; Nong, S. Y.; Shi, K.; Lu, Y.; Dai, Y. Z.; Zhuang, F. D.; Lei, T. et al. Enhancing the n-type conductivity and thermoelectric performance of donor-acceptor copolymers through donor engineering. *Adv. Mater.* **2018**, *30*, 1802850.

[220] Feng, K.; Yang, W. L.; Jeong, S. Y.; Ma, S. X.; Li, Y. C.; Wang, J. W.; Wang, Y. M.; Woo, H. Y.; Chan, P. K. L.; Wang, G. et al. Cyano-functionalized fused bithiophene imide dimer-based n-type polymers for high-performance organic thermoelectrics. *Adv. Mater.* **2023**, *35*, 2210847.

[221] Zhang, Y. Y.; Deng, L. H.; Cho, Y.; Lee, J.; Shibayama, N.; Zhang, Z. L.; Wang, C.; Hu, Z. Y.; Wang, J.; Wu, F. Y. et al. Revealing the enhanced thermoelectric properties of controllably doped donor-acceptor copolymer: The impact of regioregularity. *Small* **2023**, *19*, 2206233.

[222] Zhu, Z. H.; Li, K. C.; Hao, X.; Dai, X.; Wang, J.; Yin, F. F.; Wang, H. Rollable single-piece thermoelectric generators at cryogenic temperature fabricated with high-performance CNT films achieved by doping modulation. *Adv. Sci.* **2026**, *13*, e15688.

[223] Lin, C. Y.; Chang, J. W.; Lin, M. H.; Wu, K. C.; Hong, S. H.; Lin, J. M.; Kung, C. W.; Liu, C. L. Carbon nanotube/two-dimensional metal-organic framework composites with enhanced thermoelectric performances for thermoelectric generators. *Chem. Eng. J.* **2025**, *521*, 166861.

[224] Zhao, X.; Chen, Z. H.; Zhuo, H.; Hu, Y. J.; Shi, G.; Wang, B.; Lai, H. H.; Araby, S.; Han, W. J.; Peng, X. W. et al. Thermoelectric generator based on anisotropic wood aerogel for low-grade heat energy harvesting. *J. Mater. Sci. Technol.* **2022**, *120*, 150–158.

[225] Jang, J. Kee, S. Highly stretchable organic thermoelectrics based on dispersion-stable and dry-transferable single-walled carbon nanotubes. *Carbon* **2024**, *230*, 119590.

[226] Zhang, H.; Li, H.; Wang, W. B.; Li, P. C.; Liu, S. Q.; Yang, M.; He, C. B. Biomass lignin as dispersion to substantially enhance carbon nanotubes thermoelectric converter for energy harvesting. *Carbon* **2024**, *229*, 119489.

[227] Rani, R.; Sehrawat, M.; Verma, A. K.; Rani, M.; Gahtori, B.; Kumar, P.; Dhakate, S. R.; Singh, B. P. Surfactant-mediated control of polyethylenimine dopant for enhanced thermoelectric performance of carbon nanotube buckypaper for varied device configurations. *ACS Appl. Energy Mater.* **2024**, *7*, 6996–7005.

[228] Bark, H.; Thangavel, G.; Liu, R. J.; Chua, D. H. C.; Lee, P. S. Effective surface modification of 2D MXene toward thermal energy conversion and management. *Small Methods* **2023**, *7*, 2300077.

[229] Wan, Z. L.; Liu, X. F.; Liu, C.; Liu, C. C.; Liu, P. P.; Tan, R. R.; Zhang, Q.; Chen, Z. H.; Xu, J. K.; Jiang, F. X. Oxygen vacancy-tailored n-type MXenes for efficient thermoelectric energy harvesting. *Small* **2025**, *21*, 2410854.

[230] Ji, Y. R.; Zhang, X. F.; Ai, W.; He, Z. X.; Lou, S. Z.; Tang, Z.; Hang, F. L.; Liu, Z. G.; Ou, Y. X.; Hu, X. H. et al. Intercalation-deintercalation engineering of van der Waals stacked Mxene films for wearable thermoelectrics and sensing. *Chem. Eng. J.* **2025**, *512*, 162603.

[231] Wang, Z. W.; Chen, M. R.; Cao, Z. N.; Liang, J.; Liu, Z. G.; Xuan, Y. X.; Pan, L.; Razeeb, K. M.; Wang, Y. F.; Wan, C. L. et al.

MXene nanosheet/organics superlattice for flexible thermoelectrics. *ACS Appl. Nano Mater.* **2022**, *5*, 16872–16883.
[232] Yang, Z. Y.; Huo, S. D.; Zhang, Z.; Meng, F. Y.; Liu, B. Y.; Wang, Y.; Ma, Y. X.; Wang, Z. Y.; Xu, J. X.; Tian, Q. J. et al. High-precision multibit opto-electronic synapses based on ReS_2/h-BN/graphene heterostructure for energy-efficient and high-accuracy neuromorphic computing. *Adv. Funct. Mater.* **2025**, *35*, 2509119.
[233] Li, X.; Wu, G. C.; Pan, C. F.; Bao, R. R. Recent progress in flexible sensors based on 2D materials. *J. Semicond.* **2025**, *46*, 011607.
[234] Wei, T. Y.; Li, H.; Fu, Y. M.; Zheng, X. X.; Huang, L.; Song, A. M. A graphene-nanoribbon-based thermoelectric generator. *Carbon* **2023**, *210*, 118053.
[235] Lee, W.; Lim, G.; Ko, S. H. Significant thermoelectric conversion efficiency enhancement of single layer graphene with substitutional silicon dopants. *Nano Energy* **2021**, *87*, 106188.
[236] Novak, T. G.; Kim, J.; Kim, J.; Tiwari, A. P.; Shin, H.; Song, J. Y.; Jeon, S. Complementary n-type and p-type graphene films for high power factor thermoelectric generators. *Adv. Funct. Mater.* **2020**, *30*, 2001760.
[237] Wu, T.; Shi, X. L.; Deng, Y. Y.; Liu, Y. M.; Zhu, M.; Liu, W. D.; Li, M.; Yue, F.; Huang, P.; Chen, Z. G. et al. Incorporating graphene quantum dots boosts thermoelectric performance of PEDOT:PSS films. *Chem. Eng. J.* **2025**, *506*, 160219.
[238] Li, P. G.; Shi, J. G.; Wu, X. L.; Li, J. Q.; Hu, L. P.; Liu, F. S.; Li, Y.; Ao, W. Q.; Zhang, C. H. Interfacial engineering of solution-processed Bi_2Te_3-based thermoelectric nanocomposites via graphene addition and liquid-phase-sintering process. *Chem. Eng. J.* **2022**, *440*, 135882.
[239] Zheng, J. Q.; Wen, Y.; Wang, S. N.; Li, Y. C.; Wang, S. Q.; Zhao, Z.; Liu, S.; Liu, S. B.; Gao, X.; Zhao, L. D. Microstructure optimization in the shear-exfoliated $Bi_6Cu_2Se_4O_6$ through introducing reduced graphene oxide leads to wide-ranged thermoelectric performance. *Adv. Funct. Mater.* **2024**, *34*, 2401735.
[240] Zhang, M. C.; Li, J. J.; Liu, Y.; Liu, Y. X.; Huang, C. J.; Liu, R. H.; Wei, P.; Zhao, W. Y.; Xie, W. J.; Weidenkaff, A. et al. Screen printing high-performance free-standing Ag_2Se/carbon composite film for flexible thermoelectric converters. *Nano Energy* **2025**, *138*, 110836.
[241] Cao, T. Y.; Shi, X. L.; Hu, B. X.; Liu, S. Q.; Lyu, W. Y.; Li, M.; Wang, S.; Chen, W. Y.; Liu, W. D.; Moshwan, R. et al. Indium-doping advances high-performance flexible Ag_2Se thin films. *Adv. Sci.* **2025**, *12*, 2500364.
[242] Zhu, P. C.; Shi, C. Q.; Wang, Y. L.; Wang, Y. L.; Yu, Y. D.; Wang, Y.; Deng, Y.; Xiao, J. L. Recyclable, healable, and stretchable high-power thermoelectric generator. *Adv. Energy Mater.* **2021**, *11*, 2100920.
[243] Kang, M.; Qu, R. X.; Sun, X. W.; Yan, Y. D.; Ma, Z. J.; Wang, H.; Yan, K. F.; Zhang, W. F.; Deng, Y. Self-powered temperature electronic skin based on island-bridge structure and Bi–Te micro-thermoelectric generator for distributed mini-region sensing. *Adv. Mater.* **2023**, *35*, 2309629.
[244] Xu, S. D.; Horta, S.; Lawal, A.; Maji, K.; Lorion, M.; Ibáñez, M. Interfacial bonding enhances thermoelectric cooling in 3D-printed materials. *Science* **2025**, *387*, 845–850.
[245] Yang, D.; Shi, X. L.; Li, M.; Nisar, M.; Mansoor, A.; Chen, S.; Chen, Y. X.; Li, F.; Ma, H. L.; Liang, G. X. et al. Flexible power generators by Ag_2Se thin films with record-high thermoelectric performance. *Nat. Commun.* **2024**, *15*, 923.
[246] Sun, X. L.; Hou, Y.; Zhu, Z.; Zhu, B.; Ding, Q. F.; Zhou, W. J.; Yan, S. J.; Xia, Z. L.; Liu, Y.; Hou, Y. M. et al. Modular assembly of self-healing flexible thermoelectric devices with integrated cooling and heating capabilities. *Nat. Commun.* **2025**, *16*, 4220.
[247] Burton, M. R.; Liu, T. J.; McGettrick, J.; Mehraban, S.; Baker, J.; Pockett, A.; Watson, T.; Fenwick, O.; Carnie, M. J. Thin film tin selenide (SnSe) thermoelectric generators exhibiting ultralow thermal conductivity. *Adv. Mater.* **2018**, *30*, 1801357.
[248] Shokralla, E. A.; Ashfaq, A.; Alqurashi, H.; Alharbe, L. G.; Hanna, E. G.; Fahmy, M. A.; Macadangdang, R. R.; Alrefaee, S. H.; Almufarij, R. S.; Abd-Elwahed, A. R. Improvement of structural, morphological and thermoelectric power factor of thermally evaporated Sr doped SnTe film. *Ceram. Int.* **2024**, *50*, 34467–34471.
[249] Yang, D.; Chen, N.; Nisar, M.; Zhang, Z. L.; Li, F.; Danish, M. H.; Ma, H. L.; Liang, G. X.; Zhang, X. H.; Chen, Y. X. et al. Ultra-flexible organic-inorganic hybrid Bi_2Te_3 thin films for thermoelectric generators. *Acta Mater.* **2025**, *290*, 120971.
[250] Zhang, W. H.; Wang, C. B.; Jin, J. J.; Wang, L.; Wang, F.; Zhao, Z. X.; Zhang, Z. H.; Ma, J. C. Photoelectric coupling enhanced absorbers for boosting thermoelectric generation. *J. Mater. Sci. Technol.* **2026**, *249*, 99–108.
[251] Liu, Y.; Mu, E. Z.; Wu, Z. H.; Che, Z. X.; Sun, F. Y.; Fu, X. C.; Wang, F. F.; Wang, X. W.; Hu, Z. Y. Ultrathin mems thermoelectric generator with Bi_2Te_3/(Pt, Au) multilayers and Sb_2Te_3 legs. *Nano Converg.* **2020**, *7*, 8.
[252] Zhang, J.; Zhang, W. H.; Wei, H. X.; Tang, J. Q.; Li, D. Y.; Xu, D. Y. Flexible micro thermoelectric generators with high power density and light weight. *Nano Energy* **2023**, *105*, 108023.
[253] Zhang, L.; Wang, H. Y.; Zhang, B.; Chen, Y.; Zhou, T. H.; Lin, X. Y.; Lu, Z. S.; Lu, X.; Han, G.; Wang, G. Y. et al. Enhanced thermoelectric performance of screen-printed Bi_2Te_3 flexible films and generators through controlled thermal processing. *ACS Appl. Energy Mater.* **2025**, *8*, 14813–14821.
[254] Chen, W. Y.; Shi, X. L.; Li, M.; Liu, T.; Mao, Y. Q.; Liu, Q. Y.; Dargusch, M.; Zou, J.; Lu, G. Q.; Chen, Z. G. Nanobinders advance screen-printed flexible thermoelectrics. *Science* **2024**, *386*, 1265–1271.
[255] Lee, D.; Park, W.; Kang, Y. A.; Lim, H. T.; Park, S.; Mun, Y.; Kim, J.; Jang, K. S. Substrate-free thermoelectric 25 μm-thick Ag_2Se films with high flexibility and in-plane ZT of 0.5 at room temperature. *ACS Appl. Mater. Interfaces* **2023**, *15*, 3047–3053.
[256] Liang, J.; Zhang, X. F.; Wan, C. L. From brittle to ductile: A scalable and tailorable all-inorganic semiconductor foil through a rolling process toward flexible thermoelectric modules. *ACS Appl. Mater. Interfaces* **2022**, *14*, 52017–52024.
[257] Gao, Z. Q.; Yang, S. Q.; Ma, Y. P.; Wei, T. R.; Chen, X. H.; Zheng, W. W.; Qiu, P. F.; Zeng, X. Q.; Chen, L. D.; Shi, X. Warm metalworking for plastic manufacturing in brittle semiconductors. *Nat. Mater.* **2025**, *24*, 1538–1544.
[258] Paul, B.; Lu, J.; Eklund, P. Nanostructural tailoring to induce flexibility in thermoelectric $Ca_3Co_4O_9$ thin films. *ACS Appl. Mater. Interfaces* **2017**, *9*, 25308–25316.
[259] Fu, L. W.; Park, K.; Kim, S. I.; Kim, B.; Song, H. Y.; Choi, W.; Kim, Y. M.; Hwang, J. Y.; Lee, K. H.; Kim, S. W. High-performance bismuth antimony telluride thermoelectric membrane on curved and flexible supports. *ACS Energy Lett.* **2021**, *6*, 2378–2385.
[260] Zhu, Q.; Wang, S. X.; Wang, X. Z.; Suwardi, A.; Chua, M. H.; Soo, X. Y. D.; Xu, J. W. Bottom-up engineering strategies for high-performance thermoelectric materials. *Nanomicro Lett.* **2021**, *13*, 119.
[261] Sojo-Gordillo, J. M.; Sierra, C. D.; Gadea Diez, G.; Segura-Ruiz, J.; Bonino, V.; Nuñez Eroles, M.; Gonzalez-Rosillo, J. C.; Estrada-Wiese, D.; Salleras, M.; Fonseca, L. et al. Superior thermoelectric performance of SiGe nanowires epitaxially integrated into thermal micro-harvesters. *Small* **2023**, *19*, 2206399.
[262] Jia, X. M.; Chang, C.; Zhao, L. D. Grain boundary engineering in bottom-up synthesized thermoelectric nanocomposites. *Chem. Mater.* **2025**, *37*, 6443–6449.
[263] Sun, X. Y.; Li, J. Y.; Zhao, P.; Qi, R.; Liu, Y. C.; Ji, H. N.; Li, H. D.; Niu, X. B.; Wang, Z. M. Van der Waals epitaxy of $(Bi_{1-x}In_x)_2Te_3$ solid solutions with a broad operating temperature range for thin-film thermoelectrics. *Appl. Phys. Lett.* **2025**, *127*, 011603.
[264] Yang, S. H.; Liu, M. Y.; Yue, S. N.; Liu, P. P.; Lin, H. T.; Gao, T. T.; Huang, X. Unveiling controlled growth of single-crystalline

layered Sb_2Te_3 via van der Waals epitaxy for visible-light photodetectors and optoelectronic synapses. *Adv. Funct. Mater.* **2025**, *35*, 2419319.

[265] Kim, E. S.; Hwang, J. Y.; Lee, K. H.; Ohta, H.; Lee, Y. H.; Kim, S. W. Graphene substrate for van der Waals epitaxy of layer-structured bismuth antimony telluride thermoelectric film. *Adv. Mater.* **2017**, *29*, 1604899.

[266] Qu, S. Y.; Ming, C.; Qiu, P. F.; Xu, K. Q.; Xu, Q.; Yao, Q.; Lu, P.; Zeng, H. R.; Shi, X.; Chen, L. D. High-performance n-type Ta_4SiTe_4/polyvinylidene fluoride (PVDF)/graphdiyne organic-inorganic flexible thermoelectric composites. *Energy Environ. Sci.* **2021**, *14*, 6586–6594.

[267] Hu, Q. X.; Liu, W. D.; Zhang, L.; Gao, H.; Wang, D. Z.; Wu, T.; Shi, X. L.; Li, M.; Liu, Q. F.; Yang, Y. L. et al. Carrier separation boosts thermoelectric performance of flexible n-type Ag_2Se-based films. *Adv. Energy Mater.* **2024**, *14*, 2401890.

[268] Tu, L. J.; Wang, J. W.; Wu, Z. A.; Li, J. F.; Yang, W. L.; Liu, B.; Wu, S. Q.; Xia, X. M.; Wang, Y. M.; Woo, H. Y. et al. Cyano-functionalized pyrazine: A structurally simple and easily accessible electron-deficient building block for n-type organic thermoelectric polymers. *Angew. Chem., Int. Ed.* **2024**, *63*, e202319658.

[269] Gao, Y. X.; Ke, Y. Z.; Wang, T. Z.; Shi, Y. B.; Wang, C.; Ding, S. S.; Wang, Y. P.; Deng, Y. F.; Hu, W. P.; Geng, Y. H. An n-type conjugated polymer with low crystallinity for high-performance organic thermoelectrics. *Angew. Chem., Int. Ed.* **2024**, *63*, e202402642.

[270] Liu, C.; Liang, H. H.; Xie, R. Z.; Zhou, Q. F.; Qi, M.; Yang, C. Q.; Gu, X. D.; Wang, Y. F.; Zhang, G. X.; Li, J. L. et al. A three-in-one hybrid strategy for high-performance semiconducting polymers processed from anisole. *Adv. Sci.* **2024**, *11*, 2401345.

[271] Zhang, Q.; Sun, H.D.; Zhu, M. F. Structure design for high performance n-type polymer thermoelectric materials. *Chin. Phys. B* **2022**, *31*, 028506.

[272] Li, H. P.; Gao, C. Y.; Fan, X. H.; Li, Y. F.; Chen, Y.; Yang, L. M. Molecular conformational modulation via intramolecular non-covalent interactions enables a good balance of crystallinity and doping efficiency in DPP-based polymer thermoelectrics. *Synth. Met.* **2025**, *314*, 117948.

[273] Sun, W. P.; Gámez-Valenzuela, S.; Zhang, X. G.; Lee, J. W.; Zhong, Z. C.; Wang, P.; Ma, S. X.; Wang, H. Q.; Kim, B. J.; Guo, X. G. A simple quinoid building block for polymer semiconductors with tunable polarity and high n-type thermoelectric performance. *Angew. Chem., Int. Ed.* **2025**, *64*, e202501196.

[274] Peng, X. T.; Ye, G.; Zhang, L. L.; Kuang, Y. Z.; Shao, S. Y.; Liu, J. Enhancing charge transport performance of n-doped conjugated polymers by customizing amphipathic side chains. *Macromolecules* **2024**, *57*, 7156–7164.

[275] Zhong, F.; Zheng, Y. Y.; Song, J.; Chen, L. D.; Li, H. Side-chain-free benzothiadiazole-based thermoelectric polymers with enhanced electrical conductivity and thermal stability by acid cleavage. *Adv. Funct. Mater.* **2025**, *35*, 2507113.

[276] Ye, G.; Kuang, Y. Z.; Ma, M. Y.; Peng, X. T.; Liu, J. Fluorinated alkyl chains terminated polar glycol ether side chain for n-type organic thermoelectrics with enhanced performance and air stability. *Adv. Sci.* **2025**, *12*, 2500571.

[277] Cho, S. H.; Ha, J. W.; Song, C. E.; Kang, Y. H.; Han, M.; Lee, S.; Park, B. Significance of the relationship between the alkyl side-chain lengths of diketopyrrolopyrrole-based polymers and their thermoelectric properties. *Chem. Eng. J.* **2025**, *508*, 160823.

[278] Guchait, S.; Oummouch, S.; Durand, P.; Kamatham, N.; Jismy, B.; Herrmann, L.; Mery, S.; Leclerc, N.; Brinkmann, M. Impact of side chain chemical structure on doping and thermoelectric properties of oriented PBTTT thin films. *Small* **2025**, *21*, 2410073.

[279] Li, J. L.; Deng, X. Y.; Chen, J. P.; Fu, P. X.; Tian, S. Y.; Wang, Y. F.; Gu, X. D.; Lei, T. Cationic conjugated polymers with enhanced doped-state planarity for *n*-type organic thermoelectrics. *CCS Chem.* **2025**, *7*, 1449–1458.

[280] Wu, F. Y.; Zhu, Q.; Wang, J.; Yang, W. L.; Jeong, S. Y.; Du, L.; Fan, Z. P.; Woo, H. Y.; Guo, X. G.; Chen, L. et al. Conformationally locked polythiophene processed by room-temperature blade coating enables a breakthrough of the power factor. *J. Mater. Chem. A* **2023**, *11*, 26774–26783.

[281] Ichikawa, S.; Toshima, N. Improvement of thermoelectric properties of composite films of PEDOT-PSS with xylitol by means of stretching and solvent treatment. *Polym. J.* **2015**, *47*, 522–526.

[282] Hynynen, J.; Järsvall, E.; Kroon, R.; Zhang, Y. D.; Barlow, S.; Marder, S. R.; Kemerink, M.; Lund, A.; Müller, C. Enhanced thermoelectric power factor of tensile drawn poly(3-hexylthiophene). *ACS Macro Lett.* **2019**, *8*, 70–76.

[283] Chen, C.; Ma, H. B.; Lu, K. Q.; Zhang, X. X.; Yue, B. Q.; Song, C.; Huang, P. C.; Cheng, H. F.; Lin, Y. Boosting thermoelectric performance of semicrystalline conducting polymers by simply adding nucleating agent. *Adv. Mater.* **2025**, *37*, 2417594.

[284] Culebras, M.; Byun, Y. Y.; Jang, J.; Serafin, A.; Collins, M. N.; Park, Y. T.; Cho, C. Nanostructured PEDOT-based multilayer thin films with high thermoelectric performances. *Appl. Surf. Sci.* **2023**, *615*, 156432.

[285] Wang, R. M.; Zhang, Z. X.; Qin, J.; Meng, Q. F.; Du, Y.; Zhang, F. Nano-/micro-fiber engineering of vinylene-linked polymeric frameworks for flexible free-standing thermoelectric films. *Adv. Fiber Mater.* **2025**, *7*, 219–226.

[286] Hu, Q. X.; Liu, W. D.; Zhang, L.; Sun, W.; Gao, H.; Shi, X. L.; Yang, Y. L.; Liu, Q. F.; Chen, Z. G. SWCNTs/Ag_2Se film with superior bending resistance and enhanced thermoelectric performance via *in situ* compositing. *Chem. Eng. J.* **2023**, *457*, 141024.

[287] Zhang, C. R.; Zong, P. A. Ge, Z. S.; Ge, Y. M.; Zhang, J.; Rao, Y. J.; Liu, Z. G.; Huang, W. MXene-based wearable thermoelectric respiration sensor. *Nano Energy* **2023**, *118*, 109037.

[288] He, J. Q.; Wei, R. L.; Ma, X. L.; Wu, W. Q.; Pan, X. J.; Sun, J. L.; Tang, J. Q.; Xu, Z. S.; Wang, C. F.; Pan, C. F. Contactless user-interactive sensing display for human-human and human-machine interactions. *Adv. Mater.* **2024**, *36*, 2401931.

[289] Komatsu, N.; Ichinose, Y.; Dewey, O. S.; Taylor, L. W.; Trafford, M. A.; Yomogida, Y.; Wehmeyer, G.; Pasquali, M.; Yanagi, K. Kono, J. Macroscopic weavable fibers of carbon nanotubes with giant thermoelectric power factor. *Nat. Commun.* **2021**, *12*, 4931.

[290] Li, J. J.; He, X. Y.; Wang, J. H.; Zhu, S. Y.; Zhang, M. C.; Wu, C. X.; Dong, G. Y.; Liu, R. H.; Wang, L. M.; Chen, L. D. et al. Nanoarchitectonics of high-performance and flexible n-type organic-inorganic composite thermoelectric fibers for wearable electronics. *ACS Nano* **2025**, *19*, 11440–11449.

[291] Sun, M.; Tang, G. W.; Wang, H. F.; Zhang, T.; Zhang, P. Y.; Han, B.; Yang, M.; Zhang, H.; Chen, Y. C.; Chen, J. et al. Enhanced thermoelectric properties of Bi_2Te_3-based micro-nano fibers via thermal drawing and interfacial engineering. *Adv. Mater.* **2022**, *34*, 2202942.

[292] Sarabia-Riquelme, R.; Noble, L. E.; Espejo, P. A.; Ke, Z. F.; Graham, K. R.; Mei, J. G.; Paterson, A. F.; Weisenberger, M. C. Highly conductive n-type polymer fibers from the wet-spinning of n-doped PBDF and their application in thermoelectric textiles. *Adv. Funct. Mater.* **2024**, *34*, 2311379.

[293] Wei, L. H.; Dong, T. H.; Cui, Y. P.; Zhu, S. J.; Si, J. X. Molten drawing inorganic ductile $Ag_2S_{0.7}Te_{0.3}$ fibers with high thermoelectric performance and stability. *J. Mater. Sci. Mater. Electron.* **2024**, *35*, 1965.

[294] Fu, Y. Q.; Kang, S. L.; Gu, H.; Tan, L. L.; Gao, C. W.; Fang, Z. J.; Dai, S. X.; Lin, C. G. Superflexible inorganic $Ag_2Te_{0.6}S_{0.4}$ fiber with high thermoelectric performance. *Adv. Sci.* **2023**, *10*, 2207642.

[295] Yin, F.; Luo, X. G.; Wang, X. J.; Liang, Y. X.; Wu, T.; Li, Y. C.; Zhang, K. Q. Flexible and air-stable n-type oleylamine/carbon nanotube hybrid yarns for high-performance wearable thermoelectric generators. *Chem. Eng. J.* **2024**, *498*, 155233.

[296] Zheng, Y. Y.; Han, X.; Yang, J. W.; Jing, Y. Y.; Chen, X. Y.; Li, Q. Q.; Zhang, T.; Li, G. D.; Zhu, H. T.; Zhao, H. Z. et al. Durable,

stretchable and washable inorganic-based woven thermoelectric textiles for power generation and solid-state cooling. *Energy Environ. Sci.* **2022**, *15*, 2374–2385.
[297] Ding, T. P.; Chan, K. H.; Zhou, Y.; Wang, X. Q.; Cheng, Y.; Li, T. T.; Ho, G. W. Scalable thermoelectric fibers for multifunctional textile-electronics. *Nat. Commun.* **2020**, *11*, 6006.
[298] Jang, D.; Park, K. T.; Lee, S. S.; Kim, H. Highly stretchable three-dimensional thermoelectric fabrics exploiting woven structure deformability and passivation-induced fiber elasticity. *Nano Energy* **2022**, *97*, 107143.
[299] Sun, T. T.; Zhou, B. Y.; Zheng, Q.; Wang, L. J.; Jiang, W. Snyder, G. J. Stretchable fabric generates electric power from woven thermoelectric fibers. *Nat. Commun.* **2020**, *11*, 572.
[300] Wu, B.; Wei, W.; Guo, Y.; Yip, W. H.; Tay, B. K.; Hou, C. Y.; Zhang, Q. H.; Li, Y. G.; Wang, H. Z. Stretchable thermoelectric generators with enhanced output by infrared reflection for wearable application. *Chem. Eng. J.* **2023**, *453*, 139749.
[301] Wang, Z.; Jiang, W. K.; Cao, P. L.; Wang, Y.; Xie, A. Q.; Niu, S. C.; Xu, Y. M.; Li, L. H.; Zhang, K. Q.; Wang, X. Q. Bioinspired programmable and ultrastretchable Janus helical hydrogel fibers for strain-invariant thermoelectric body heat harvesting and sensation. *Nano Lett.* **2025**, *25*, 2509–2518.
[302] Kim, S.; Lim, S.; Jeong, M. H.; Kim, W.; Baik, S.; Suk, J. W. Flexible thermocouple using a thermoelectric graphene fiber with a seamless junction. *J. Mater. Sci. Technol.* **2024**, *172*, 15–22.
[303] Jing, Y. Y.; Luo, J.; Han, X.; Yang, J. W.; Liu, Q. L.; Zheng, Y. Y.; Chen, X. Y.; Huang, F. L.; Chen, J. W.; Zhuang, Q. L. et al. Scalable manufacturing of a durable, tailorable, and recyclable multifunctional woven thermoelectric textile system. *Energy Environ. Sci.* **2023**, *16*, 4334–4344.
[304] Hou, Y.; Yang, Y.; Wang, Z. Y.; Li, Z. Y.; Zhang, X. Z.; Bethers, B.; Xiong, R.; Guo, H. Z.; Yu, H. Y. Whole fabric-assisted thermoelectric devices for wearable electronics. *Adv. Sci.* **2022**, *9*, 2103574.
[305] Arimatsu, H.; Osada, Y.; Takagi, R. Fujima, T. Giant seebeck effect in a PEDOT material coated on a felt fiber. *Materials* **2025**, *18*, 838.
[306] Newby, S.; Ahmed, R.; Mirihanage, W.; Fernando, A. Screen-printable p- and n-type functionalized graphene inks for flexible textile thermoelectric generators. *ACS Omega* **2025**, *10*, 39706–39711.
[307] He, X. Y.; Shi, X. L.; Wu, X. Y.; Li, C. Z.; Liu, W. D.; Zhang, H. H.; Yu, X. L.; Wang, L. M.; Qin, X. H.; Chen, Z. G. Three-dimensional flexible thermoelectric fabrics for smart wearables. *Nat. Commun.* **2025**, *16*, 2523.
[308] Wu, Q.; Hu, J. L. A novel design for a wearable thermoelectric generator based on 3D fabric structure. *Smart Mater. Struct.* **2017**, *26*, 045037.
[309] Yang, J.; Pu, Y.; Yu, H.; Ye, D. D.; Liu, X.; Xin, J. H. A cross-plane design for wearable thermoelectric generators with high stretchability and output performance. *Small* **2023**, *19*, 2304529.
[310] Yang, X. N.; Zhang, K. Direct wet-spun single-walled carbon nanotubes-based p-n segmented filaments toward wearable thermoelectric textiles. *ACS Appl. Mater. Interfaces* **2022**, *14*, 44704–44712.
[311] Guo, J. Q.; Zhang, D.; Liu, L. L.; Li, Q.; Fang, Y. J.; Bai, P. J.; Bo, Y. W.; Zhou, Y. T.; Wang, G. F.; Ma, R. J. Highly ductile n-type thermoelectric MOF-based foams. *ACS Nano* **2025**, *19*, 29448–29461.
[312] Zhang, S.; Liu, Z. K.; Wu, Z. H.; Yao, Z. T.; Zhang, W. B.; Zhang, Y. W.; Guan, Z. H.; Lin, H. X.; Cheng, H. G.; Mu, E. Z. et al. Boosting self-powered wearable thermoelectric generator with solar absorber and radiative cooler. *Nano Energy* **2024**, *132*, 110381.
[313] Tan, M. H.; Liu, Y. D.; Wang, Y. Y.; Li, Y. W.; Wu, C.; Jiang, Z. H.; Peng, L. H. Wireless thermoelectric hydrogel recreates biomimetic electric field and angiogenic signal accelerating diabetic ulcer repair. *Adv. Funct. Mater.* **2025**, *35*, 2425610.
[314] Jia, S. Y.; Ma, H. S.; Gao, S. J. Y.; Yang, L.; Sun, Q. Thermoelectric materials and devices for advanced biomedical applications. *Small* **2024**, *20*, 2405019.
[315] Qin, Y. D.; Jia, S. Y.; Shi, X. L.; Gao, S. J. Y.; Zhao, J. Q.; Ma, H. S.; Wei, Y. X.; Huang, Q. L.; Yang, L.; Chen, Z. G. et al. Self-powered thermoelectric hydrogels accelerate wound healing. *ACS Nano* **2025**, *19*, 15924–15940.
[316] Wang, H.; Li, K. C.; Hao, X.; Pan, J. H.; Zhuang, T. T.; Dai, X.; Wang, J.; Chen, B.; Chong, D. T. Capillary compression induced outstanding n-type thermoelectric power factor in CNT films towards intelligent temperature controller. *Nat. Commun.* **2024**, *15*, 5617.
[317] Xu, S. D.; Li, M.; Dai, Y. C.; Hong, M.; Sun, Q.; Lyu, W. Y.; Liu, T.; Wang, Y.; Zou, J.; Chen, Z. G. et al. Realizing a 10 °C cooling effect in a flexible thermoelectric cooler using a vortex generator. *Adv. Mater.* **2022**, *34*, 2204508.
[318] Jung, Y.; Choi, J.; Yoon, Y.; Park, H.; Lee, J.; Ko, S. H. Soft multi-modal thermoelectric skin for dual functionality of underwater energy harvesting and thermoregulation. *Nano Energy* **2022**, *95*, 107002.
[319] Park, M. Recent advances in wearable thermal devices for virtual and augmented reality. *Micromachines* **2025**, *16*, 383.
[320] Wang, L.; Shu, L. C.; Lv, Y. L.; Hu, Q.; Ma, L.; Jiang, X. L. Ultra-efficient and thermally-controlled atmospheric structure deicing strategy based on the peltier effect. *Appl. Therm. Eng.* **2024**, *248*, 123162.
[321] Wang, X. D.; Dong, L.; Zhang, H. L.; Yu, R. M.; Pan, C. F.; Wang, Z. L. Recent progress in electronic skin. *Adv. Sci.* **2015**, *2*, 1500169.
[322] Zhao, Y.; Gao, W. C.; Dai, K.; Wang, S.; Yuan, Z. Q.; Li, J. N.; Zhai, W.; Zheng, G. Q.; Pan, C. F.; Liu, C. T. et al. Bioinspired multifunctional photonic-electronic smart skin for ultrasensitive health monitoring, for visual and self-powered sensing. *Adv. Mater.* **2021**, *33*, 2102332.
[323] Wu, G. C.; Li, X.; Bao, R. R.; Pan, C. F. Innovations in tactile sensing: Microstructural designs for superior flexible sensor performance. *Adv. Funct. Mater.* **2024**, *34*, 2405722.
[324] Liu, Y.; Tao, J.; Mo, Y. P.; Bao, R. R.; Pan, C. F. Ultrasensitive touch sensor for simultaneous tactile and slip sensing. *Adv. Mater.* **2024**, *36*, 2313857.
[325] Su, Y. J.; Liu, Y. L.; Li, W. X.; Xiao, X.; Chen, C. X.; Lu, H. J.; Yuan, Z.; Tai, H. L.; Jiang, Y. D.; Zou, J. et al. Sensing-transducing coupled piezoelectric textiles for self-powered humidity detection and wearable biomonitoring. *Mater. Horiz.* **2023**, *10*, 842–851.
[326] He, H. L.; Xu, J.; Mia, M. H.; Yu, Z. H.; Wan, Y. H.; Jiang, Q.; Qu, X. R.; Liu, J. R.; Hou, L.; Song, Y. Y. et al. Integrated core-shell structured dual-mode thermoresponsive optical-electrical sensing fiber for accurate temperature recognition and early fire warning. *Chem. Eng. J.* **2025**, *521*, 167127.
[327] Chen, C. Z.; Liu, Z. J.; Guo, L. C.; Huo, B. C.; Sun, Q.; Liang, L. R.; Du, C. Y.; Chen, G. M. High spatiotemporal resolution biomimetic thermoreceptors realizing by jointless p-n integration thermoelectric composites. *Adv. Funct. Mater.* **2024**, *34*, 2411490.
[328] Liao, J. C.; Shao, H.; Zhang, Y. X.; Yan, Y.; Zeng, J.; Lan, C. Y.; Gao, B. X.; Chen, D.; Quan, Q.; Xie, P. S. et al. Infrared in-sensor computing based on flexible photothermoelectric tellurium nanomesh arrays. *Adv. Mater.* **2025**, *37*, 2419653.
[329] Zeng, H.; Li, W. H.; Wang, J. T.; Yu, H. L.; Xiong, T.; He, J.; Xiang, Z.; Song, Y. J.; Li, S. Q.; Zhou, D. Y. et al. Simultaneous strain, strain rate and temperature sensing based on a single active layer of Te nanowires. *Nat. Commun.* **2025**, *16*, 10771.
[330] Yu, Z. C.; Huang, L. L.; Zhou, M.; Xu, J.; Ma, J. C.; Wan, Y. H.; Jiang, Q.; Qu, X. R.; He, H. L. Dual-mode core-shell structured early fire warning sensing fiber with selective CO and temperature detection. *Chem. Eng. J.* **2025**, *512*, 162586.
[331] Ding, Z. F.; Li, G.; Wang, Y. J.; Du, C. Y.; Ye, Z. Q.; Liang, L. R.; Tang, L. C.; Chen, G. M. Ultrafast response and threshold adjustable intelligent thermoelectric systems for next-generation

self-powered remote IoT fire warning. *Nanomicro Lett.* **2024**, *16*, 242.
[332] He, H. L.; Qin, Y.; Zhu, Z. Y.; Jiang, Q.; Ouyang, S. N.; Wan, Y. H.; Qu, X. R.; Xu, J.; Yu, Z. C. Temperature-arousing self-powered fire warning e-textile based on p-n segment coaxial aerogel fibers for active fire protection in firefighting clothing. *Nanomicro Lett.* **2023**, *15*, 226.
[333] Zhou, X. X.; Wu, B.; Cai, Z. F.; Li, K. R.; Hou, C. Y.; Zhang, Q. H.; Li, Y. G.; Wang, H. Z. Multifunctional carbon nanotube based thermoelectric yarn enabling fire warning and waste heat harvesting. *Adv. Funct. Mater.*, in press, DOI: 10.1002/adfm.202522298.
[334] Ouyang, B.; Chang, C.; Zhao, L. D.; Wang, Z. L.; Yang, Y. Thermo-photoelectric coupled effect induced electricity in N-type SnSe:Br single crystals for enhanced self-powered photodetectors. *Nano Energy* **2019**, *66*, 104111.
[335] Dai, M. J.; Zhang, X. R.; Wang, Q. J. 2D materials for photothermoelectric detectors: Mechanisms, materials, and devices. *Adv. Funct. Mater*. **2024**, *34*, 2312872.
[336] Li, Y.; Wang, X. Y.; Chen, K. K.; Feng, Y. H.; Liu, P. P.; Jiang, Y.; Shen, Z. H.; Chen, X. Hierarchical MoS_2/CuS photonic nanostructure accelerating photothermoelectric conversion of bacterial cellulose based phase change materials. *J. Colloid Interface Sci.* **2026**, *702*, 138863.
[337] Wang, Z. X.; Wei, Y. C.; Chen, C.; Yang, X. T.; Wei, L. J.; Zhang, Y. S.; Xu, Y. F.; Xie, J. L.; Peng, S. L.; Zhou, H. X. et al. Hybrid-dimensional polycrystalline van der Waals heterostructure for high responsivity and broadband detection. *Laser Photonics Rev.* **2025**, *22*, e00814.
[338] Li, T. T.; Fan, X. X.; Zhang, X. Y.; Zhang, X. F.; Lou, C. W.; Lin, J. H. Photothermoelectric synergistic hydrovoltaic effect: A flexible photothermoelectric yarn panel for multiple renewable-energy harvesting. *ACS Appl. Mater. Interfaces* **2023**, *15*, 57219–57229.
[339] Chen, C.; Yu, H. L.; Zhao, Y. M.; Hou, P. X.; Guo, S. Y.; Li, S. Q.; Wang, H. Z.; Tai, K. P.; Liu, C. Ultrahigh-response flexible photothermoelectric photodetectors based on a graded Bi_2Te_3-carbon nanotube hybrid. *Chem. Eng. J.* **2024**, *497*, 154263.
[340] Xie, Z. M.; Wang, J. Q.; Lu, G. X.; Yeow, J. T. W. Room-ambient operation of integrated and visualized photothermoelectric system with patterned Mo_2C/PEDOT: PSS flexible devices. *Mater. Des.* **2023**, *235*, 112383.
[341] Lu, X. W.; Sun, L.; Jiang, P.; Bao, X. H. Progress of photodetectors based on the photothermoelectric effect. *Adv. Mater.* **2019**, *31*, 1902044.
[342] Matsuzaki, Y.; Tadenuma, R.; Aoshima, Y.; Yamamoto, M.; Takai, L.; Kon, Y.; Sakai, D.; Takahashi, N.; Koshimizu, R.; Zhang, Q. et al. All-solution-processable hybrid photothermoelectric sensors with carbon nanotube absorbers and bismuth composite electrodes for nondestructive testing. *Small Sci.* **2025**, *5*, 2400448.
[343] Fang, H. J.; Xie, X. X.; Jing, K.; Liu, S. J.; Chen, A. N.; Wu, D. X.; Zhang, L. Y.; Tian, H. A flexible dual-mode photodetector for human-machine collaborative IR imaging. *Nano-Micro Lett.* **2025**, *17*, 229.
[344] Wu, W. Q.; Lu, H.; Han, X.; Wang, C. F.; Xu, Z. S.; Han, S. T.; Pan, C. F. Recent progress on wavelength-selective perovskite photodetectors for image sensing. *Small Methods* **2023**, *7*, 2201499.
[345] Guo, X. H.; Lu, X. W.; Jiang, P.; Bao, X. H. Touchless thermosensation enabled by flexible infrared photothermoelectric detector for temperature prewarning function of electronic skin. *Adv. Mater.* **2024**, *36*, 2313911.

Linlong Xing is currently studying for his Ph.D. degree at the College of Physics in Beihang University. He received his Master's degree from Zhengzhou University in 2024 and got Bachelor's degree from Hainan University in 2020. His current research interests are flexible thermoelectric materials and devices.

Yongxin Qin is currently an Associate Professor (full-time) at the International Research Institute for Multidisciplinary Science, Beihang University. He received his Ph.D. degree from Beihang University in 2021 under the supervision of Professor Li-dong Zhao. From 2021 to 2024, he conducted postdoctoral research at the School of Integrated Circuit Science and Engineering, Beihang University. His research interests primarily focus on thermoelectric cooling materials and devices, as well as flexible thermoelectric materials.

Caofeng Pan was conferred his Bachelor of Science degree in 2005 and his Ph.D. degree in 2010, both in Materials Science and Engineering, from Tsinghua University, China. Subsequently, he undertook a postdoctoral fellowship at the Georgia Institute of Technology from 2010 to 2013. In 2013, he assumed the role of a full professor at the Beijing Institute of Nanoenergy and Nanosystems, Chinese Academy of Sciences. Since 2023, he has been serving as a distinguished professor and leads a research group at the Institute of Atomic Manufacturing, Beihang University. His research endeavors predominantly focus on the exploration and application of low-dimensional materials in the development of smart wearable electronics and optoelectronic devices for tactile sensing. For further information, please visit http://www.piezotronics.cn.